Journal of
Materials Chemistry A

ROYAL SOCIETY
OF CHEMISTRY

REVIEW

View Article Online
View Journal | View Issue

Check for updates

Cite this: *J. Mater. Chem. A*, 2025, **13**, 20104

Field-enhanced chemical vapor deposition: new perspectives for thin film growth

Bhupendra Singh,[a] Thomas Fischer[a] and Sanjay Mathur*[ab]

Received 10th February 2025
Accepted 15th May 2025

DOI: 10.1039/d5ta01081k

rsc.li/materials-a

Chemical vapor deposition (CVD) is a versatile technique for producing thin films and coatings of functional materials with diverse mechanical, electrochemical, electrical, tribological, and optical properties. The CVD process is governed by various experimental parameters including precursor chemistry, feed rate, growth temperature, pressure, and carrier or reactive gases. The growth kinetics depends on precursor decomposition that can be influenced by plasma-chemical or photo-dissociation processes to supplement thermal energy. More recently, the application of electric or magnetic fields during the CVD process has impacted the film growth beyond the conventional parametric space. This review highlights the influence of external field effects (plasma, photo-radiation, electric field, and magnetic field) on key steps of thin film processing, such as nucleation, grain growth, texture, density, phase formation, anisotropy, and kinetic stabilization. The emphasis is on recent technical, material, and phenomenological innovations in the CVD technique, with applied fields as extrinsic processing parameters offering new insights into future directions in the research and development of high-fidelity functional films and coatings.

1 Introduction

Chemical vapor deposition (CVD) and its variants represent a platform technology to deposit a diverse range of materials as thin films and coatings that find large-scale applications from the food industry (*e.g.*, antibacterial coatings) to precision-engineered semiconductor devices (*e.g.*, light emitting diodes).[1–6] By definition, CVD involves the deposition of a solid material by vapor phase decomposition of chemical species (precursors) on a substrate maintained at a specific temperature. When compared with physical vapor deposition techniques, such as evaporative deposition, sputtering, and pulsed laser deposition involving the generation of a plume of atomic or molecular species from a source material followed by their deposition (condensation) on a substrate, the CVD process relies upon chemical reactions of gaseous or aerosol precursors,

---

[a] *Institute of Inorganic and Materials Chemistry, University of Cologne, Greinstraße 6, 50939 Cologne, Germany. E-mail: sanjay.mathur@uni-koeln.de*

[b] *Department of Metals and Materials Engineering, Indian Institute of Technology Madras, 600036 Chennai, India*

Bhupendra Singh

Bhupendra Singh is a postdoctoral researcher at the Institute of Inorganic and Materials Chemistry, University of Cologne, Germany. His research interests focus on the synthesis and characterization of materials for electrolysers, SOFCs, and PEMFCs. His current interests include fabrication of thin film electrocatalysts by plasma-enhanced chemical vapor deposition for small molecule activation for energy conversion processes.

Thomas Fischer

Thomas Fischer is a senior scientist at the Institute of Inorganic and Materials Chemistry at the University of Cologne, Germany. He has worked during his doctoral research on metal oxide-based gas sensors and was a co-developer of micro-CVD equipment that enables site-selective growth of metal oxide nanostructures on sensor substrates. His current interests include in situ characterization of chemical vapor deposition processes and the influence of external magnetic fields on the molecular to materials transformation.

occurring in the gas phase and/or on the substrate surface (Fig. 1(a)).[2,7]

The fundamental parameters controlling the CVD process are the temperature of the substrate, pressure in the CVD reactor, precursor feed rate (flux), and the chemical nature of used precursors, as well as carrier gas that can be reactive or non-reactive. The film growth rates are governed by chemical kinetics and energy input, which influence the characteristics of the material, such as adhesion, morphology, microstructure, and crystallinity.[8–13]

The CVD technique encompasses numerous phenomenologically related processes (Fig. 1(a))[2,14] that differ in energy input provided to activate the chemical precursors thermally, optically, or photochemically, resulting in different categories of CVD processes (Fig. 1(b)). In conventional CVD reactors, thin film deposition proceeds by thermal energy provided by resistive heating of the entire reaction zone (hot-wall CVD) or through a susceptor that selectively heats the substrate (cold-wall CVD). Alternatively, utilization of photons or plasma to decompose precursor species has led to the development of photo-assisted CVD (PACVD) and plasma-enhanced CVD (PECVD). The modification of CVD reactors and processes is largely driven by the necessity of achieving conformal coverage and chemically homogeneous deposition, which relies on the vapor pressure and chemical reactivity of the used precursor gases and chemicals. In addition, the necessity of applying functional coatings on temperature-sensitive substrates (*e.g.*, aluminum, glass, polymers) has triggered the use of non-thermal plasmas (so-called cold plasma) in the CVD processes. The benefits of plasma-enhanced processes are twofold: they can activate the substrate surface before deposition, remove any adsorbate layer that is inevitably present, and facilitate the growth kinetics. The attempts to diversify the range of precursors and to have greater control over the precursor chemistry, overcoming the barriers of non-volatility of precursors, have led to the development of aerosol-assisted CVD (AACVD) and metalorganic CVD (MOCVD). Similarly, the requirements for substrate cleaning in the semiconductor industry and the non-thermal initiation step in the

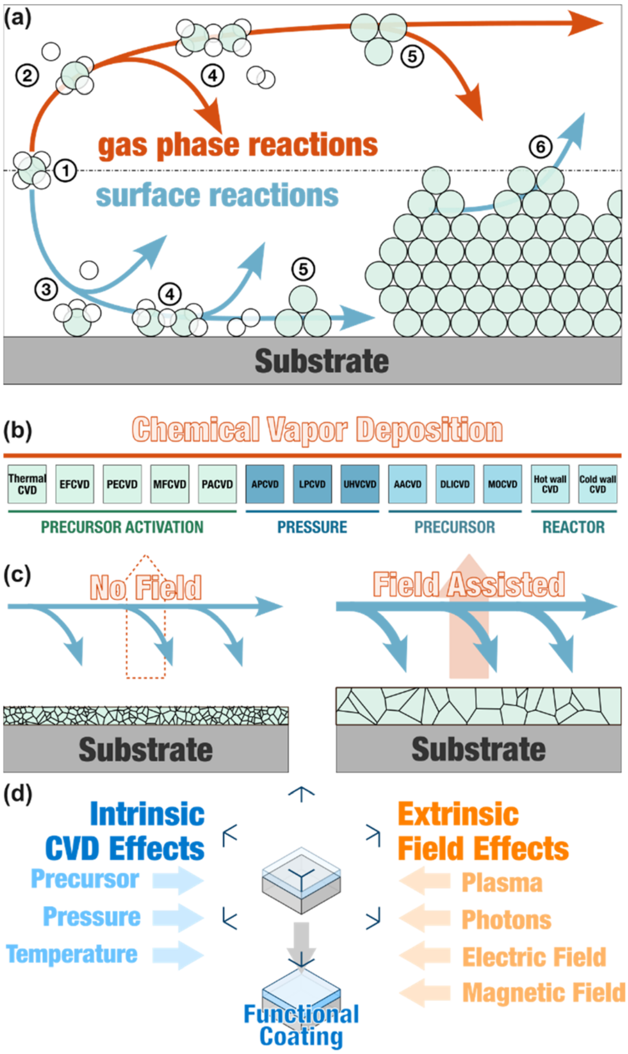

Fig. 1 (a) Schematic of the general elementary steps of a typical CVD process consisting of precursor flow (1), decomposition (2), adsorption (3), intermolecular reactions (4), cluster formation (5), and diffusion (6). (b) Classification of various CVD processes, categorized according to precursor activation, pressure, precursor delivery and reactor type; PECVD, RPECVD – remote plasma enhanced CVD, APCVD – atmospheric pressure CVD, LPCVD – low pressure CVD, UHVCVD – ultrahigh vacuum CVD, AACVD – aerosol-assisted CVD, DLICVD – direct liquid injection CVD, MOCVD – metalorganic chemical vapor deposition. (c) and (d) Schematic representation of intrinsic CVD process parameters and extrinsic field effects enabling auxiliary control over the CVD process.

Sanjay Mathur

Sanjay Mathur is director and chair of the Institute of Inorganic and Materials Chemistry at the University of Cologne, Germany, and a distinguished professor at the Indian Institute of Technology, Madras. His research interests focus on the application of nanomaterials and advanced ceramics for energy technologies. He holds several patents and has authored/co-authored over 540 original research publications (h index, 80) and has edited several books. He serves as the editor-in-chief for the Journal of Electroceramics, and editor for Nano Energy. He is an Academician of the World Academy of Ceramics. He is a fellow of the American Ceramic Society, ASM International and Materials Research Society and the European Ceramic Society. He was elected a fellow of the European Academy of Science (2020), a foreign fellow of the National Academy of Science, India (2021) and a fellow of the African Academy of Science (2024). He was awarded the Woody White award of the Materials Research Society (2021) and had received the medal of the Chemical Research Society of India (2022). He is also a recipient of the Materials Frontiers award (2022) of the International Union of Materials Research Society (IUMRS, 2022).

polymerization of thermally sensitive materials have led to the development of low energy and/or pulsed plasma CVD.[15–17]

In thermal CVD, the role of temperature has been to fulfill the energy requirements for precursor decomposition, although it has further influenced the nucleation and growth kinetics.[18–20] Temperature and other precursor-specific intrinsic parameters (composition, flow rate, precursor chemistry, *etc.*) are thermodynamics-dependent and often need macro-level control to execute micro-level variations in the properties of the resulting deposition. On the other hand, the characteristics of precursor-independent extrinsic parameters (photons, plasma, electric field, magnetic field) are controlled, independent of thermodynamics (Fig. 1(c) and (d)). Therefore, while using photon or plasma as an agent fulfilling the energy requirements, manipulations in their characteristics have provided additional means to manipulate and control the CVD process at the microscopic level. For example, besides providing energy for precursor decomposition, plasma also provides energetic species – electrons, photons, ions, excited atoms, and molecules – to the substrate/growth surface, causing surface reconstruction, stoichiometric change, and alteration in reaction rate and growth kinetics. Moreover, the interaction of the precursor with plasma species initiates an alternative decomposition pathway, enabling deposition without temperature assistance or at a significantly lowered temperature.[15] Similarly, the use of laser radiation for precursor dissociation localizes the thermal energy and generates free carriers that further influence the thermodynamics and kinetics of the CVD steps.[21] Additionally, photolysis and photosensitization reduce the energy of activation (E_a) of gaseous or surface-adsorbed species, accelerating the reaction kinetics.[22]

The energy associated with an electric field (EF) or magnetic field (MF) generated in a normal laboratory environment may not be sufficient to overcome the E_a for precursor decomposition in CVD. However, when applied in a CVD environment, the field associated with them interacts with various components (precursor, decomposition products, substrate, plasma, *etc.*), influencing the growth rate or modifying the film properties.[23] For example, an external EF-assisted bias-enhanced nucleation has been key in the "seed-free" deposition of diamond on smooth surfaces.[24,25] Similarly, the application of MF in the course of precursor flow or around the substrate, inside the reactor, has provided directional control over the movement of polar/charged species, altering the deposition and growth parameters.[26] Moreover, coupling of an external MF with other CVD modulators, such as EF,[27,28] plasma,[29,30] or both,[26,31] has generated a synergistic effect, imparting a unique microstructure and morphology to the deposited films.

The development of novel functional materials for targeted applications drives the need for new strategies to modulate the CVD process beyond conventional control parameters. In this context, the use of plasma and photo-irradiation, as well as the integration of external electric (EF) and magnetic fields (MF) into CVD setups, has shown significant potential to control intrinsic materials characteristics. These external fields can influence reaction kinetics and overcome the constraints of conventional CVD methods, enabling low-temperature deposition, alternative nucleation and growth mechanisms, selected area deposition, directional grain growth, molecular-scale engineering, and substrate versatility. This review is motivated by recent advances in CVD methodology that leverage such field effects – both contact-based (plasma and photo-irradiation) and non-contact (electric and magnetic fields)—to exert additional control at the microscale. These approaches help transcend the restrictions imposed by macroscopic parameters on growth rate, composition, phase, morphology, and microstructure.

This account highlights the key achievements made in field-assisted CVD, emphasizing how these techniques enable the fabrication of thin films with enhanced material properties. The review is organized into focused subsections; each begins with an introduction to the field-matter interaction during CVD, followed by a discussion of field as an external parameter to control the CVD process, either independently or in combination with conventional parameters. Each section is concluded by outlining the influence of fields on precursor decomposition, nucleation, film growth, and resulting characteristics.

2 Plasma-assisted/enhanced chemical vapor deposition

2.1 Plasma-matter interaction during chemical vapor deposition

The PECVD process primarily utilizes the high energy electrons present in the non-equilibrium plasma of partially ionized gases (reactive and/or carrier), having electron temperature $T_e \leq$ 10 eV (1 eV = 11 600 K) and gas temperatures ranging from room temperature to 10^4 K, to excite atomic and molecular precursor species to higher electronic and vibrational states.[32] This initiates or/and promotes the dissociation of chemical bonds, consequently facilitating thin film deposition at significantly lower temperatures compared to conventional thermal CVD processes. Plasma electrons, owing to their low mass and high mobility, lead in receiving energy from the ionization source (electric field, heat, light, magnetic field, *etc.*) and transmit it to other species *via* inelastic collisions, leading to numerous gas-phase plasma-chemical processes, such as ionization/recombination, excitation/relaxation, dissociation/association, and charge-transfer reactions.[33] The electron energy distribution function (EEDF; $f(\varepsilon)$), denotes the probability density for an electron to possess energy ε and is described by eqn (1)

$$f(\varepsilon) = 2\sqrt{\varepsilon/\pi(kT_e)^3}\exp(-\varepsilon/kT_e) \tag{1}$$

where k is Boltzmann's constant and T_e is the electron temperature, which becomes key in determining the rate of these processes. The EEDF indicates how electrons acquire energy from an electric field and lose it in collisions with the background gas. In low-density plasma, electrons have a Druyvesteyn energy distribution, whereas in high-density plasma they have a Maxwellian energy distribution.[34] The $f(\varepsilon)$ depends on the gas composition and electric field frequency used to generate plasma. Nevertheless, the ions, radicals, excited atoms/molecules, and photons present in the complex mixture resulting from plasma-material interactions also play an important role in the efficiency of a PECVD process.[35,36]

During the PECVD process, the quasi-neutrality of plasma bulk breaks due to the buildup of charge near the substrate surface, and an electrically non-neutral region known as the plasma sheath is formed. The sheath thickness, which is of the orders of Debye length, depends on electron energy and electron density. As the potential attained by the substrate (floating potential) is less than plasma potential (V_P), positive ions diffuse through the plasma sheath, acquiring some additional energy en route to the substrate surface, which can be regulated by substrate biasing (V_B) leading to the maximum kinetic energy given by eqn (2)

$$E_{i,\max} = e|V_P - V_B| + (\Delta E/2) \tag{2}$$

where the term ($\Delta E/2$) corresponds to the periodic modulation (excitation frequency) of sheath voltage. The optimization of plasma-assisted modulation of CVD encompasses the identification of discharge characteristics suitable for the generation of high densities of free radicals and ions diffusing toward the surface and leading to deposition. To this end, external parameters (pressure, gas composition and flow, discharge excitation frequency, and power) are administered to modulate the resulting plasma characteristics (plasma density, electron temperature, EEDF, electrical potentials, fluxes of species). In practice, ion energy (E_i) and ion flux (Φ_i), key parameters affecting the film characteristics, are governed by the prevailing excitation frequency (radio frequency, RF or microwave, MW), pulsed direct current (DC), or RF-induced negative substrate bias.[35,37] Accordingly, based upon the power frequencies for plasma generation, the PECVD is often sub-classified as microwave PECVD (0.5–10 GHz), radio frequency PECVD (1–500 MHz), and direct current PECVD.[38] Additionally, depending upon the mode of plasma confinement using electrical, magnetic, or both, affecting the plasma density, the PECVD is further sub-classified as capacitively/inductively coupled PECVD,[39,40] helicon wave PECVD,[41,42] electron cyclotron resonance PECVD,[43,44] and so on.[45]

Santhosh *et al.*[46] presented an interesting overview of different modes of generation and confinement in plasma systems used in PECVD (Fig. 2). The PECVD process relies on a complex interplay of plasma characteristics, precursor chemistry, and reactor design.[48,49] Notwithstanding, high precursor decomposition efficiency, even at room temperature, is ensured by energy transfers in the form of kinetic and potential energies through plasma electrons and charged particles to the precursors, leading to the formation of free radicals and charged ions that are critical in influencing the deposition and growth.[50,51] Additionally, the plasma-surface interaction under appropriate plasma conditions, apart from initiating/promoting precursor decomposition, also promotes adsorption, desorption, nucleation, adatom migration, implantation, sputtering and displacement of atoms, thus tuning the composition, phase, microstructure, and morphology of the deposited material.[37,52,53]

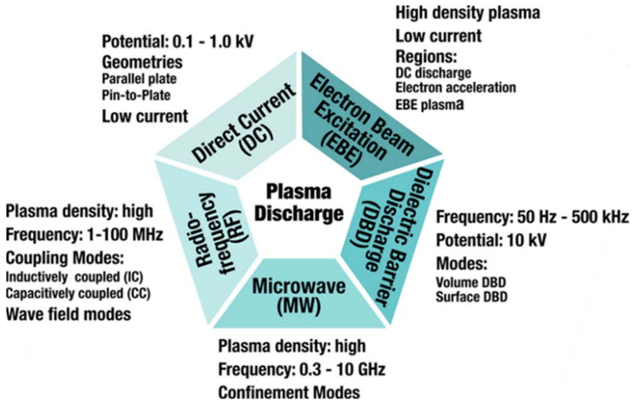

Fig. 2 A brief overview of different plasma systems used in PECVD.[46,47]

2.2 Overview of plasma-enhanced chemical vapor deposition

The plasma-assisted modulations in CVD induce gas-phase chemistry mediated by energetic plasma species, enabling the decomposition of precursors, even of low reactivity, leading to deposition on temperature-sensitive and morphologically intricate substrates.[54,55] A recent review by Snyders *et al.*[48] provides an impressive historical background of the stages of development and conceptual foundations of PECVD, tracing the origin of PECVD to 1911. Several other reviews discussing the basic chemical and physical phenomena associated with the PECVD process have been reported.[17,46–48,50,56–60]

The PECVD process has been successfully used for depositing metals and ceramics,[50,61–66] carbon-based materials,[58,59,67–71] and organic polymers.[17,48,72] In recent years, plasma-assisted modulations have focused on enhancing deposition and growth rates,[73] achieving directional growth and crystallographic orientation of nanostructures,[59,74–76] surface modification,[77–80] doping and vacancy generation,[81–85] and manipulating phase composition and crystallinity.[86–89] Table 1 presents selected recent reports on PECVD, displaying its utility in thin film fabrication for a range of materials.

In PECVD, the excitation frequency of the plasma source provides a key tool to modulate the deposition process.[100,117–122] Generally, an RF plasma source uses industrial 13.56 MHz frequency for plasma excitation, and for increasing the plasma density to accelerate the precursor decomposition and subsequent film growth rate, the plasma power is increased. However, an increase in power also causes increased ion bombardment, which often proves detrimental to the film quality. To overcome this, very high frequency (VHF; 30–300 MHz)[123–125] or dual frequency[126–129] plasma configurations are employed. With VHF plasma, increased frequency imparts higher energy to electrons *via* so-called stochastic heating but reduces the sheath thickness and lowers the electrical field intensity, thereby reducing the ion-bombardment energy.[120] A dual frequency configuration involves two different frequencies on the same electrode or on separate electrodes, where high frequency imparts a stable discharge generating the reactive species and the low frequency controls the ion bombardment.[119] The dual frequency

Table 1 Some recent reports on plasma-enhanced CVD of functional materials[a]

Material/substrate	Plasma-type	Key features	Application	Ref.
Carbon-based materials				
Diamond films on 3D Si spheres	MW, (CH_4, H_2), 10 kPa	Uniform EF and plasma distribution by a Faraday cage	Uniform diamond coating on complex 3D geometries	73
Diamond films/Si	MW, 600–900 W, (H_2, Ar, CH_4), 12.6 kPa, 750 °C	Bias-enhanced nucleation led azimuthal texturing; Raman peak ~1332 cm^{-1}	Quantum devices; coatings with aligned *N* vacancy defect centres, ~70% azimuthal orientation	90
DLC/tungsten carbide	Cathode arc discharge (120 A DC), (N_2, Ar, C_2H_2), 0.9 Pa, 450 °C	Role of particle energy on structure and properties	Cutting tool protection film; coefficient of friction = 0.112	91
(*n*-Diamond)-carbon nanowalls hybrid/Si(100)	CCP-RF, 300 W, (CO, CH_4, Ar, H_2), ~33 Pa, 450 °C	Large area (4 inch) simultaneous deposition	—	92
Fluorescent nanodiamond with Si impurity/Si	MW, (H_2, CH_4), 2.5 kPa, 700 °C	A vertically aligned Si source in the plasma path gives highly fluorescent (7–10 times enhanced) diamond film	Photoluminescent films	85
Vertical graphene (VG)/quartz	RF, 500 W, (C_2H_2, H_2), ~1 × 10^5 Pa, 900 °C	Position-induced control over morphology; superhydrophobicity and ultrahigh emissivity (0.999)	Black body and infrared thermometer	93
Graphene/sapphire	ECR, 500 W, (C_2H_2, H_2), ~0.54–5.4 kPa, 600–700 °C	Direct growth of uniform and continuous graphene on insulators at reduced temperature	Graphene film for optoelectronic device; transmittance > 90%, sheet resistance < 1 kΩ)	94
Vertical graphene/SiO_2	RF (remote), 300 W, (CH_4, Ar), 0.1 Pa, 300–1000 °C	Interfacial EF between plasma and substrate-governed vertical growth	—	95
Metalloids				
SiN_x/SiOF/SiN_x flexible moisture barrier film/polymer substrate	MW, 1500 W, (Ar, SiF_4, N_2O), 9 Pa, 45 °C	Films with high WVTR (3.94×10^{-4} g m^{-2} day^{-1}) and visible light transmittance (93.32%)	Roll-to-roll processing of optical devices	96
Amorphous hydrogenated silicon carbonitride/Si	MW (remote), 120 W, (TMDS/HMDS, H_2, N_2), 43–90 Pa, 30–400 °C	Precursors with Si–H bonds are necessary for initiation of remote plasma-CVD with a single source	Tribological coatings	97
Si film on different substrates	CCP-RF, 15 W, (SiF_4, H_2, Ar), 306 Pa, 150 °C	Area-selective Si deposition; surface-dependent nucleation delay due to a fluorinated Si precursor	—	98
Hydrogenated silicene/polycrystalline Ag	—	First report of silicone synthesis by PECVD	—	99
Phosphorus-doped nanocrystalline SiO_x/glass	RF (13.56, 27, 40 MHz), (318, 333, 256 W), (SiH_4, H_2/CO_2/PH_3), 200 °C	Industrial-scale deposition using a very high-frequency PECVD system	Si heterojunction solar cells	100
2D hexagonal-boron nitride (h-BN)/SiO_2/Si	RF, 30 W (BH_3-NH_3, Ar/H_2), ~115 kPa, 300 °C	First report of catalyst-free directly-on-substrate growth	Dielectric interface for WSe_2 field-effect transistor	101
Multilayered h-BN/Si, SiO_2/Si, and quartz	ICP-RF, 40–180 W, (borazine, Ar, N_2, H_2) 10–100 Pa, 300–900 °C	Catalyst-free low-temperature growth of multilayered (>50 nm) h-BN	Optoelectronics; comparable/better optical characteristics than commercial h-BN, $E_g = 5.8$ eV	40
h-BN/Si	MW, 1000 W, (H_2, NH_3, B_2H_6), 2 kPa	Regardless of B_2H_6 flow rate (0.6–3.0 sccm), h-BN with B/N ratio = 1 is formed	High-hardness coatings	102
2D boron carbonitride (BC_xN)/SiO_2/Si or SiO_2	30 W, ($BH_3 \cdot NH_3$, CH_4, Ar, H_2), 80 Pa, 450–620 °C	First report of catalyst-free temperature-dependent BC_xN growth; $E_g = 2.3$ eV	Field effect transistors and sensor; H_2O_2 detection limit = 0.1 μM	103
Boron film on (100) Si	RF, 1000 W, (Ar, B_2H_6), 133–239 Pa	Comparison of PECVD films with other related deposition techniques	Mask layer/structural material in micro-machining	104

Table 1 (*Contd.*)

Material/substrate	Plasma-type	Key features	Application	Ref.
Metals, oxides, chalcogenides, nitrides				
Fe, Co, and Ni metallic films on different substrates	DC hallow cathode, 50–150 W, 50 Pa, 70–100 °C	Plasma electrons as reducing agents; electrical conductivity of the substrate plays a major role	Catalysts and electronic devices	105
Cu_2O on different substrates	CCP-RF, 10 W, (Ar), 26 Pa, 200 °C	Large area (2.88×3.13 m^2) uniform deposition	Thin-film semiconductors; $\rho = 10^5$ Ω cm; $E_g = 2.53$–2.59 eV, $\mu_H = 1.48$ cm^2 (V s)$^{-1}$	106
MoS_2/sapphire or SiO_2/Si	RF direct/remote plasma, 300 W, (MoO_3, H_2S, Ar), 400 °C	Photoluminescence (direct plasma deposited only at 2.0 eV; remote plasma dep. at 1.8 and 2.0 eV)	Hydrogen evolution reaction (HER)	107
N-alloyed Ga_2O_3 films (Ga_2O_3, GaON, and GaN)/*c*-Al_2O_3	RF, 200 W, (Ga, Ar, N_2, O_2), 850 °C	Bandgap tuning and O vacancy density (V_o) reduction by adjusting $N_2 : O_2$ gas ratio	Photodetectors; $E_g = 4.64$–3.25 eV, $V_o = 32.89$–19.87%	108
MoS_2	ICP-RF, 300 W, (S_8, Ar), 29–53 Pa, 500 °C	Single-step deposition using elemental S and $MoCl_5$ as precursors	—	109
Mo_2C/MoS_2 or $Mo_2C/MoSe_2$ on Cu foil	RF, 150 W, (S/Se, H_2, N_2), 750–350 °C	Phase-engineering of Mo_2C by plasma-assisted selenization and sulfurization	HER; (Tafel slope/mV dec^{-1}: $Mo_2C/MoS_2 = 83$, $Mo_2C/MoSe_2 = 66$); (overpotential/mV: $Mo_2C/MoS_2 = 2263$, $Mo_2C/MoSe_2 = 257$)	110
Amorphous carbon-tin film/glass	Glow discharge (40 kHz), 500 W, 4.2 Pa	Coupling capacitance of the reactor controls the semiconductor/insulator characteristics	HER or CO_2 reduction; transport gap = 5.2 eV, $E_g = 3.1$ eV, electron affinity = 2.1 eV, ionization potential = 7.3 eV	111
Cr–N coating on Cr layer	MW, 5000 W, (H_2 and N_2), ~22.6 kPa, 750–950 °C	MW plasma-assisted *in situ* reactions on a chromium pre-coated substrate	Tribological coatings; coefficient of friction <0.55 (in 750–950 °C range), wear resistance = 0.085 and resistance to plastic deformation = 0.142 at 800 °C	112
GaS on different substrates	RF (40.68 MHz) discharge, 50 W, 13.3 Pa, 250 °C	Influence of substrate on stoichiometry, structure, and surface morphology investigated	—	113
TiN, TiBN or TiB_2 hard coating/steel	Pulsed DC, (BBr_3, $TiCl_4$, N_2, H_2, Ar), ~933–1200 Pa, 500 °C	Use of BBr_3 as a B precursor; hardness of TiN, TiBN and TiB_2 films was 15.74, 19.44 and 23.47 GPa, respectively	Tribological coatings; for TiB_2 coating, elastic modulus = 298 GPa and coefficient of friction = 0.23	75
GeSn film on Si	RF, 30 W, ($GeCl_4$, $SnCl_4$, H_2), 53 Pa, 180 °C	Low-temperature GeSn film without any buffer layer or post-annealing (growth rate ≈15 nm min^{-1} at 180 °C)	Short-wave infrared Si photonics; high Sn (>9%) and low threading dislocation density (1×10^7 cm^{-2})	114
Others				
Methyl ammonium iodide (MAI)	RF, 60 W, (MAI, H_2O, Ar), ~13 Pa	First report of MAI deposition using PECVD for $MAPbI_3$ films; $E_g = 1.57$ eV, refractive index = 3.07, extinction coefficient = 0.13	perovskite/Si photodiode; rectifying ratio = 1.58×10^4 at 1.0 V, photo-sensitivity = 7.46×10^2	115
Poly(DPAEMA) film	RF, 20–80 W, (diisopropyl aminoethyl methacrylate, N_2), ~13–67 Pa, 10–40 °C	Initiator-free polymerization; large area (>16 cm diameter) deposition rate = 18.6 nm min^{-1} at 40 °C	pH-responsive polymers	116

[a] CCP – capacitively coupled plasma; ICP – inductively coupled plasma; DLC – diamond-like carbon; DPAEMA – 2-diisopropyl aminoethyl methacrylate; E_g – optical band gap; h-BN – hexagonal boron nitride; HMDS – hexamethyldisilazane; *n*-diamond – new-diamond (face centered cubic-carbon); TMDS – 1,1,3,3-tetramethyldisilazane; WVTR – water vapor transmission rate; ρ – resistivity; μ_H = hall mobility.

configuration has proven its utility in improving the deposition quality in terms of film stress, step coverage, and stability.[129]

In catalyst-mediated PECVD processes, plasma-catalyst interactions play a key role during the pretreatment step and deposition. Such plasma-assisted restructuring or activation has proven to be important for controlling the mechanism, growth rate, composition, morphology, and microstructure.[130–135] Restructuring of metal catalysts used for the growth of carbon nanostructures,[130–134] silicon nanowires[135–139] and other metal/metal oxide nanowires[140,141] by plasma pre-treatment or/and during plasma-assisted catalytic vapor–liquid–solid[142,143] and solid–liquid–solid[141,144] growth mechanisms is well documented. For example, Zheng *et al.*[141] demonstrated that during GeSn nanowire growth using Sn nanoparticle catalysts H_2 plasma-assisted annealing inhibited the wetting of Sn during and at the end of nanowire growth, preventing the pinning of Sn NPs around the nanowires. Similarly, during *in situ* fabrication of graphitic nanosheet supported N-doped carbon-coated $LiFePO_4$ (LFP@NC/GNS), plasma assisted the reduction of Fe^{2+} ions to Fe^0, which catalyzed *in situ* formation of graphitic nanosheets on LFP@NC, and simultaneously removed $Fe^{\bullet}_{Li}$ antisites, a commonly observed detrimental defect in LFP for its performance in Li-ion batteries.[134]

Over the years, there has been a growing trend to integrate PECVD with other deposition techniques for the deposition of a diverse range of materials. In PECVD of rare-earth element-doped Si-based materials, metal-organic precursors are used for *in situ* metal doping. However, the use of metal-organics causes significant hydrogen contamination. To overcome this limitation, a hybrid deposition technique was developed by *in situ* coupling PECVD with a magnetron sputtering source having the rare-earth target.[145–150] Kulczyk-Malecka *et al.*[150] proposed a high-power impulse magnetron sputtering-PECVD system where the magnetron-generated plasma also acted as an electron source to drive the precursor decomposition in the PECVD process, thus requiring only a single power supply. Moreover, the application of a variable magnetic field strength magnetron resulted in precise control over dopant content without adjusting the power supply. Lee *et al.*[151] used a similar PECVD-sputtering hybrid system to fabricate Ti-doped diamond-like carbon (DLC) coatings, where metal doping helped overcome the residual stress in the deposits. Moreover, a multi-step PECVD or its integration with other deposition techniques resulted in a specific nanostructured assembly.[152–156] For example, Huang *et al.*[153] reported an anode-assisted reactive magnetron sputtering coupled with a DC PECVD system to fabricate amorphous hydrogenated DLC coatings with CrC interlayers, ameliorating the adhesion properties of DLC coatings by reducing the residual stress. Dias *et al.*[157] reported large-volume deposition ($\sim$19 mg min^{-1}) of metal oxide/sulfide anchored *N*-graphene for supercapacitor applications by spraying a controlled metal-oxide(sulfide) microparticle jet into the plasma afterglow region, leading to plasma-induced size reduction and subsequent binding to the *N*-graphene sheets. Furthermore, Su *et al.*[158] reported an integrated process encompassing plasma-assisted roll-to-roll deposition of vertical graphene (VG, which is graphene-containing carbon nanosheets grown vertically onto the substrate) and simultaneous syngas production from greenhouse gas mixtures. Such hybrid approaches have effectively expanded the application spectrum of PECVD, overcoming the technological barriers of limited precursor availability.

Over the years, manipulation of plasma characteristics and plasma delivery has enhanced the CVD process for tailoring film properties for desired applications. In this regard, PECVD using pulsed plasma flow with dynamic pulse parameters such as pulse frequency, duty ratio, and peak power has displayed remarkable effects on the deposition qualities.[51,159–164] Pulse modulation, in combination with other plasma parameters, has been successful in significantly decreasing deposition temperature while maintaining or even enhancing characteristics like growth rate and composition.[159,165,166] Interestingly, significant film growth also occurred during the "off" plasma duration[167] and the pulsed mode resulted in additional morphological variations.[168,169] For example, during PECVD growth of 2D copper sulphide superstructures, Taplick *et al.*[169] observed that site-dependent charging–discharging dynamics during plasma pulsing played a crucial role in the directed assembly of nanoplatelets in the gas phase. The plasma pulsing promoted side-by-side growth, whereas continuous plasma additionally caused pronounced spike-like growth perpendicular to the basal plane. Similarly, pulsed PECVD displayed great usefulness in PECVD of insulating thin films, where substrates need to be under an alternating signal.[170] In this regard, it is worthwhile to mention the hybrid plasma-immersion ion implantation and deposition systems for DLC coatings from hydrocarbon precursors, where ion-implantation renders improved tribological and mechanical properties.[171–173] Recently, Tran *et al.*[160] used a similar hybrid system to fabricate high surface area activated carbon coatings for biomedical applications, where the growing coatings were subjected to implantation of ion-aggregates formed in the plasma in a high voltage dielectric barrier discharge PECVD.

Moreover, efforts have been made to further modulate pulsed PECVD by coupling it with externally-controlled MF for plasma confinement.[162,163,174] To fabricate pinhole-free amorphous silicon carbo-nitride, SiCN, at a high deposition rate, *e.g.*, Matsutani and coworkers[162] designed an MF coupled pulsed PECVD system, where a permanent magnet kept below the plasma electrode (which also holds the substrate) in a parallel electrode setup led to an increase in plasma current and deposition rate, as compared to that without MF. In a subsequent study, they generated pulsed plasma alternatively on both electrodes, while keeping the permanent magnet below the substrate electrode, to overcome the etching-induced film thinning due to the charging effect.[163] The MF confinement of plasma during the plasma-immersion ion implantation and deposition of DLC coating resulted in improved diamond-like character with defect-free morphology and reduced roughness in as-grown films.[174]

Plasma-assisted processes have been demonstrated for large-scale fabrication of various carbon nanostructures for electronics, optoelectronics, energy and environmental applications.[59,67,175–179] In addition, PECVD processing has enabled a controllable preparation strategy for the growth of desirable carbon nanoarchitectures at significantly lower temperatures[112] and even without the need of catalysts,[180] ensuring high purity by eliminating metal contamination. In the catalyst-free growth of VG,[181] high-energy ion bombardment activated the surface for nucleation by inducing defects and facilitated growth mainly from the surface of the substrate.[176,180] PECVD has enabled substrate-independent growth of graphene, facilitating its growth at 700 °C on Si and 3C–SiC/Si surfaces, important in electronic/optoelectronic heterojunction devices, which could not be achieved by thermal CVD due to the extremely low diffusion of carbon over these surfaces, as indicated by the theoretical studies.[182] For deposition of amorphous carbon/DLC films, the control over plasma-ion energy by adjusting the bias power and bias voltage has conferred control over the H-content and I_D/I_G and sp^2/sp^3 ratios, regulating their amorphous or DLC characteristics and resulting in mechanical, electrical, optical, or tribological properties. For example, high ion density plasma, such as microwave plasma and magnetically enhanced plasma, promoted low H-content whereas low-density RF plasma promoted high H-content growth.[68,69] A high ion density helped in the removal of H atoms from C–H bonds and raised the sp^2/sp^3 ratio in the deposited films.[69]

An important aspect of catalyst-aided or catalyst-free PECVD of various carbon nanomaterials is its ability to aid in vertically aligned growth, as the electric field associated with the plasma

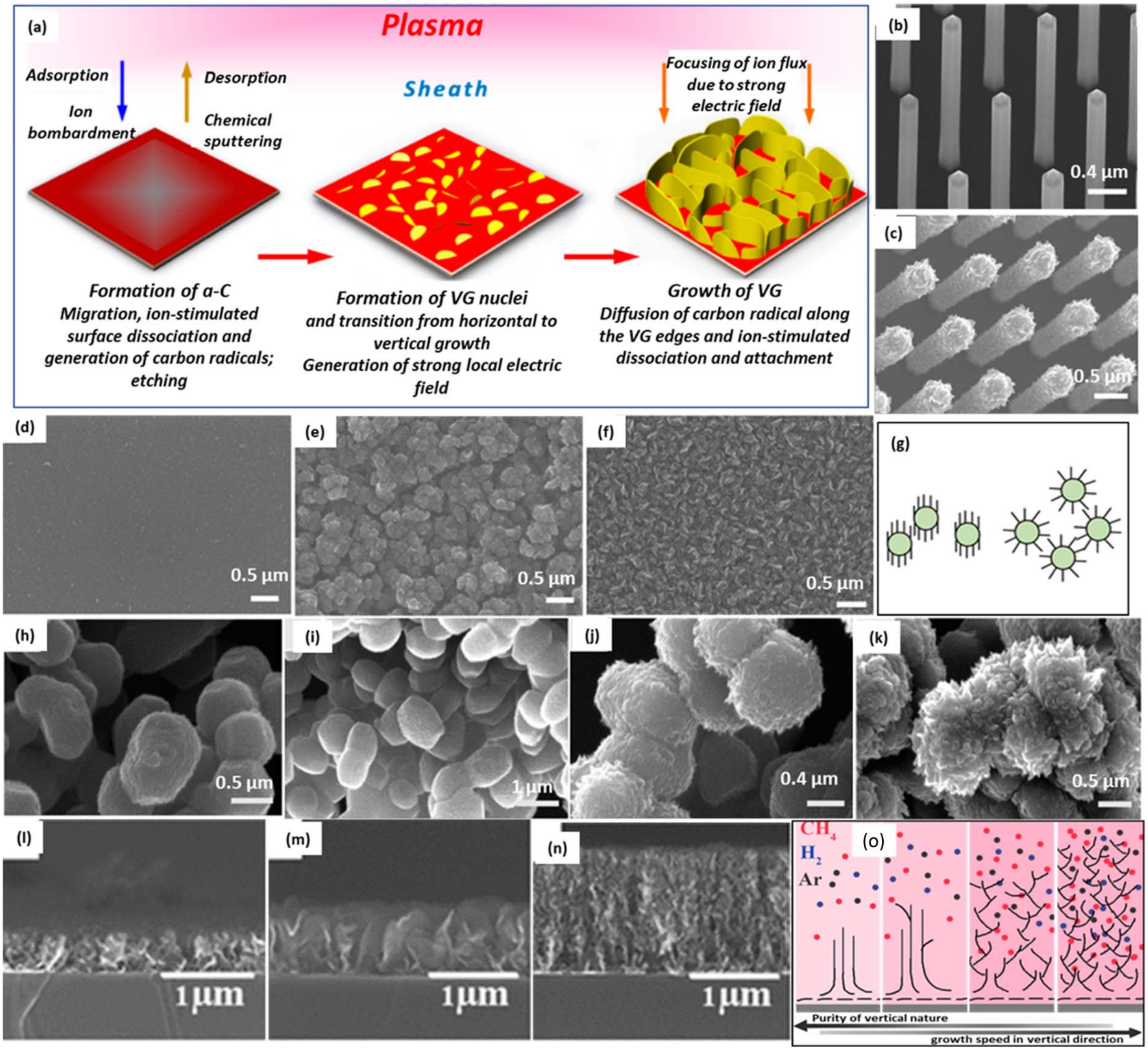

Fig. 3 Schematic diagram of plasma-assisted vertical growth of carbon nanostructures (a), adopted with permission from MDPI;[46] acanning electron microscopy (SEM) images of GaN nanowires (b) before and (c) after the VG growth in remote PECVD; SEM images of growth on the SiO$_2$/Si substrate surface, nearly complete growth inhibition of VG growth when EF is completely screened (d), growth along the mesh holes when EF is partly blocked (e), normal VG growth without screening (f); schematic illustration of possible growth modes of VG on nanoparticles – (left) perpendicular to the substrate and (right) alongside the normal directions of the nanoparticles (g); SEM images confirming the latter growth mode with increasing flow rates of C$_2$H$_2$ and growth times (h)–(k), reused with permission from American Chemical Society (ACS).[186] SEM images of VG deposited at 600 °C with different plasma powers, 100 (l), 200 (m), and 300 (n); and schematic showing the difference in growth behavior of VG under different plasma densities (o), reused with permission from ACS.[95]

sheath helps the nanofibers grow vertically from the substrate.[59,95,183–185] Various studies demonstrate, however, that the mechanistic implications of the role of plasma and other process parameters on the vertical growth mechanism are not well understood.[95,186,187] Theoretical studies suggest that during VG growth, the coulombic repulsion due to the accumulated electrons on the flakes eventually push the growth to change from 2D to 3D mode.[186] Sun *et al.*[186] studied the role of plasma sheath EF in the mechanism for the growth of vertically grown graphene nanostructures. Using GaN nanowires grown onto a silicon substrate (GaN/Si) (Fig. 3(a)), much denser and longer growth of VG flakes was observed at the nanowire tips than on the nanowire bodies (Fig. 3(b)), indicating a local field-enhancement effect due to the higher field strengths and charge accumulation at the wire tips (Fig. 3(c)). Furthermore, when EF is selectively screened by employing metal meshes of different sizes, growth occurred only along the holes (Fig. 3(d)–(f)), due to partial blocking of the electric field formed in the plasma sheath. Moreover, using SiO_2 nanoparticles as substrate, out of two possible modes of growth (Fig. 3(g)), the VG exclusively grew perpendicular to the particles' surface (Fig. 3(h)–(k)).[186] These findings set the foundations for further mechanistic studies on the vertical growth of 2D materials.

Zhang and coworkers[188–191] demonstrated the use of auxiliary vapors (chloroform, fluorobenzene, water, *etc.*) along with the chemical precursor to generate a special collection of plasma and reactive species to enhance the growth rate of VG in an electric field-assisted PECVD. For example, the introduction of fluorobenzene and water in the deposition chamber promoted the decomposition of the carbon source and etching of amorphous carbon, respectively, to enable higher growth rates ($\sim$14.4 μm h^{-1}).[189] Zhang *et al.*[95] observed that milder plasma and temperature conditions are helpful for vertical growth, as the higher growth temperatures, precursor and carrier flow rates, and applied plasma power also promoted branching (Fig. 3(p)), apart from increasing the growth rate (Fig. 3(i)–(n)).

In vacuum or atmospheric PECVD, plasma-assisted effects have demonstrated synergistic regulation of nanostructures and defect engineering in carbon nanostructures.[46,93,192–197] For example, Ma *et al.*[93] demonstrated a continuous variation of morphology, from “porous” to “tree-like” and then to “wall-like” structure, by adjusting the growth positions during PECVD of VG. Similarly, Dias *et al.*[198] reported a PECVD approach capable of varying the density and energy of basic building blocks within the high energy-density plasma environment in the assembly zone, allowing precise control over the energy and material fluxes directed towards the evolving nanostructures for sustained gram-scale (30 mg min^{-1}) production of graphene and allied derivatives from a low-cost feedstock of ethanol and acetonitrile. Moreover, plasma-assisted vertically-aligned growth is not limited to carbon-based nanostructures and it has been successfully used in the growth of vertically aligned metal oxides, nitrides, and chalcogenides[168,199–206] as well as polymeric and heterostructures.[207,208]

Plasma-assisted CVD of functional inorganic materials with specific composition, phase, morphology and microstructure has led to promising applications in integrated electronics, energy storage and conversion, catalysis, and sensors.[106,168,209–211] Among chalcogenides, transition metal dichalcogenides (TMDs) present unique properties depending on their polymorphic phases, such as 1T (metallic), 1T′ (semimetal-like), and 2H (semiconductor).[212] In recent years, the fabrication of phase-pure and polymorphic heterostructures of these compounds has been realized by temperature-controlled plasma-assisted sulfurization/selenization of metal.[84,89,110,200,210,213–218] Kim *et al.*[201,210] reported an optimized PECVD system with Ar + H_2S plasma for 1T-WS_2 and 1T-MoS_2 synthesis, which is otherwise challenging due to their metastable nature. The pre-deposited metal was sulfurized by accelerating the H_2S^+, ionized through the penning effect, in the plasma (positive) to the substrate (relatively negative) by the electric field in the sheath region. The ion bombardment caused the metal layer to break into nanocrystals and the H_2S^+ simultaneously penetrated it for efficient sulfurization. Unlike the microcrystalline nature of the deposits obtained from other chemical methods, the nanocrystalline structure of 1T-TMDs obtained from PECVD transformed it from metastable to a highly stable 1T phase structure with a lower surface energy than the 2H phase. However, in plasma-assisted sulfurization/selenization at higher temperatures, the 2H phase is predominantly formed.[89,219]

PECVD has been proven to be a convenient method for the fabrication of few-layer TMD–TMD heterostructure interfaces that exhibit interesting properties for diverse applications, due to their uniform band edges and tunable band gap through numerous layers.[200,220] Kim *et al.*[221] executed Ar plasma-induced phase transformation of SnS_2 to SnS for the fabrication of a vertical SnS–SnS_2 p–n junction heterostructure. The bombardment of Ar^+ radicals on the SnS_2 surface preferentially cleaved Sn–S bonds leading to selective etching of more volatile sulfur, thereby inducing the formation of the SnS phase. Similarly, Li *et al.*[222] reported fabrication of a vertical SnSe/$SnSe_2$ p–n heterojunction by NH_3 plasma-induced phase transformation. Seok *et al.*[200] reported wafer-scale MoS_2–WS_2 vertical heterostructures *via* a single-step plasma sulfurization of sequentially deposited seed layers of W and Mo (1 nm each) onto the SiO_2/Si substrate. By optimizing the plasma and deposition temperature, Seok *et al.*[220] reported wafer-scale growth of phase-selective 1T-MoS_2/1T-WS_2 or 2H-MoS_2/2H-WS_2 vertical heterostructures. Likewise, Sino *et al.*[213] demonstrated a similar top-down approach for high-yield MoSSe asymmetric structures from MoS_2 flakes where plasma-assisted selenization resulted in a Janus MoSSe layered structure at low temperature (200 °C) and a polymorphic alloy MoSSe at high temperatures (400–600 °C). Moreover, plasma-assisted sulfurization/selenization has also been extended for the fabrication of heterostructures of TMDs with metal oxides and carbides.[110,218,223,224]

For the fabrication of photovoltaic devices, PECVD is extensively employed in the deposition of antireflection coatings, passivation layers, dielectric layers, and so on.[60,225–228] To ensure high throughput, avoiding the standing wave effect in a large-area uniform deposition process, it is essential to control the spatial distribution of plasma parameters and the complex interplay of plasma physics and chemistry with the deposition-chamber dimensions. Accordingly, numerous theoretical and experimental studies have been performed to address the uniformity of plasma over a large area.[122,229] Zhang *et al.*[229] investigated the plasma density distribution under different voltage and pressure conditions in a H_2 capacitively coupled plasma (CCP) discharge sustained by multiple consecutive harmonics. Using a 2D fluid model, Kim *et al.*[230] analyzed the nature of the substrate and reactor sidewall material on plasma density distribution in a CCP reactor. They also investigated the role of dilution gas in the spatial distribution of the plasma parameters in a CCP reactor.[231] Similarly, in deposition of hydrogenated nanocrystalline silicon oxide (nc-SiO_x:H), Yu *et al.*[100] designed an industrial-scale VHF PECVD system with a minimized standing wave effect, by using a curved electrode and a glass plate over it, thus reducing the degree of non-uniformity for VHF1 (27 MHz) and VHF2 (40 MHz) to ±4.6% and ±10%, respectively, as against to ±27% and ±70%, for the same frequencies using a flat electrode configuration and without a glass plate. As a result, the thickness uniformity was improved in nc-SiO_x:H layers. When employed in a metric 6 mm screw thread (M6)-size bifacial silicon heterojunction solar cells with silver electrodes, high power conversion efficiency with a narrower distribution range (25.7–25.9%) under VHF1 was observed as compared to the VHF2 (25.3–25.9%). On replacing the Ag with Cu electrodes, the device displayed a power conversion efficiency of 26.41%. Besides enhancing the growth rate, dual-frequency PECVD operations have effectively improved film stress, chemical composition, step coverage, and stability.[37,126,232,233]

As plasma characteristics are highly dependent upon plasma sources or/and coupling mechanisms, some desirable effects for specific applications may be attained only by a particular plasma source.[32] For example, during the growth of carbon nanostructures using an RF plasma source, the ICP led to vertical graphene, whereas the CCP led to carbon nanotubes (CNT) due to the coupling mechanism affecting the plasma density.[234] From the standpoint of innovation in plasma processing and confinement for PECVD, magnetized plasma sources such as helicon wave plasma (HWP) and electron cyclotron resonance plasma, in which the excited electrons are launched as spiral beams along the MF lines as a function of the MF and excitation frequency, enable a resonant-like increase of plasma density useful in various applications.[235–239] The HWP source, with its electrodeless and magnetized plasma features, has provided an important means to regulate the energetic ion-bombardment flux on the stress level, structure, and resulting properties of the deposited films. Along with the flow rate, parameters – RF power and MF strength – can be used to regulate the high-density HWP.[240] Accordingly, HWP-CVD is employed for the deposition of carbonaceous,[42,239,241–243] metal carbide,[244,245] and metal oxide[246] coatings. During PECVD of DLC coatings, high plasma density of HWP enabled a high growth rate.[247,248] Qian *et al.*[249] reported room temperature PECVD of DLC in HWP with different magnetic field ($B_0 = 1200$–2400 G). The optical emission spectroscopy analyses indicated that the precursor decomposition followed the pathway ($CH_4 + e^- \rightarrow CH_3 + CH_2 + CH + C + H$), along with the formation of C_2 species by the recombination of CH_4 and other C-containing radicals. An increased MF provided high plasma density for achieving a higher growth rate. The C_2 and CH emission intensities increased to a maximum value at $B_0 = 2100$ G, leading to an enhanced deposition rate (800 nm min^{-1}) and sp^3/sp^2 ratio, as numerous energized H atoms generated by HWP helped in graphitic carbon removal and hydrogen incorporation.

An electron cyclotron resonance plasma source is another example where MF-assisted electron confinement plays a key role in plasma density enhancement, influencing the PECVD growth rate.[236,238,250,251] For example, during epitaxial growth of silicon thin film, the MF variation shifted the ECR plasma zone close to the SiH_4 outlet, causing increased concentration of free radicals responsible for deposition and resulting in an increased growth rate.[236] Nevertheless, the MF-assisted plasma confinement for enhanced growth and/or microstructural evolution has not been limited to a magnetized plasma sources alone, as demonstrated by Miller *et al.*[237] with an RF-powered hollow cathode PECVD system for DLC films. The MF applied *via* an electromagnetic coil around the hollow cathode tube influenced the magnitude of cathode DC self-bias, with an MF of ~95 G inducing maximum DC self-bias, indicating an optimal gas ionization that was independent of the applied RF power. Similarly, in a CCP system, the application of an MF (typically order of $\sim 10^2$ G) parallel to the electrodes normally enhanced the performance of CCP, although stronger MF may cause plasma non-uniformity.[252] Moreover, combined plasma, magnetic and electric field (substrate bias voltage) modulation to control the number of electrons and their movement path, influencing the ability of electrons to collide and ionize the gas for the deposition of DLC films is reported.[91] Nevertheless, recently, some efforts focusing on plasma diagnostics and measurement of flux and energy of plasma and reactive species in magnetically confined plasma have been reported,[252–256] which could be valuable for a better understanding of plasma chemistry to design suitable deposition conditions for film growth and microstructure.

In recent years, the requirements of fast processing with minimal crystalline defects in many device fabrication processes with enhanced plasma density at controlled ion-bombardment have prompted the testing of a variety of plasma excitation and delivery methods, such as gas-jet electron beam plasma,[257–260] hallow-anode plasma,[45,261,262] and radical injection plasma.[45,263–266] There have been reports on the usage of highly ionized plasma, designed using continuous or pulsed high power schemes and often coupled with substrate bias to impart a high degree of energetic bombardment, influencing the deposition conditions and resultant phase, microstructure and quality.[267–270] High-power plasma conditions involving excited ions with high power densities and ion energy have been important in the 3D growth of carbon nanostructures (thickness, branching, alignment height, *etc.*).[271] For example, the nucleation of carbon nanowalls in the initial growth period occurred only under optimal balance between ion and radical fluxes, with ion bombardment modifying the surface adsorption mechanism from physical to chemical.[266,272] It is important to mention here, however, that although it is generally accepted that high ion energies (~200–250 eV) and ion fluxes (~3.3–3.8

μA cm^{-2}) are necessary to induce nanowall deposition, there are many reports of PECVD growth of nanowalls in low-energy ions, following a different growth mechanism.[59,273,274]

Plasma-enhanced chemical vapor deposition is also extended to the deposition of organic polymer films as an initiated-PECVD (i-PECVD) process where usually a plasma of low power density is used for quasi-selective breaking of the weak peroxide bond (O–O) in the initiator molecules, facilitating subsequent polymerization of monomers.[275–280] Alternatively, i-PECVD is also performed directly with monomers only, without using any initiator.[281,282] However, limiting the purview of this review, the reader is referred to the existing literature[283,284] for detailed information. Similarly, as an alternative to plasma-assisted precursor decomposition, localized substrate-heating by a high-energy (often in the keV range) focused ion or electron beam is used, enabling nanoscale-level control over the material fabrication in CVD. For detailed information about such focused ion/electron beam-assisted CVD, relevant ref. 285–290 can be referred to. Here, the recent reports of plasma electron-assisted CVD of metallic films[105,291–293] are notable, which rely upon electron-induced redox chemistry, unlike the thermal effects in focused ion/electron beam-assisted CVD.

2.3 Perspective on plasma-enhanced chemical vapor deposition

Modulations based on nonconventional energy vectors (plasma and photons) and fields (electric field and magnetic field) have significantly enriched the landscape of CVD, enabling the facile deposition of unique nanoarchitectures with desired properties at significantly low temperatures and faster rates compared to the conventional thermal CVD. The use of auxiliary gases along with the key precursor to generate a special collection of plasma and reactive species in the reactor has constantly been popular, enabling lowered deposition temperature and/or increased deposition rate.[74,189,190,294] Future opportunities lie in designing novel configurations of plasma power, precursor and reactor design, controlling the plasma parameters (energy density and the composition and density of species such as photons, ions, excited fragments, *etc.*) for better control over the kinetics and imparting added functionalities (vacancies, dopants, *etc.*) in the deposited materials. With a judicious selection of plasma chemistry and substrate attributes, for example, PECVD can perform area selective deposition.[98,293,295–298] PECVD has been more focused in utilizing the energy of plasma electrons, often ignoring the role of ionic species, which can be partially due to the emergence of related technology of plasma-immersion ion implantation and deposition. Increased attention towards tuning the plasma ionic species can provide an additional degree of freedom for influencing the properties of the thin films grown by PECVD.[37,299,300]

Given the fact that the plasma-assisted processes are quite complex and involve numerous physical and chemical processes, the study of the deposition and growth mechanism has always been challenging. Additionally, most of the reported data on PECVD are largely based on the in-house plasma source and reactor, making the comparison of data somewhat challenging. Therefore, generalized relations between film characteristics and growth parameters such as temperature, dosage of precursors and carrier gases, and plasma power are still less established to date, hindering its utility in large-scale production of advanced materials and devices for specific applications. To overcome this, greater attention on establishing a generalized and direct correspondence between the plasma state, thermodynamic conditions and characteristics of deposited structures is required.

3 Photo-assisted chemical vapor deposition

3.1 Photoirradiation-matter interaction during chemical vapor deposition

Photoirradiation-based processing serves various applications, including deposition, doping, chemical etching and ablation.[301–303] Photo-assisted or photo-initiated CVD utilizes photons generated from sources such as gas discharge lamps, inert gas-ion lasers, solid-state lasers, or excimer lasers to drive precursor decomposition. Typically, photons in the visible or ultraviolet (UV) spectrum (wavelength ∼100–700 nm) are used, though infrared (IR) lasers are occasionally employed for precursor decomposition.[304,305] Precursor decomposition may occur through thermal effects (pyrolytic decomposition), non-thermal effects (photolytic/photochemical decomposition), or by a combination of both photophysical processes.[306,307] In addition to temperature, factors such as pressure, nature of the reactant, and thermal conductivities of the substrate, gas, and resulting deposit also influence the deposition rate during the pyrolytic process.[308]

In the pyrolytic process, a suitable laser is typically used to heat the substrate locally, creating a Gaussian distribution of irradiance on the focused region. This ensures that only the central part of the focused spot reaches the desired temperature for precursor decomposition and deposition. Conversely, in the photolytic process, directed radiation activates precursor molecules (*e.g.*, AB) on the substrate or in the gas phase (eqn (3)), leading to dissociation (eqn (4)) or reactive dissociation (eqn (5)), resulting in decomposition and deposition.

$$\text{Absorption: AB} + h\nu \rightarrow \text{AB}^* \tag{3}$$

$$\text{Dissociation: AB}^* \rightarrow \text{A} + \text{B} \tag{4}$$

$$\text{Reactive decomposition: AB}^* + \text{D} \rightarrow \text{E} + \text{F} \tag{5}$$

Additionally, if the energy supplied by the UV lamp or laser is high enough, ionization (eqn (6)–(8)) and radical formation (eqn (9)) are concomitant reactions, leading to the formation of reactive species.[309,310]

$$\text{Ionisation: AB} + h\nu \rightarrow [\text{AB}]^+ + \text{e}^- \tag{6}$$

$$\text{AB} + h\nu \rightarrow \text{A}^+ + \text{B} + \text{e}^- \tag{7}$$

$$\text{AB} + h\nu \rightarrow \text{A}^+ + \text{B}^- \tag{8}$$

$$\text{Radical formation: AB} + h\nu \rightarrow \text{A}^\bullet + \text{B}^\bullet \quad (9)$$

In the photolytic process, precursor decomposition can occur at temperatures significantly lower than the pyrolysis temperature. This is achieved through energy transfer from the excited electronic states to the vibrational states of the precursor molecules.[311] The fraction of excited molecules undergoing bond dissociation and the corresponding reaction rate (R_a) can be represented using a modified Beer's relationship, eqn (10)

$$R_a = (I_0/h\nu)F\exp(-\sigma_\lambda pl/kT) \quad (10)$$

where I_0 is the incident UV intensity, $h\nu$ is the photon energy, F is the photochemical quantum efficiency, k is Boltzmann's constant, σ_λ is the absorption cross-section for incident wavelength λ, p is partial pressure, l is the optical path length, and T is the absolute vapor temperature.[312] In the pyrolytic process, decomposition occurs at the substrate surface, and the deposition rate is kinetically controlled, with a high activation energy (E_a) of ~100 kJ mol^{-1}. In contrast, photolytic decomposition occurs in the gas phase where the deposition rate is diffusion-controlled, with a significantly lower E_a of ~10 kJ mol^{-1}.[313] Additionally, the absorption of incident radiation by the substrate, such as a semiconductor, alters its surface charge state, which can induce catalytic activity, promoting reactions between the organic ligands of metalorganic precursors to form stable by-products or leaving groups. Their desorption facilitates enhanced film growth at temperatures much lower than those required for conventional thermal CVD.[314]

Photolytic PACVD typically employs vacuum ultraviolet (VUV, wavelength <200 nm) lamps or lasers, emitting high-energy (5–15 eV) photons capable of cleaving most chemical bonds, as the initiation source. However, the limited light transmission at these wavelengths necessitates specialized reactor windows, such as MgF_2 and LiF, or advanced reactor designs. To overcome these limitations, short-wave UV light (200–280 nm) is often used, which can be transmitted through cost-effective quartz windows. This approach requires careful selection of precursors with reactive chemical bonds that can be activated at these wavelengths. To broaden the range of applicable precursors, especially for the deposition of polymers, photosensitizers and/or photo-initiators are used along with the monomers.[315]

3.2 Overview of photo-assisted chemical vapor deposition

The PACVD technique was initially developed to meet the demands of the semiconductor and microelectronics fabrication industry. Early reports of pyrolytic laser-assisted CVD (LACVD) include the deposition of silicon using a 50 W infrared CO_2 laser[316] and the deposition of carbon using a visible Ar^+-ion laser.[317] Important studies by Liu *et al.*,[318,319] Ruzin and Nemirovsky,[320] Irvine *et al.*,[321] and Santos *et al.*[322] explored the theoretical and mechanistic aspects of LACVD. Comprehensive discussions of the key principles underlying PACVD can be found in earlier reference works.[312,323,324] Similarly, reviews by Sankur,[325] Zhao *et al.*,[22] and Hwang *et al.*[326] provide valuable insights into the advancements and applications of PACVD. Table 2 presents selected reports on PACVD, displaying its importance in thin film fabrication for a range of materials.

Photo-assisted CVD has been widely used for the deposition of metals,[351] oxides,[352] carbides,[334] nitrides,[311,347] carbonitrides,[334] and organic polymers,[353] targeting applications such as coatings and functional materials. PACVD has demonstrated significant versatility in tailoring the characteristics of deposited materials by independently or synergistically modulating the characteristics of photo-radiation such as intensity or source type, or integrating it with substrate heating or PECVD processes. Akazawa *et al.*[354,355] reported increased reactivity of the GeH_4 precursor in PACVD of germanium on an SiO_2 substrate using a VUV beam as the heat source, due to its gas phase photolytic decomposition. Lari *et al.*[356] reported a continuous aerosol photopolymerization technique for coating nanoparticles, where photosensitive nanoparticles initiated surface photopolymerization of monomers onto their surfaces. Kasparek *et al.*[357] studied the influence of different VUV sources on thiol-terminated films deposited from C_2H_2 + H_2S gas mixtures, indicating that the absorption coefficients of gases significantly affected the photolytic reaction kinetics and resulting film composition.

Photo-assisted MOCVD has resulted in the deposition of oxide films (TiO_2, NiO, ZnO, and NiZnO) with improved crystallinity.[339,343,358,359] It also provided a convenient method for depositing metals at a reasonable growth rate on thermally delicate structures, such as self-assembled monolayers.[337] McElwee-White and coworkers extensively investigated the photochemistry of suitable precursors,[337,351,360–362] indicating that the secondary photo-processes often strongly influenced the overall efficacy of precursor decomposition.[337]

In laser-assisted CVD, depending upon the laser fluence and mode of its application (direct or parallel to substrate, scan speed, *etc.*), the laser-matter interaction can be expressed *via* laser pyrolysis,[332,363,364] laser photolysis[328,365–367] or laser resonance sensitization.[368–370] LACVD displayed its utility in the fabrication of thin films of metals,[371–373] oxides,[338,344] nitrides,[152,308,311,347,374] carbides,[375] sulphides,[376–378] carbon-based materials,[329,331,379] and composites.[334,380,381] Several general or material-specific reviews highlight the versatility of LACVD.[307,370,379,382–388]

Odusanya *et al.*[331] investigated the role of deposition parameters (gas flow rate, temperature, laser power, time, substrate) in a pulsed laser-assisted CVD of carbon nanomaterials. Um *et al.*[379] reported laser-assisted direct writing of >10 nm thick highly-ordered graphite film on a Ni substrate. Wu *et al.*[329,389] utilized femtosecond laser texturing of metal substrates to improve the adhesion of diamond coatings in laser-assisted combustion flame CVD. Moreover, laser-assisted photolysis of hydrocarbon precursors has been shown to effectively suppress nondiamond carbon formation and promote preferential crystallographic orientation in CVD diamond.[327,328,390]

Tu *et al.*[342] reported LACVD of HfO_2 films *via* a single growth process using an InGaAlAs diode laser that created a lateral temperature gradient (100 K mm^{-1}) over the Si(100) substrate and resulted in four regions with different deposition

Table 2 Selected examples of photo-assisted CVD used for the deposition of functional coatings of various compositions[a]

Material/substrate	Photon source/reaction	Key features	Application	Ref.
Carbon-based materials				
Diamond/Si (100)	Laser (wavelength: 532 nm)/photolytic	Coupling of laser with PECVD for increased crystal growth	Coatings; hardness = 91 GPa, Young's modulus = 721 GPa	327
Diamond/WC or cobalt	UV laser (wavelength 193 and 248 nm)/photolytic	Nondiamond carbon accumulation was minimised	—	328
Diamond/SS 316	CO_2 laser	19 μm-thick diamond coating with a quality factor of 96%	Coatings; enhanced adherence with metallic substrate due to stress relief and improved mechanical bonding	329
Diamond/WC	Wavelength-tunable CO_2 laser	Enhanced growth rate by resonant vibrational excitation of the CH_2-wagging mode in C_2H_4 molecules	Synthetic diamond; grain size without laser (2.6 μm) increased to 10.494–14.3 μm with laser	330
Carbon-based materials/Si or Cu	Nd:YAG laser	Pulsed laser CVD; Cu foil was a more suitable substrate to grow pyrolytic carbon than SiO_2	Pyrolytic carbon with graphene as its fundamental building block	331
Metalloids				
SiOC–SiC/graphite	CO_2 laser/pyrolytic	Temperature-dependent auxiliary formation of amorphous SiO_2, β-SiC nanocrystals, and/or Si crystals	—	332
3C–SiC/Si (001) epitaxial films	YAG diode laser	Density of microtwins was controlled by dilution gas (H_2) flow	—	333
SiC–TaCN/Si_3N_4	Nd:YAG laser	For 1000 °C deposited film, hardness and Young's modulus ≈30.4 and ≈232 GPa, respectively	Tribological coating; (extreme penetration = 59.0 μm and surface roughness = 3.5 μm)	334
Silicon nitride	InGaAlAs diode laser/photolytic	Lowest deposition temperature (1100 °C) so far for crystalline film; max. rate 972 $\mu m\ h^{-1}$ at 1300 °C	Coatings; Vickers microhardness and nano-hardness 25.1 GPa and 34.8 GPa at 1300 °C, respectively	308
SiN encapsulation film	ArF excimer laser	Two-step fabrication of SiN film using LACVD and LAPECVD	Thin-film encapsulation for organic light emitting diodes (encapsulation increases lifetime by 3.59 times)	335
Boron carbon oxynitride/Si	Nd:YAG laser, 1050 °C; TDMAD precursor	Composition $B_wC_xN_yO_z$ was varied by regulating the flow rate of the oxidation gas (*i.e.*, air)	Phosphor; PL emission bands at 386–570 nm; intense emission bands at 534 and 570 nm for C- and O-rich films	336
Metals, oxides, chalcogenides, nitrides				
Ru on thiolated self-assembled monolayers (SAMs)	Hg arc lamp	Ru and RuO_x deposit on $-CH_3$- and –OH-terminated SAMs; no deposition on –COOH-terminations	—	337
N-doped α-Fe_2O_3/Si	Ar^+ laser/pyrolytic; pulsed Nd:YAG laser	Ar^+ laser for deposition and pulsed Nd:YAG laser for crystallization and minimize the surface irregularities	Magnetic devices and photoelectrodes	338
Li-doped NiZnO/*c*-axis oriented sapphire	Tungsten–halogen lamp (cutoff wavelength ∼200 nm)	Compared to CVD, PACVD results in decreased defect density and lattice stress	Optoelectronics; NBE/DLE ratio = 15.6 for PACVD compared to that of 3.2 for CVD	339

Table 2 (*Contd.*)

Material/substrate	Photon source/reaction	Key features	Application	Ref.
$SmBa_2Cu_3O_{7-\delta}$/$LaAlO_3$	Semiconductor laser, (wavelength: 808 nm)	P_{O_2} dependence of deposition rate, critical temperature (T_c) and critical current density (J_c)	Superconductive films; highest T_c (89.2 K) and J_c (2.04 MA cm^{-2}) for film deposited with $P_{O_2} = 200$ Pa	340
Eu^{3+}-, Dy^{3+}-, or Tb^{3+}-doped $HfTiO_4$/quartz	Diode laser (continuous-wave mode; 1470 nm; 75 W)	Fast deposition rate (36 μm h^{-1})	Phosphor; Eu^{3+}, Dy^{3+}, and Tb^{3+} activated films displayed red, yellow, and green photoluminescence	341
HfO_2/Si(100)	InGaAlAs diode laser/pyrolytic	Max. deposition rate (362 μm h^{-1}) was 10^2–10^4 times higher than that obtained using existing methods	High-dielectric constant (k) material; $k = 16$–22	342
Arsenic doped p-type ZnO/($GaAs/Al_2O_3$)	Tungsten–halogen lamps (∼200 nm cutoff; total input power 600 W)	The GaAs layer acted as a doping source and its thickness controlled the doping level	Photoelectric device; hole concentration 3.1×10^{16} to 2.4×10^{17} cm^{-3}	343
Tb^{3+}-,Eu^{3+}-doped YAP/(100) $SrTiO_3$	CO_2 laser (10.6 μm; 60 W), ZnSe window	Deposition rate (53 μm h^{-1}) 50–90 times faster than for thermal CVD at 900–1003 °C	X-ray scintillation screen; fluorescence decay constants 1.89 ms (Tb^{3+}:YAP) and 1.96 ms (Eu^{3+}:YAP)	344
Ce^{3+}-,Eu^{3+}-doped YAG-Al_2O_3 ordered eutectic system	CO_2 laser (10.6 μm; 60 W), ZnSe window, 791–1030 °C	First report on the formation of an α-Al_2O_3 rod-like structure in the YAG-Al_2O_3 composite	X-ray scintillation screen	345
Al-doped β-Ga_2O_3/*c*-axis oriented sapphire	CO_2 laser (10.6 μm; 60 W), 750–900 °C	Fast epitaxial deposition (15 μm h^{-1})	X-ray scintillation screen; scintillation light yield = 5400 photons per 5.5 MeV, decay response = 5.1 ns	346
Gallium nitride/(0001) GaN-on-sapphire	CO_2 laser (9.219 μm; 250 W)/photolytic	∼60% reduction in carbon impurity incorporation (5.5×10^{15} cm^{-3}); (max. growth rate 4.5 μm h^{-1})	Electron mobilities were 600–750 and 750–1275 cm^2 V^{-1} s^{-1}, respectively, for normal and laser-assisted growth	311
GaN/GaN	CO_2 laser (9.219 μm; 200 W)/photolytic	High laser power suppressed the incorporation of carbon impurity	Trap concentrations were higher in laser-assisted GaN (up to 2×10^{15} cm^{-3})	347
Others				
Poly(HEMA-*co*-4VP)/electrospun *c*PCL	UV lamp, *tert*-butyl peroxide as initiator	piCVD-assisted crosslinking	Polymer degradation and drug delivery	348
Oligomeric film on CNTs	Short-wave UV lamp/photolytic, H_2O_2 initiator	piCVD; vertical chemical gradient formation to control hydrophilicity/hydrophobicity	Surface modification (wettability control)	349
Janus HEMA-PTFE membrane	UV (254 nm)/photolytic	piCVD	Membrane distillation (antifouling effect)	350

[a] DLE – deep level emission; HEMA – 2-hydroxyethyl methacrylate; NBE – near-band-edge emission; PTFE – polytetrafluoroethylene; P_{O_2} – oxygen partial pressure; PL – photoluminescence; TDMAD – tetrakis(dimethylamino)diboron; YAP – yttrium aluminum perovskite; YAG – yttrium–aluminum garnet.

temperatures (Fig. 4). The four regions followed different deposition kinetics, resulting in differential phase, microstructure, and morphological developments in these regions. The maximum deposition rate was 10^2 to 10^4 times higher than that in previously reported deposition methods. On the other hand, Zhang *et al.*[380] achieved a vertical temperature gradient between the top and bottom of the coating during the growth of graphene/SiC composites over Si nanowires. The light-trapping structure of nanowires enabled full utilization of the photothermal effect of the laser at the top of nanowires, resulting in a larger surface area in the deposited film.

Zhang and coworkers[380,391–393] utilized LACVD to fabricate graphene/cubic silicon carbide (3C–SiC) composite films using hexamethyldisilane as a single precursor. In these composites, the formation of graphene relied on the multi-step decomposition of hexamethyldisilane, depending on the deposition temperature and pressure:[391]

At lower deposition temperature and high pressure (*i.e.* at lower phonon energy per hexamethyldisilane molecule), hexamethyldisilane decomposition mostly proceeded to step (2), resulting in a graphene-rich graphene/3C–SiC composite. However, at high deposition temperature and low pressure (*i.e.* at sufficient phonon energy per hexamethyldisilane molecule), complete decomposition of hexamethyldisilane ensured sufficient supply of [$(CH_3)_n$–Si] clusters, resulting in pure epitaxial SiC films. A high distribution of graphene at the bottom of the film in transmission electron microscopy (TEM) analysis further supports this mechanism, as the formation of graphene predominantly occurred in the early stages of the heating ramp.

Laser-assisted CVD has emerged as a preferred method for the maskless fabrication of microdevices.[307,364,379,394] Laser-assisted vapor phase epitaxy, a variation of LACVD, resulted in selected area epitaxial growth of high structural and optical quality layers of III–V compound semiconductors, without masking or surface structuring.[395] LACVD has achieved a growth rate of ~84 μm h^{-1} compared to ~2–3 μm h^{-1} in normal CVD for the deposition of gallium nitride (GaN) transistors and diodes.[347,396] In CVD of GaN using ammonia as a nitrogen source, poor decomposition efficiency of ammonia leads to abundant carbon impurities. Conventional approaches to overcoming carbon impurities, such as increased carrier gas flow and high NH_3-to-Ga precursor ratio, have negatively affected the growth rate. LACVD has helped solve this issue without compositing with the growth rate. For example, by using a high-power CO_2 laser in LACVD of GaN film from a trimethylgallium precursor, Zhao and coworkers[311,397] achieved >60% reduction in carbon content with a high growth rate (4.5

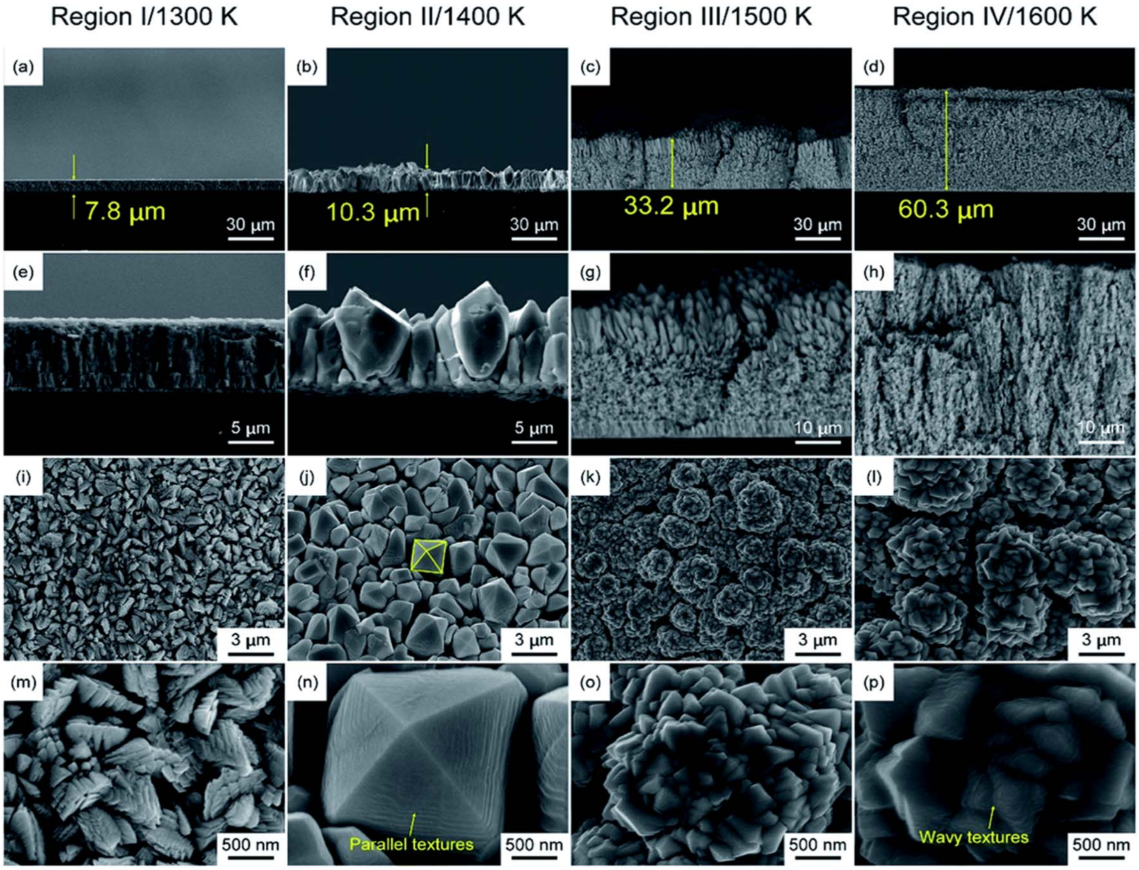

Fig. 4 SEM images of the cross-sections and surfaces of HfO_2 films in the four regions, obtained using the high-throughput growth process. (a), (e), (i), (m) region I at $T = 1300$ K, (b), (f), (j), (n) region II at $T = 1400$ K, (c), (g), (k), (o) region III at $T = 1500$ K, (d), (h), (l), (p) region IV at $T = 1600$ K, respectively. T represents deposition temperature, reused with permission from Royal Society of Chemistry.[342]

μm h^{-1}). A strong interaction of the CO_2 laser with NH_3 molecules at a wavelength (9.219 μm) matching with the rotational–vibrational transition of N–H wagging mode (1084.63 cm^{-1}) of NH_3 facilitated the NH_3 decomposition.[311]

Laser-assisted PECVD (LAPECVD) processes are developed for electronic and optoelectronic applications to avoid key drawbacks of PECVD, such as ion bombardment-induced substrate damage, nonstoichiometric composition, and residual stress.[152,335] For example, Kim *et al.*[152] used an ArF laser along with the NH_3/SiH_4 plasma (Fig. 5(a)) for the dissociation of reactive gases during the deposition of silicon nitride films. The LAPECVD-grown film displayed increased deposition rate (Fig. 5(b) and (c)) and lower residual stress compared to the normal PECVD-grown film (Fig. 5(d)), due to the shift in composition towards the stoichiometric Si_3N_4. The LAPECVD-grown film displayed higher etching resistance due to the high film density resulting from its higher nitridation. Moreover, the organic light-emitting device employing the LAPECVD-grown passivation layer displayed improved performance without any electrical damage.

The initiated chemical vapor deposition (iCVD) is widely used for organic and hybrid polymer films, where thermal activation of a volatile initiator is employed to commence the polymerization of monomers.[353] In iCVD, thermal activation generally needs an active cooling strategy to keep the substrate temperature conducive for adsorption, which can be arduous for complex or poorly thermal-conducting substrates. To address this, initiation-polymerization can be achieved by gas phase or surface photoactivation of initiator/monomer(s) in photo-initiated CVD (piCVD), thus eliminating the requirement of high-temperature sources.[279,315] Typically, piCVD needs a judicious selection of a primary monomer reaction mixture, often without any initiator and sensitizer, based on its capacity to undergo photo-induced polymerization in the gas phase or onto the substrate. In recent years, piCVD has been widely used for the deposition of polymeric films and the surface functionalization of nanomaterials.[22,348,349,353,398] The utilization of photon energy to initiate and propagate the polymerization process in functional films for biochemical/biological applications has eliminated the requirement of potentially toxic initiators and crosslinkers.[348,399,400] The piCVD has been preferred for surface modification.[22,315,348,349,398,401] In this regard, to overcome the constraints of a limited range of photochemically active precursors, initiators and sensitizers, a syngas piCVD is proposed, where syngas (H_2 + CO) is photoexcited by short-wave UV radiation to produce radicals and reactive species.[315,398,402,403] Tavares and coworkers studied the kinetics of syngas piCVD,[315,402,404] and employed it for the deposition of thin films and surface treatment of polymers and nanoparticles.[398,405–407] The piCVD achieved large-scale (5 g) encapsulation of magnetic iron oxide nanoparticles in a jet-assisted fluidized bed configuration.[406] The piCVD is used to regulate the surface wetting behavior.[349,407,408]

Photo-assisted manipulations employing the ablation and annealing effects of laser are extensively used complementary to the main CVD process, influencing the composition, crystallographic orientation, and morphology of the substrate and

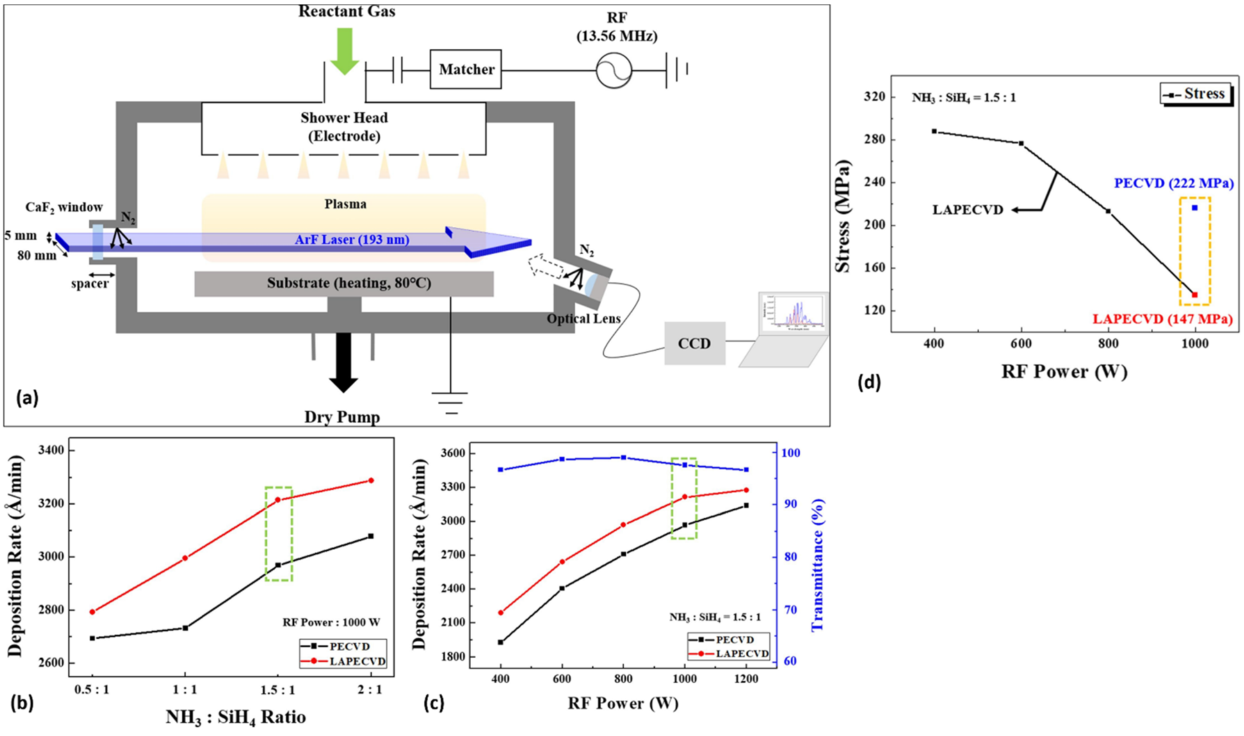

Fig. 5 (a) Schematic of the LAPECVD system; deposition rates for PECVD and LAPECVD, measured as functions of $NH_3 : SiH_4$ ratio (b) and RF plasma power (c); and (d) residual stress of silicon nitride films with plasma RF power, reused with permission from Elsevier.[152]

'preparing' it for the deposition of a desired material in the subsequent CVD step.[326,375,409,410]

3.3 Perspective on photo-assisted chemical vapor deposition

Photo-assisted manipulations in CVD enable the deposition of films and arrays with impressive substrate adhesion, high quality, and high deposition rate. Using PACVD, low-temperature deposition of selected area (using laser) and relatively large area (using UV lamps) film on thermally labile substrates is easily achieved. Unlike the PECVD where bombardment of aggressive plasma species may cause some damage to the film, PACVD-grown films are free from such artifacts. However, for using a VUV source, window composition has been one of the major factors in reactor design. The range of photolytic PACVD has been limited by the availability of photosensitive reactants. Photosensitizers and photoinitiators are employed to extend this range; however, their high cost is still a major constraint. The paucity of a universal and readily activated photoinitiator, such as the thermally activated peroxides in iCVD, is still a concern.

Syngas piCVD has been a convenient and economical method for organic film deposition and surface functionalization. However, it is limited to carbonaceous materials and requires further understanding of the role of syngas composition and iron species on deposition chemistry and kinetics. Moreover, organic substrates and deposited films can often be susceptible to photo-induced degradation, limiting the quality of the films.

PACVD and its variants provide a convenient method for the deposition over thermally delicate structures, such as self-assembled monolayers. However, to achieve this, the development of new precursors with a greater understanding of their photochemistry is desired. PACVD is not suitable for deposition on transparent substrates. Similarly, the importance of LACVD rests in ensuring selective area deposition; however, the area of deposition is limited by the laser spot size. The Gaussian distribution of irradiance around the focused spot even renders it less suitable for nanoscale direct writing over a large area. In this regard, plasmon-assisted CVD, suggested by Boyd *et al.*,[411] where localized heating induced by the surface plasmon of nanostructured metals is used for nanoscale heating and subsequent deposition, can be an alternative in some cases, especially where contamination by nanostructured metal layer is not an issue. However, a potential use of this Gaussian distribution of laser irradiance can be in creating a nanoscale temperature gradient during the molten metal-catalyzed growth of nanostructures. This, under some conditions, can manifest in interesting physicochemical effects on deposition and growth kinetics, *e.g.*, the Marangoni effect in SiO_2 during field-assisted CVD growth of CNTs[412] and in differential phase, microstructure, and morphological developments in HfO_2.[342] Moreover, the idea of using a laser for selective alteration of specific chemical bonds or excitation of vibration modes in reacting species and thus imparting chemical selectivity[413] is less explored in CVD and needs greater attention.

4 Electric field-assisted chemical vapor deposition

4.1 Electric field-matter interaction during chemical vapor deposition

The interaction of the external electric fields with matter (atoms or molecules) has a range of effects, with the Stark effect displaying the splitting of energy levels being the most prominent manifestation. Theoretical calculations suggest that an EF of 1–10 V nm^{-1} can alter the E_a of gas phase reactions by several kJ mol^{-1}. The application of such an intense EF on reaction volume is challenging due to the dielectric breakdown of the medium.[414] However, an externally controlled moderate EF provides efficient ways to alter the reaction chemistry *via* its direct interaction with the participating species (atoms, molecules, or other complex matter), influencing the electron transfer/charge migration, geometry and/or bond strength, and interfacial behavior.[415–417] When an external EF is coupled with the CVD process, the precursor molecules having a permanent or induced dipole interact with the field and gain kinetic energy, increasing their probability of reaching the substrate surface.[418] The gaseous precursor may assume a preferred orientation towards the substrate and, if EF is sufficiently strong, some of the bonds in precursors get activated along the direction of the dipole, reducing the energy of nucleation and executing a preferred growth orientation.[23]

During the CVD process, externally controlled electrical biasing of the substrate-containing electrode plays an important role in bias-enhanced nucleation (BEN)[90,419,420] and bias-enhanced growth.[421] In processes involving the gas phase formation of charged nanoclusters, the application of electrical bias directs these clusters toward the substrate, where they act as nucleation centers for deposition.[419] For example, during the deposition of diamond and carbon nanotubes, the gas-phase flux contains, respectively, the positively and negatively charged carbon fragments. Therefore, the substrates, which are negatively-biased (in diamond deposition) and positively-biased (in carbon nanotube deposition), promote nucleation and growth (Fig. 6(a)).[424–428] Additionally, the nature of external electrical bias (*i.e.*, DC/AC) has been an additional control parameter, with voltage and AC bias frequency significantly affecting the microstructure evolution and growth rate.[23,422,423,429]

From a non-classical nucleation point of view, the charged nanoclusters originating at the initial stages of precursor decomposition in CVD act as building blocks for 1D nanostructures such as nanowires and nanorods. For CVD growth of such nanostructures, the applied external electrical bias, apart from influencing their velocity and population at the substrate *via* a repelling or attracting influence, also provides directional control over the growing nanostructures.[430] For example, during EF-assisted growth of 1D materials such as CNTs, the dipole-induced torque directed the growing 1D nanostructure to align along the EF, enabling a sustained oriented 1D growth (Fig. 6(b)).[188,431] Similarly, external EF-induced *in situ* manipulation helped the formation of doped nanostructures, *e.g.*, by

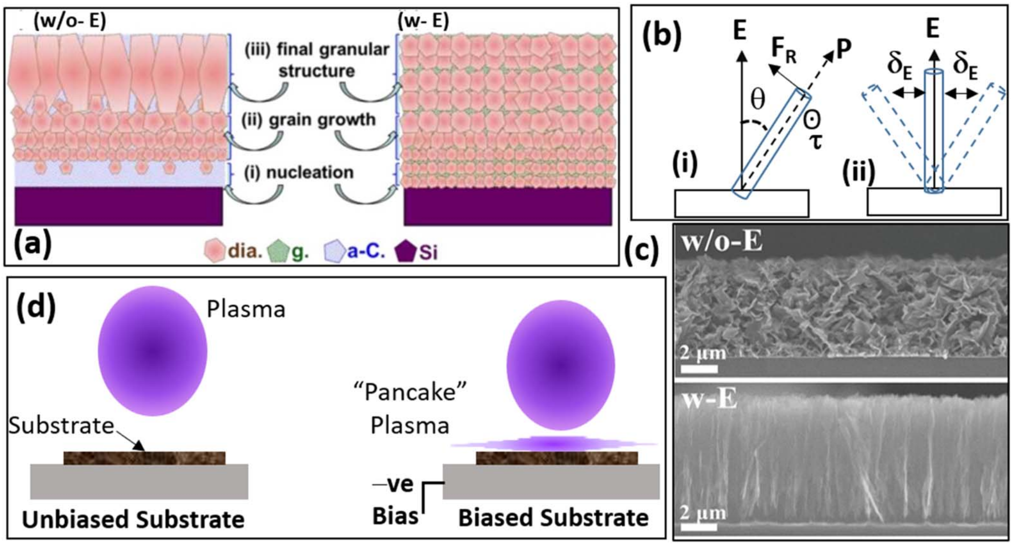

Fig. 6 (a) Schematics of the bias effect on the evolution process for the granular structure of diamond films with (w-E) and without (w/o-E) EF. The bias condition displayed an increased and instantaneous nucleation (i), moderate grain-growth (ii), and coexistence of some graphitic phase (iii), reused with permission from ACS;[421] (b) schematic showing a single-walled carbon nanotube in an EF (i) and its vibration in an EF (ii);[422] (c) SEM images showing the effect of EF on the growth of vertical graphene arrays and graphene nanowalls, reused with permission from Wiley;[188] and (d) effect of electrical bias on plasma appearance in PECVD of diamond films.[423]

inducing electromigration of dopant species,[432] and homojunctions, *e.g.*, by sequential growth of the Sb-doped p-type ZnO microwires (with EF) along the undoped n-type ZnO microwires (without EF).[433]

In PECVD, external EF has been used to influence the distribution of plasma around the substrate. The negatively charged plasma wall, due to the higher mobility of electrons compared to the ions, is attracted or repelled toward the substrate, depending upon the substrate bias (Fig. 6(d)). The external EF also led to the decoupling of ion flux and ion energy[251,263,434] and exerted control over the electric field concomitant with the plasma.[183,435,436] Such external bias-controlled ion energy and plasma flow characteristics have influenced various phenomena such as ad-atom migration, desorption, etching, and displacement of lattice atoms in the growing film, affecting its characteristics-growth rate, crystallinity, density, and stoichiometry.[437,438]

4.2 Overview of electric field-assisted chemical vapor deposition

The use of externally applied electrical bias in CVD can be traced back to the work of Sawabe and Inuzuka[24] on the hot filament CVD (HFCVD) of diamond film, displaying an increased deposition rate due to a 150 V bias-induced enhanced electron bombardment on the substrate surface. Yugo *et al.*[25,419] used an external EF-induced pre-deposition process to generate diamond nuclei under a minimum bias voltage of −70 V during the PECVD of diamond. Yoshimura *et al.*[439] reported the fabrication of molecular-aligned polymer film by employing a strong (0.78 MV cm^{-1}) external EF. The external EF-assisted CVD process gained momentum in the 1990s,[418,439–441] and was well-received during the 2010s.[23,433,442–454] It has been employed in CVD of metal[455] and 1D/2D materials (hexagonal boron nitride,[456] carbon microcoils and nanotubes,[28,457] and graphene[183]), AACVD of metal oxides,[449,453,454,458–461] and PECVD of microcrystalline silicon.[462] The EF assistance in CVD has been focused on manipulation of deposition and growth,[463] growth direction and crystallographic orientation in nanostructures,[183,433,454,464] defects,[435] and selective growth (phase composition and crystallinity).[431,433,465] Table 3 presents selected examples of EFCVD used for the deposition of functional coatings.

External EF assistance has shown a remarkable impact in aerosol-assisted CVD (AACVD) of metal oxides.[449,453,454,458–461] Beyond the magnitude and polarity of the applied bias, factors such as the type of current (AC *vs.* DC), frequency,[458] aerosol delivery setup and substrate orientation[461] significantly influence particle size and shapes, agglomeration, and phase composition and preferential crystal orientations.[453,454] The trajectory and flight time of aerosol droplets, charged either due to polarized molecules or static surface charges are influenced by the EF parameters. For example, in the deposition of WO_3 using the $[W(OPh)_6]$ aerosol in toluene, applying AC voltage rather than DC voltage resulted in aligned and evenly distributed fibrous growth. This is attributed to the higher impedance of AC fields, which prevents the rapid dissipation of induced dipoles in the growing material, thus maintaining the alignment of the fibers with the field.[458] In the CVD of β-Ga_2O_3 on a patterned sapphire substrate, external EF (0–80 V) was found to significantly affect the growth rate, morphology, and crystallinity.[450,465] The growth rate increased with increasing EF, forming uniform and regularly arranged microstructures. X-ray diffraction (XRD) analysis indicated increased preferential growth along the (−201) plane of the monoclinic crystalline phase of β-Ga_2O_3 with increasing external voltage.[465]

Table 3 Selected examples involving electric field-assisted manipulations in CVD of functional materials[a]

Material/substrate	Bias	Key effect of EF	Application	Ref.
Metal oxides, carbides, nitrides, *etc.*				
ZnO/Si	0–700 V	No deposition in the absence of EF; shape and size changes with increasing bias	—	466
β-Ga_2O_3/sapphire	0–80 V	Improved growth rate & crystal quality; a blue shift in absorption with increasing V	Direct wide band gap semiconductors; $E_g = 4.59$–4.94 eV	465
ZnO, CdO and PbO/fluorine-doped tin oxide (FTO)	~625 V cm^{-1}	EFCVD films displayed enhanced photocurrent in 0.1 M Na_2SO_4 compared to those deposited without EF	Photoelectrochemical; j values for ZnO, CdO and PbO in light and darkness were 207, 263, 237 and 1.55, 215, 1.67, respectively	463
VO_2/FTO	1–10 V cm^{-1}	Reduction in crystallite size and thermochromic transition temperature	Glazing material	452
TiO_2/glass	0–30 V	EF induced changes in particle size and shapes, agglomeration, and composition	Photocatalytic dye degradation	453
TiO_2/FTO	0–30 V	EF induced changes in particle size and shapes, and preferential crystal orientations	Antimicrobial and photocatalytic application	454
Silicon	±1000 V	−ve bias is more favorable than the +ve bias	—	467
SiC	±50 V	−ve bias promotes epitaxial growth	—	468
Carbon-based materials				
Vertical graphene (VG)/Si	0–60 V	EF assistance in PECVD; height of VG arrays increased with the bias (18.7 μm with an EF of 30 V cm^{-1})	Thermal interface material; high vertical thermal conductivity (53.5 W m^{-1} K^{-1}) and a low TRC (11.8 K mm^2 W^{-1})	188
Vertical graphene (VG)/Si	−60–250 V	EF assistance in PECVD; high growth rate (11.5 μm h^{-1})	Thermal interface material; vertical thermal conductivity (34.2 W m^{-1} K^{-1}) and a low TRC (18.2 K mm^2 W^{-1})	190
Vertical graphene/Cu	−400–400 V	Deposition rate decreased with increasing −ve bias but opposite effect with +ve bias	—	431
Vertical graphene	30 V cm^{-1}	Straight pore structure & enhanced electrochemically active surface area for efficient ion/electron transport pathways	Electrochemical capacitors; $C_a = 1.72$ mF cm^{-2} at $\Phi_{120} = 80.6°$ after 500k cycles, energy density = 0.33 μW h cm^{-2}	191
Quenched-produced diamond/Ti	−40 V	A spontaneously formed TiC interfacial layer caused a 3-fold increase in adhesion strength	Coatings for biomedical devices; hardness = 96 GPa	426
Diamond/Si(100)	150–250 V	Bias voltage plays a key role in the formation of azimuthally (70%) textured diamond film	Quantum devices; diamond films with N vacancy defect centres	90
Vertical graphene	100 V	EF-assisted PECVD; max. growth rate = 15.9 μm h^{-1}; VG height ~144 μm	Light shielding; ultra-low reflectance of 0.25%	189
Carbon nanotubes	0–30 V	Growth rate increased and diameter decreased with higher +ve voltage	EF-assisted mass production of CNTs	469
Carbon nanotubes	0–700 V	"Herringbone structure" (diameter 25 nm) in no field, uniform parallel to the tube axis (diameter 12 nm) in EF	Supercapacitor; $C = 237$ F g^{-1} (3-fold increase compared to no field)	470
"Cow-nipple-like" submicro-nano carbon	0–300 V	A vertically grown carbon nanotube (dia. 10–40 nm) upon a carbon ball (dia. 30–120 nm)	—	471
Others				
Perfluoropolyether on diamond-like carbon	0–300 V	An EF-modulated photoelectron-assisted CVD	Ultrathin perfluoropolyether/DLC hybrid coatings for magnetic disks	472

[a] C_a – specific areal capacitance; C– specific capacitance; j – photocurrent density (in μA cm^{-2}); TRC – thermal contact resistance.

The EF-assisted CVD processes have played an important role in understanding the non-classical charged nanocluster-based nucleation and growth. Hwang and coworkers[429,466–468,473–475] have studied the formation of charged nanoclusters and their deposition behavior under different bias conditions (substrate bias, filament bias in HFCVD, AC *vs.* DC bias) in CVD. In HFCVD of SiC, a negative bias of hot filament led to the formation of smaller charged nanoclusters compared to that in positive or zero bias, which displayed liquid-like properties and promoted epitaxial growth through epitaxial recrystallization.[468] In CVD of diamonds, the electrical bias accelerated the charged nanoclusters formed in the gas phase towards the substrate to act as nucleation centers and execute a bias-enhanced growth.[476,477] In the CVD process, diamond deposition is also accompanied by an undesirable graphitic phase and EF-assisted +ve substrate biasing suppresses this graphitic phase.[476] Wang *et al.*[427] studied the evolution of nucleation and growth of a heteroepitaxial single-crystal diamond film with substrate bias on an Ir substrate, displaying a close relation between bias voltage and bias time. The bias-enhanced nucleation experienced incubation and domain-nucleation periods where domains can enlarge and diminish with bias time, resulting in the nucleation pathways changing from "isolated-crystal nucleation" to "typical domain nucleation" and again back to "isolated-crystal nucleation".

In HFCVD of anisotropic carbon-based nanomaterials, the external electrical bias influences the deposition rate, composition, and orientation of growing nanostructures.[478,479] For example, during catalytic deposition, the axis polarizability of 1D-carbon nanostructures in EF has caused them to be lifted upward from the horizontal direction, enabling them to grow more readily from the catalyst surface.[443,470,480] Zhang and Pan[481] demonstrated a bias-dependent diameter variation of carbon nanofibers using Ni nanocatalysts. An external bias of 0, 25 and 50 kV m^{-1}, respectively, influenced the size of nanocatalysts, which become liquid at the deposition temperature, resulting in nanofibers with 19.2 ± 8.6, 13.8 ± 4.7, and 8.0 ± 2.4 nm diameter. Similarly, Peng *et al.*[443] exploited the greater polarizability of metallic-CNTs compared to the semiconducting-CNTs to raise the percentage of metallic-CNTs to 80% with EF-bias of 200 V cm^{-1} compared to that of 47% with zero field bias. Luo *et al.*[470] observed that the CNTs grown under EF displayed a smaller and uniform diameter, improved crystallinity and graphitic nature, and fewer graphite layers parallel to the tube axis. Issman *et al.*[464] used external EF for continuous alignment of CNT bundles (Fig. 7). The theoretical model simulating the alignment process indicated that a CNT stiffening effect (introduced by a *z*-pinch mechanism induced by the Lorentz force of the AC field, rather than DC fields) enabled a means to control CNT bundle diameters. The EF-assisted samples

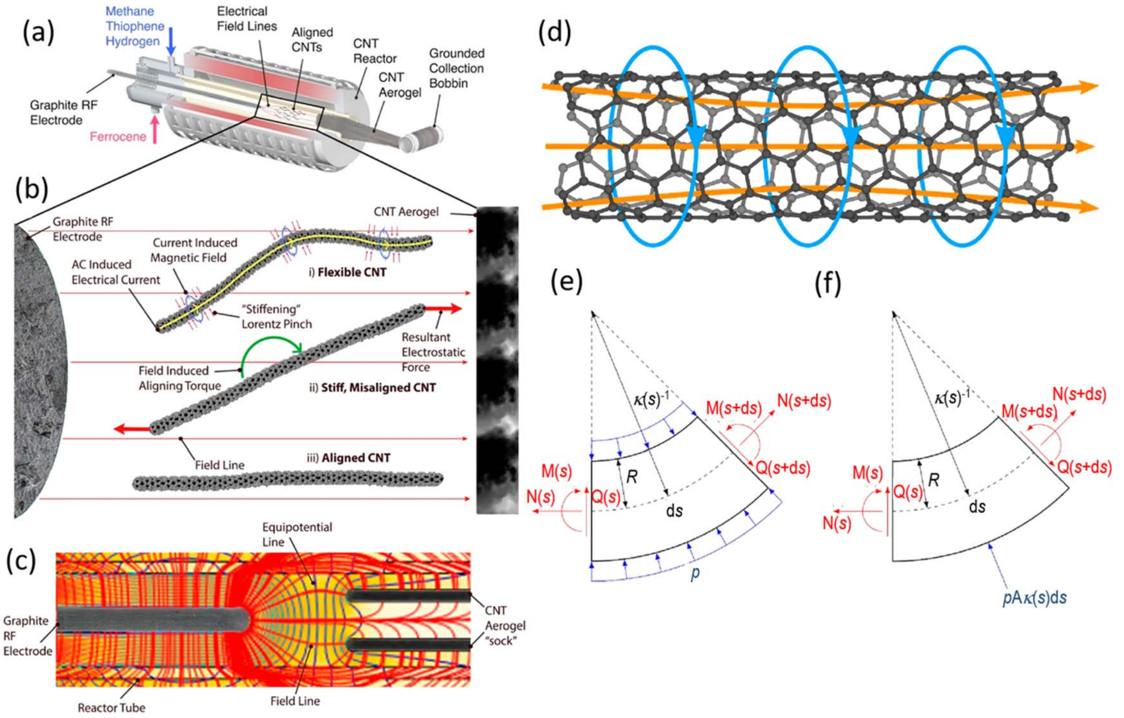

Fig. 7 (a) An illustration of an EFCVD reactor with an RF electrode inserted at its front, while the forming CNT aerogel acts as a counter electrode. (b) A magnified schematic shows the occurrence in the interelectrode gap: (i) AC field induced "Lorentz pinch" stiffens the ultralong CNT, (ii) Stiff, ultralong CNT is under the influence of a field-induced aligning torque, (iii) CNT is aligned according to the field lines. (c) Finite element method numerical results of field distribution inside the reactor tube portraying equipotential lines (blue) and orthogonal field lines (red). The packing density of the equipotential lines indicates the local field intensity. The model shows the presence of alignment-inducing field lines bridging the two electrodes within the interelectrode gap (50 mm wide). (d–f) Z-pinch mechanism, (d) illustration of electromagnetic fields in a CNT relevant for the z-pinch stiffening effect. Axial current (orange) is confined to the CNT walls and induces a circumferential magnetic field (blue). (e and f) The cross-section free-body diagram of the continuum CNT model for the z-pinch. Internal forces on both faces along the contour are shown in red. Pressure acting on CNT wall (e) and equivalent restoring force (f) are shown in blue, adopted with permission from ACS.[464]

displayed a 75–90% increase in specific electrical conductivity and 260–320% increase in specific tensile stress to failure, compared to the zero-field sample.

Linnik *et al.*[482] reported the RF (13.56 MHz) bias-enhanced nucleation of diamond on dielectric substrates where the nucleation densities obtained on sapphire and Si substrates were 10^{10} and 10^{11} cm^{-2}, respectively. In PECVD of carbon-based nanomaterials, internal EF associated with the plasma plays an important role in oriented growth.[183,186,483] However, additional electrical biasing has also been enforced, ensuring vertical growth and/or enhancing desired materials attributes.[188] For large-area deposition of high electrical conducting graphite-like carbon film in PECVD, high and uniform plasma density and effective ion bombardment (*i.e.*, high plasma energy) are needed to increase graphitic character. To this, Bae *et al.*[434] used a high negative substrate bias (up to 2 kV) to decouple the ion flux with ion energy, enhancing the ion bombardment energy (≥1.3 keV) of the Ar/C_6H_6 surface-wave plasma (plasma density ≥10^{17} m^{-3}) for the deposition of sp^2 carbon-rich films. With increasing bias, the deposition rate decreased, but the graphitic character increased, resulting in a highly conducting large area (16 cm) film. In PECVD, diffused/remote plasma configurations overcome the issues of defect creation and etching, which are observed in the direct plasma configuration. However, in vertical growth of carbon nanomaterials, diffused/remote plasma configurations may also lead to horizontal growth.[484–487] The application of an additional external substrate bias with respect to the electrically grounded chamber wall minimized the horizontal growth.[59,184,186] Butcher *et al.*[488] used a biased grid placed between the plasma and the substrate, shielding the substrate from the strong EFs generated by the RF plasma during PECVD of GaN. PECVD with a grounded grid resulted in highly smooth films, whereas +ve grid biasing led to columnar growth. Interestingly, −ve grid biasing significantly reduced the carbon and hydrocarbon content of GaN films. Similarly, by placing metal-covered Si half-rings around an Ir/YSZ/Si(001) substrate, Yoshikawa *et al.*[489] demonstrated wafer-scale bias-enhanced nucleation and heteroepitaxial growth of single-crystalline diamond by PECVD, with the half-rings and their thickness influencing the bias-enhanced nucleation density and the plasma density distribution. Some studies have reported innovative ways to execute the EF-matter interaction in CVD. For example, Reiprich *et al.*[490] reported an EF-guided localized and programmable CVD method to deposit 3D materials. The electrically charged precursor molecules were guided by the arrays of electrodynamic funnels to nanosized (≥250 nm) deposition locations, where nearest neighbor coupling led to the deposition of 3D nanostructures. Shi *et al.*[491] reported double bias induced post-deposition nanostructuring of a boron-doped diamond film *via* a reactive ion etching process, introduced by negative substrate bias (250–300 V) and positive bias (0–60 V) of a strategically placed grid in the HFCVD system. The double biasing greatly improved the etching efficiency, forming nanocone structures with enhanced electrochemically active surface area.

Some studies simulated the physical processes on the scale of the apparatus in EF-assisted PECVD to present mathematical models relating the electrical bias with the deposition rate.[492,493] For example, to explain the diamond growth from the CH_4/H_2 gas mixture in EFCVD, Lifang *et al.*[494,495] performed Monte Carlo simulation correlating the energy carried by electron and precursor fragments as a function of experimental parameters. For metal-catalyzed CVD of CNTs, Saeidi and coworkers[496,497] presented a theoretical model relating the external EF with the phonon oscillations of metal catalysts. They demonstrated that a catalyst-specific optimum electric field was required, depending upon the metal–carbon van der Waals interactions, atomic mass, and free charge carrier density of metal atoms.[497] Wang *et al.*[438] proposed a two-dimensional axisymmetric model to understand the influence of positive bias and deposition pressure on the plasma flow properties in the deposition chamber during the bias-enhanced PECVD process, predicting a bias voltage threshold phenomenon with a narrow range of suitable voltage.

4.3 Perspective on electric field-assisted chemical vapor deposition

The imposition of external EF around the assembly of precursors, carrier gas, and substrate has provided a non-contaminating way to manipulate the CVD process. However, except for bias-enhanced nucleation in diamond growth and aligned growth of nanostructures, the potentials of EF-assisted modulations seem to be underutilized in CVD. Previous studies have focused mainly on the realization of EF-assistance on isolated, lab-scale deposition processes, which should be tested at the industrial scale, given the importance of CVD in modern manufacturing. In this regard, recent reports of employing EF-assisted modulations in tuning the ion energies in plasma-assisted atomic layer deposition,[498,499] an offshoot technique of PECVD, warrant renewed attention in EFCVD.

Electric field-driven, potentially non-thermal mechanisms have proven their significance in materials synthesis and processing,[500] manifesting far-from-equilibrium effects at a range of length scales – from the atomic level to microstructural level – and therefore should not remain ignored in CVD. The reports of using an external electric field to influence defect creation and defect migration during materials processing[432,433,435,501,502] should be extended to the EFCVD of diverse functional materials.

Most reports on EFCVD remain confined to lab-scale demonstrations, primarily due to economic constraints and challenges of process integration. In addition, limited understanding of EF-matter interaction in CVD parametric space also poses a significant barrier to broader the adoption of EFCVD. As nucleation and film growth are mediated by charged nanoclusters generated in the gas phase during CVD,[466,473,503–505] there is a growing need for studies investigating the influence of external EF effects on electrostatic energy and drag force acting on these nanoparticles, particularly in relation to floating, grounded, or biased substrates. Such investigations accompanied by appropriate modeling efforts, specifically focusing on the influence of external EF on the reactivity, mass and heat transfer, and reaction kinetics would provide valuable insights to optimize EFCVD processes and scale them for practical applications.

5 Magnetic field-assisted chemical vapor process

5.1 Magnetic field-matter interaction in chemical vapor deposition

Depending upon the time-space properties of the field, an MF-matter interaction has manifested into any or a combination of phenomena – Zeeman effect, magneto-thermodynamic effect, magnetic torque, Lorentz force, Faraday force, eddy current, and energy injection.[506] Quantitatively, an external magnetic field of 1 T induces a $\sim$0.05 J mol^{-1} change in Gibbs free energy of a chemical reaction at room temperature, influencing the rate constant by a seemingly insignificant factor of $\sim 10^{-5}$.[507] However, these low-energy magnetic interactions have displayed a noticeable influence on chemical kinetics and the outcome of the chemical reactions.[508] For example, when a magnetic field is applied in the course of precursor flow in CVD, polar molecules and charged particles move in a cyclical way under the influence of the MF-induced Lorenz force, making their movement trajectories overlap more frequently. This increased the probability of collision between reacting species and carrier gas molecules.[26] An external MF influenced the nucleation process and, depending upon the difference in magnetization between the vapor phase and the substrate, provided an extra driving force in the form of Zeeman energy, thus lowering the energy barrier for nucleation on the substrate surface.[509] A sufficiently strong and favorably oriented MF influenced the mobility and diffusion of precursor molecules onto the substrate surface, altering the crystallization temperature, phase separation, and morphology in the resulting film.[510] The coupling of MF with other field effects-electric field,[27,28,31] plasma,[29,30,511] or both[26,27,31,512,513] has resulted in a synergistic effect, leading to the deposition of films with unique nanostructures.

5.2 Overview of magnetic field-assisted chemical vapor deposition

The initial reports on externally controlled MF assistance in the CVD process can be traced back to the 1980s when it was used to influence the plasma properties during PECVD, displaying variable effects of MF on the plasma and resulting deposition, depending upon the MF strength, precursor characteristics, and plasma and thermodynamic parameters.[514–516] For example, MF was used to confine the plasma density over the substrate, enhancing the deposition rate and film quality of DLC films.[517–519] The confinement of a low RF power plasma by an MF parallel to the substrate surface effectively enhanced the plasma density without increasing the ion energy, resulting in a high deposition rate at low DC self-bias (sheath voltage). In the absence of MF, only a high RF power input could ensure a high growth rate. However, a high RF power resulted in a high sheath voltage and ion energy, causing a potential deterioration in film quality. The external MF influenced the plasma sheath parameters by affecting the ion flux and ion energy.[516] A streamlined magnetic field has been used to stabilize the RF plasma over long-range propagation, enabling high plasma density with a decay-free, uniformly distributed ion energy over an extended space, thus offering an energy-efficient means for scalable fabrication of films of 1D/2D materials.[511,520–522] Table 4 presents selected examples of MF assistance employed in CVD of functional coatings.

Researchers also employed an external MF to influence the normal CVD processes for the deposition of numerous functional materials. For example, metal catalysts used for the growth of CNTs are influenced by the application of magnetic field, thus altering the growth mechanism. During MFCVD of Fe-encapsulated CNTs, Wei *et al.*[527] observed that an MF (0.2 T with a gradient of $\sim$50 mT cm^{-1}) transverse to the growth direction resulted in the growth of branched CNTs having Fe particles at their base, whereas an MF parallel to the growth direction led to less-branched Fe-encapsulated CNTs. Similarly, the CVD of carbon nanofibers over a Ni catalyst led to random nanofibers with entangled orientation, but an external MF assistance led to an aligned growth perpendicular to the substrate.[528] Interestingly, with increasing field strength (up to 0.5 T) the morphology changed from disordered solid-cored nanofibers to bamboo-like CNTs. A growth mechanism based on the particle size of the catalyst, which decreased with increasing magnetic field and the diamagnetic nature of carbon atoms, was proposed to explain the morphological variations in CNFs with the field strength. A similar growth mechanism, induced by an ordered arrangement of magnetic FeMgAl layered double hydroxide catalyst flakes in an MF-assisted fluidized bed CVD, resulted in a higher yield of bundles of longer, narrower, and highly graphitic CNTs.[521]

Magnetic field assistance has played a key role in enabling the growth of diamond at relatively low temperatures and low pressures in catalytic HFCVD.[537–539] Based on the atomic scale dynamics and electronic spin effects for carbon rehybridization and fixation, Little and Goddard[537] demonstrated the influence of a static MF on the nucleation and growth mechanism of diamond. A strong MF ($\sim$19.3 T) was capable of initiating the nucleation, thus eliminating the requirement of chemical or abraded nucleation centers.[537] The constriction effect induced by Lorentz force of the static MF increased the effective concentration of electrons and polarized hydrocarbon species in the reactive gas mixture by minimizing their collisions with the reactor walls.[539] In a periodic MF (with magnetic field strength $B = B_0 \sin \omega_f t$, where B_0 is maximum field strength and ω_f is angular frequency, Fig. 8(a)), the concentration of active carbon particles increased with increasing ω_f, resulting in enhanced nucleation density and diminished crystal size. Due to the rotation of magnetic lines in a periodic field, the electrons and polarized hydrocarbon species prolong their moving path, leading to a higher probability of collision with reaction gas molecules to produce more carbon precursors.[539] However, based on the intricate relationship between B_0 and vibrational frequency of spiral movement, it is proposed that the positive effect of increasing ω_f on prolonging the moving path of particles becomes negative beyond a ω_f value (Fig. 8(b)).[525,539]

Table 4 Selected reports on external MF assistance in CVD of functional materials[a]

Material/substrate	Process parameters (precursor, MF, substrate temperature)	Key features	Application	Ref.
Diamond/Si (111)	($H_2 + CH_4$; 98/2 sccm); dynamic magnetic field (DMF, $\omega = 83$–600 π rad s^{-1})	Enhanced nucleation density due to an induced EF excited by the DMF and electron-stimulated H desorption	—	523
Diamond/rod-shaped tungsten carbide	($H_2 + CH_4$; 2000/10 sccm); ring magnet 400 mT; 800 °C	Simulation studies on MF distribution, ion movement, and deposition	—	524
Diamond/Si (100)	($H_2 + CH_4$; 99/1 vol.); periodic MF ($\omega = 0$–1 kHz); ~700 °C	(110) or (100) orientation favored with lower or higher ω	—	525
Nanostructured carbon films/Si	($H_2 + CH_4$) ~8 mT; ~700 °C	MF assistance in PECVD resulted in finer nanostructures with higher crystallinity	Electron field emission; MFCVD sample gave turn-on field 6.5 V μm^{-1} (*vs.* ~15.5 for zero-field)	442
Diamond film/Si (100)	($H_2 + CH_4$); ~8 mT; −ve substrate bias (0–40 mA current); ~700 °C	Combined EF- and MF-assisted control; film thickness varied with field	Electron field emission; MFCVD sample gave turn-on field 6.1 V μm^{-1} (*vs.* 11.2 for zero-field)	31
Diamond film/Si	($H_2 + CH_4$); ~4 mT; ~808–872 °C	Use of a rotating MF; film thickness 7.41 μm (without MF 6.88 μm)	—	526
Branched or Fe-encapsulated carbon nanotubes/Si	Iron(II) phthalocyanine + H_2; ~0.2 T (gradient 50 mT cm^{-1}); 550 °C	MF promoted the coalescence or division of catalyst particles, forming branched or encapsulated CNTs	—	527
DLC on YG8 carbide substrate	Cathode arc discharge (120 A DC), (N_2, Ar, C_2H_2), 0.9 Pa, 450 °C	Role of MF and bias controlled on structure and properties	Cutting tool protection film; coefficient of friction = 0.112	91
Carbon nanofibers (CNFs)/Ni-deposited Cu	C_2H_2; 0–0.5 T; 700 °C	CNFs changed to homogenized, narrower, bamboo-like CNTs with increasing MF	—	528
Single-walled carbon nanotubes	10 T	MF-assisted preferential growth of metallic single-walled CNTs (1 nm diameter)	—	529
a-C:H:SiO_x film/stainless steel	(Polyphenylmethylsiloxane + Ar); (0–1.7 mT)	Use of MF for enhancing plasma confinement in PECVD; elastic modulus increased from 90 to 117–125 GPa	Tribological application; hardness increased from 8.7 to 11.7–12.5 GPa	29
Vertically standing graphene	(5–50 mT)	Use of MF for plasma confinement and vertical growth	Na^+ battery anode; capacity retention of 86% after 2000 cycles at 1 A g^{-1}	511
Carbon nanotubes on LDH-catalyst	($N_2/H_2/C_3H_6$ 70/40/40 ml min^{-1}); (~0.02 T); ~700 °C	MF affects catalyst arrangement, inducing higher yield, increased length and graphitic nature	—	521
Iron oxide/Si (100)	$[Fe(O^tBu)_3]_2$; 0–0.5 T perpendicular to the substrate; 500 °C	Magnetite with increased particulate size in MFCVD, whereas (hematite + amorphous iron(III)oxide) in CVD	—	530
Iron on FTO or Si (100)	$Fe(CO)_5$; 0–1 T; 300 °C	Anisotropic columnar growth in MFCVD, isotropic grain growth in CVD	Water-splitting; *J* values were 0.027 and 0.050 mA cm^{-2} for no field and MF film	531
α-Fe_2O_3/FTO	$Fe(CO)_5$ + 20 sccm O_2; 0–120 mT	MF assistance in PECVD	Water-splitting; *J* values were 0.484 and 0.659 mA cm^{-2} for no field and MF film	532
UO_2/Si	$U(O^tBu)_6$; 0–1 T; 400–1000 °C	Preferred ⟨111⟩ growth in CVD, polycrystalline growth in MFCVD	—	533

Table 4 (*Contd.*)

Material/substrate	Process parameters (precursor, MF, substrate temperature)	Key features	Application	Ref.
TiO_2/Si	$TiCl_2(O^iPr)(pyridine)_3$; 0–0.5 T with (perpendicular/parallel) field orientation; 300 °C	Well-defined anatase-type TiO_6 subunits in MFCVD, whereas rutile-type distorted TiO_6 units in CVD	—	534
$MgFe_2O_4$ films	$MgFe_2(O^tBu)_8$; 0–1 T; 300 °C	MF induces higher grain growth and densification, influencing the magnetic domains and inversion of the crystal lattice	—	535
ReN films/Si	[*fac*-Re(I)(CO)$_3$(L)]; 0–1 T; 600 °C	Preferred growth along the ⟨100⟩ direction in MFCVD	—	536

[a] a-C:H:SiO_x-SiO_x doped amorphous hydrogenated carbon; J = photocurrent density; L = (*N*,*N*-(4,4,4-trifluorobut-1-en-3-on)-dimethyl propylene diamine; LDHs – FeMgAl layered double hydroxides.

As diamond films are known for their orientation-dependent functional properties, Wang *et al.*[525] demonstrated that depending upon lower or higher ω_f values the MF-assisted HFCVD grown diamond film preferred a (110) or (100) orientation, respectively. Using a methane and hydrogen (1/99 vol%) gas mixture, the molar ratio of C_2H_2 and CH_3 fragments ($C_{[C_2H_2]}/C_{[CH_3]}$) in a reactive gas mixture influenced the orientation of the diamond film. The C–H bond dissociation energy in CH_3 (462 kJ mol^{-1}) is lower than that in C_2H_2 (556 kJ mol^{-1}), indicating an easier dehydrogenation of CH_3 than C_2H_2. The rising collision possibility with increasing ω_f raised the $C_{[C_2H_2]}$ more rapidly compared to the $C_{[CH_3]}$, resulting in a higher $C_{[C_2H_2]}/C_{[CH_3]}$ ratio that favored the (100) orientation over (110) orientation. Also, higher ω_f values resulted in continuous nanodiamond films with fine grains, displaying an improved field emission performance.[539]

In a related study, Wang *et al.*[31] investigated the effect of the coupled magnetic and electric field on the growth of a diamond film, presenting a qualitative simulation of the moving paths of particles in the coupled fields with different electric field intensities, direction of initial velocity, and charge-to-mass ratio (Fig. 8(c)). The experimental results indicated that the coupled fields enhanced the graphitization and refinement of diamond crystals. The simulation study pointed out that MF suppressed the (100) orientation by changing the precursor distribution, influencing the ratio of two precursor fragments $-C_2H_2$ and CH_3, a key factor deciding the preferred orientation of the as-prepared film.

Liu *et al.*[540] investigated the effect of a dynamic MF (where the induced EF points alternately in the ±*z* directions, orthogonal to the substrate surface[523]) with different angular frequencies on the growth rate, diamond quality, growth orientation, and deposition uniformity. At higher angular frequencies, the electrons move with a higher velocity and a larger radius, leading to an increased range of electron motion. With this, the electron-molecule collisional excitations are intensified, enabling more activated molecules to participate in growth and enhance the growth rate.[540] Additionally, similar to the EF-assisted bias-enhanced nucleation,[90,419,420] a dynamic MF drives electrons and ions to enhance the diamond nucleation. However, it does not cause a persistent bombardment of charged particles to the diamond growth front, which otherwise causes graphitization. Thus, a dynamic MF suppressed the sp^2 carbon generation and improved the diamond quality.[540] Presenting a detailed investigation of the effect of dynamic MF on diamond growth, Liu *et al.*[523] demonstrated that the dynamic MF-induced EF alternately pointed in the ±*z* directions, driving the electrons to continuously oscillate during motion and leading to non-persistent bombarding at the substrate surface.[523] As a result, the dynamic MF-induced diamond nucleation has an entirely different surface chemistry compared to the EF bias-assisted nucleation. As the thermal energy of the hot filament was well below the energy required to generate atomic H and CH_3 components *via* gas phase electron–molecule collisions, the gas phase electron–molecule collision excitation could not support the enhancement of diamond nucleation in CVD. The nucleation density (calculated from

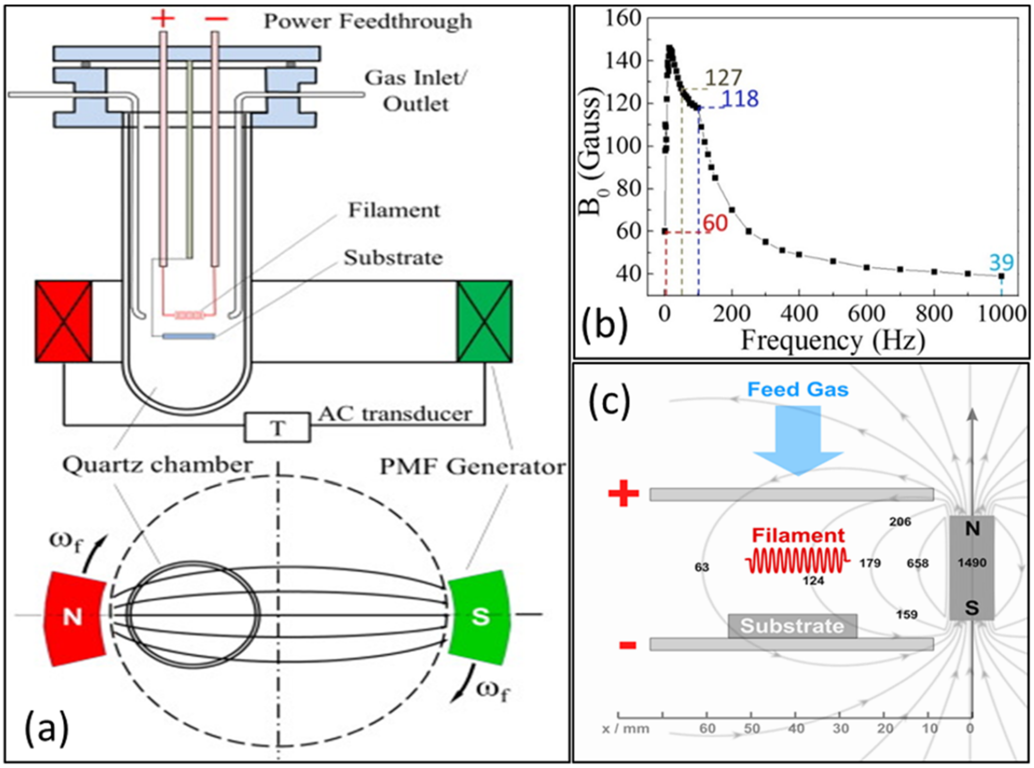

Fig. 8 (a) Schematic diagram of a periodic MF-assisted HFCVD system and (b) the measured relationship between B_0 and angular frequencies, reused with permission from Elsevier.[525] (c) A schematic displaying the distribution of MF strength in magnetic and electric field coupled HFCVD. The numerical values in figures are taken from the work of Wang *et al.*[31] and represent the Gaussian value of the MF strength.

SEM images) displayed a dependence on ω (Fig. 9(a)) and the Fourier-transformed infrared spectroscopy (FTIR) of the MF-assisted HFCVD film displayed strong peaks at 1750 and 2240–2400 cm^{-1} (Fig. 9(b)), indicating a highly activated film surface. Therefore, the authors proposed that dynamic MF mainly influenced the surface chemistry rather than the gas chemistry. The enhancement was attributed to a dynamic MF-induced EF, leading to the electron-stimulated desorption of hydrogen and formation of carbon dangling bonds on the growth front, which subsequently morphed into mono-radical and bi-radical sites for enhanced diamond nucleation (Fig. 9(c)).

Magnetic field-assisted CVD has been also employed for the deposition of numerous non-carbonaceous materials, such as metalloids and metal oxides. For example, in PECVD of hydrogenated microcrystalline silicon (μc-Si:H) thin films, Kim *et al.*[541] observed that an MF assist using a geometrically aligned magnetic mirror resulted in a 7-fold increase in deposition rate and enhanced crystallinity. This was attributed to the increased formation of Si and SiH radicals from the SiH_4 precursor under MF-induced enhanced plasma confinement, as observed in the analysis of plasma properties using optical emission spectroscopy.

For magnetically active materials, the application of MF during CVD influences not only the deposition and growth process but also the orientation of grains and other field effects.[542] Mathur and coworkers have extensively used MF-assisted manipulation in the CVD of magnetically active materials.[530–536,543] For example, PECVD of hematite film using an iron pentacarbonyl precursor displayed excellent MF-assisted control on phase and surface properties in static MF generated by different arrangements (parallel/perpendicular; par/perp) of rod-type or disk-type magnets (RTMs or DTMs) along the substrate (Fig. 10(a)–(f)).[532] In crystallographic analysis, the zero field and RTM-perp samples experienced preferred growth along the (110) crystallographic plane, whereas the RTM-par sample, along with the DTM-par and DTM-perp samples, experienced preferred growth along the (104) plane (Fig. 10(g) and (h)). Compared to zero field deposition, field-assisted depositions resulted in a more homogeneous particle shape and size, forming a denser microstructure (Fig. 10(i)–(n)). The films deposited under the DTM-perp arrangement creating an overall attractive field interaction exhibited larger aggregates with fewer grain boundaries (Fig. 10(j)). The films deposited under the DTM-par arrangement creating an overall repulsive interaction exhibited more aggregates of densified crystallites (Fig. 10(k)). However, the films deposited under DTM-perp and DTM-par arrangements displayed no difference in crystallite sizes. More importantly, the hematite film prepared under MF-assistance displayed significant enhancement in photoelectrochemical properties in water splitting, which was attributed to the presence of smooth particle surfaces and fewer grain boundaries in field-assisted growth, favoring charge transportation and reduced charge recombination.

The MFCVD of hematite on F-doped SnO_2 and Si(100) substrates displayed substrate-independent anisotropic growth

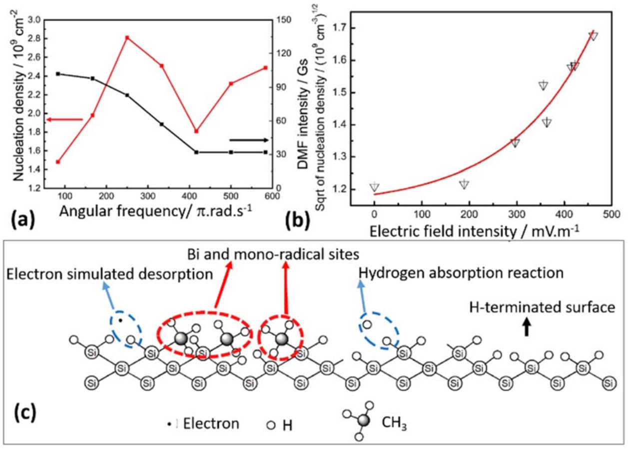

Fig. 9 (a) Dynamic MF intensity and diamond nucleation density as a function of angular frequencies; (b) square root of diamond nucleation density fitted (red curve) as a function of the induced electric field; and (c) schematic diagram of the diamond growth front and hydrogen desorption, adopted with permission from Elsevier.[523]

of α-Fe_2O_3 columns, as against an isotropic grain growth in zero field deposition.[533] Moreover, a parallel field resulted in larger crystallites with cuboidal morphology, whereas a 45° inclination led to a tilted orientation of anisotropic grains. The TEM analysis displayed a gradual increase in average crystallite size with increasing field strength, supporting the observation that even under low MF strength, the interactions between the crystalline nuclei and MF can greatly influence the nucleation and grain growth on the substrate.[31,530,536]

Mathur and coworkers further broadened the horizon of MFCVD by using a paramagnetic metalorganic Ti(III) precursor [$TiCl_2(O^iPr)(pyridine)_3$] for the deposition of TiO_2 films, demonstrating a remarkable shape anisotropy in deposited films.[534] The MF-assisted ($B = 0.5$ T) deposition resulted in the growth of well-defined anatase-type TiO_6 subunits, whereas zero-field deposition led to distorted rutile-type TiO_6 subunits. The zero-field deposition displayed preferential growth along the (200) plane, whereas the MFCVD resulted in preferential growth along the (101) and (200) planes in perpendicular-field

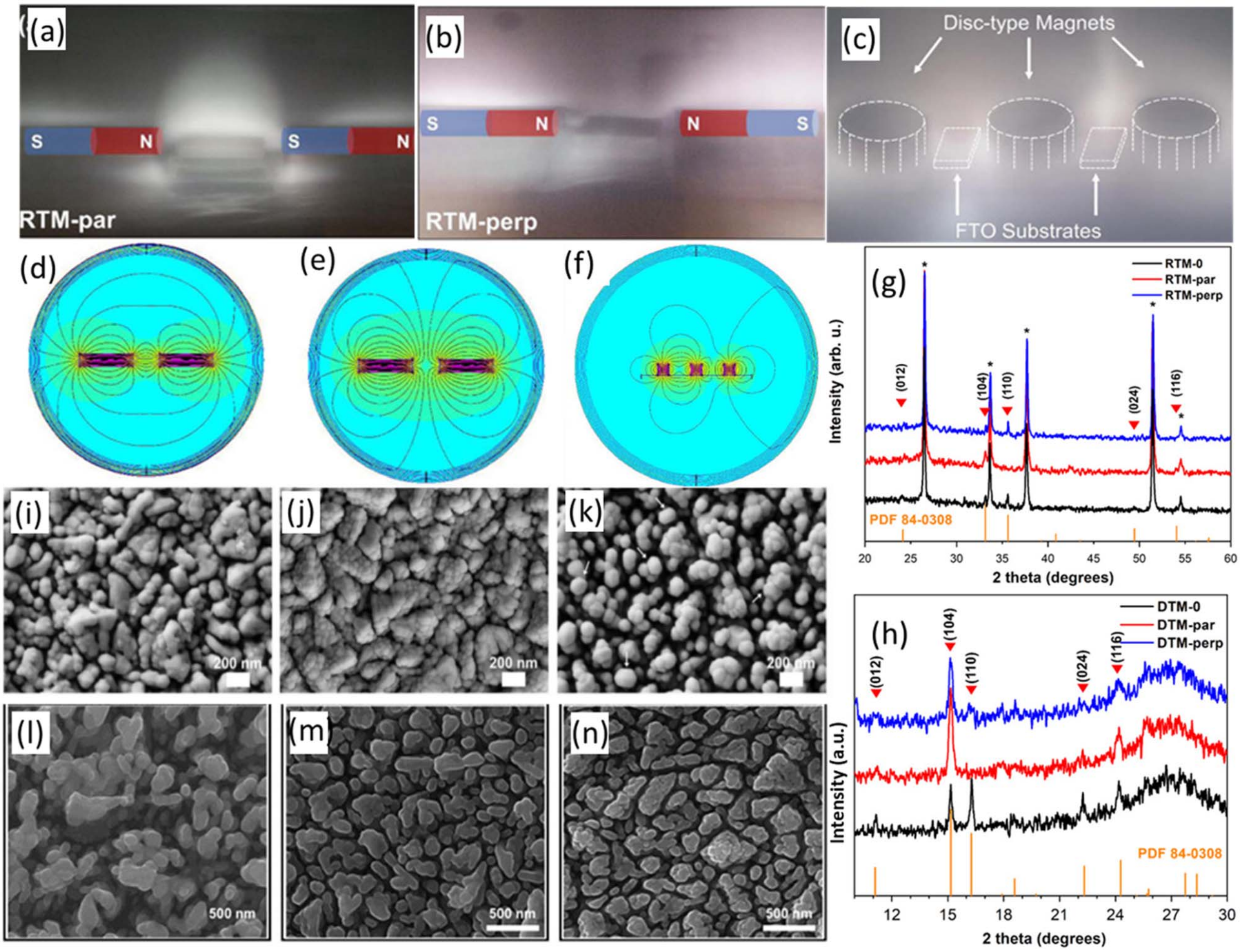

Fig. 10 Photographs of plasma under (a) parallel and (b) perpendicular field geometry and corresponding qualitative magnetic field profiles (d) and (e) for RTMs; photographs of plasma (c) and corresponding qualitative magnetic field profile (f) for arrangement of DTMs; XRD patterns of the hematite films deposited under different MFs. Asterisks (*) represent SnO_2 from FTO substrates (g) and (h); surface morphologies of deposition using RTM under (i) zero field, (j) parallel field, and (k) perpendicular field; surface morphologies of deposition using DTM under (l) zero field, (m) parallel field, and (n) perpendicular field, adopted with permission from Wiley.[532]

and parallel-field orientations, respectively. Elaborating on the MF-matter interaction, similar experiments performed using a diamagnetic precursor $Ti(O^iPr)_4$ indicated no such field-dependent microstructural variations, highlighting the importance of the d^1 electronic configuration in triggering the MF-matter interaction. However, noticeably, irrespective of the field strength and orientation, the MFCVD with paramagnetic precursors resulted in diamagnetic TiO_2 films.[534]

MFCVD displayed similar variations in shape, morphology, and crystallographic orientation during <1.0 T MF-assisted CVD of rhenium nitride,[536] UO_2,[531] and $MgFe_2O_4$.[535] Interestingly, although MF-assist has invariably increased the nucleation and growth and has a homogenization effect on shape, particle size distribution, and composition, it has exerted a varying influence on particle size evolution, depending upon the MF orientations and magnetic behavior of participating and resulting species. More precisely, except for UO_2 (ref. 531) and $YBa_2Cu_3O_7$ films,[509] the MF assistance led to increased particle size in CVD of magnetite,[530] hematite,[532] TiO_2,[534] rhenium nitride,[536] and $MgFe_2O_4$.[535] This was explained based on the induced internal magnetic field inside the growing diamagnetic UO_2 and $YBa_2Cu_3O_7$ being antiparallel to the applied external MF, creating an energetically unfavorable situation for grain growth.[509] Notwithstanding, in case of $YBa_2Cu_3O_7$ a low MF (≤2.0 T) caused a decrease in grain size compared to the zero field, but at higher MF (≥4.0 T) the grain size increased, due to the change in growth mode—from being 2D at low MF to 3D at higher MF,[509] and most likely due to, in our opinion, a high MF field overcoming the internal diamagnetic field effect.

5.3 Perspective on magnetic field-assisted CVD

Over the years, numerous results have strengthened the utility of external MF in inducing a profound influence on the nucleation, grain growth, phase composition, and crystallographic orientation during CVD, thus altering the morphology, chemical topography, and functional properties of the resulting films. Therefore, it is expected to increasingly become a preferred pathway, compared to conventional experimental controls-temperature and pressure or precursor chemistry, for *in situ* manipulation of the material properties of the CVD-grown films. Magnetic fields with spatial and temporal variations such as periodic, dynamic, or rotating configurations have shown significant potential in influencing nucleation and growth mechanisms during CVD. However, such approaches have mostly been limited to the deposition of diamond materials and their application to other material systems remains underexplored. Most reports on magnetic field-assisted CVD are limited to lab-scale set-ups with small-area deposition. A key challenge lies in generating strong and uniform magnetic fields over larger deposition areas. This limitation is reflected in the fact that most MFCVD studies have employed magnetic field strengths of ≤1 T. New CVD setup designs capable of accommodating even stronger magnetic fields (≥5 T) carry the potential to broaden the scope of MFCVD enabling field-assisted control over growth kinetics and materials properties. Nevertheless, the integration of strong magnets brings added instrumentation complexity, cost, and technical expertise requirements, which must be carefully considered for practical scalability.

Most MF-matter interaction studies in CVD so far have focused mainly on the precursor-MF interactions, and the interaction of MF with a carrier gas and substrate[533,544,545] is less explored. Moreover, the interaction of MF with temperature, an important process control parameter, has been less precisely monitored and understood, especially in the case of a magnetically active precursor and deposited materials. The influence of external MF in those CVD processes where paramagnetic oxygen is used as a reactant/carrier gas[546] is less exploited. Most importantly, the field of MFCVD lacks sufficient mathematical models and simulation studies relating the effects of external magnetic fields with the CVD growth parameters.

6 Concluding remarks

Field-assisted chemical vapor deposition (CVD) represents a promising future direction for controlling thin-film growth, with precise control over film properties and microstructure. This technique involves applying external fields, such as magnetic or electric fields, during the CVD process to influence the deposition dynamics, leading to novel material characteristics and improved process efficiency. The various field-assisted modulations in CVD have emerged as a powerful additional control method, often operating independently of precursor chemistry influence and thermodynamic parameters. These modulations have enabled significant advancements in growth control, microstructure tuning, and material properties for targeted applications.

This review underscores the importance of non-conventional process parameters in CVD and highlights their impact on material synthesis. Additionally, it addresses key limitations, particularly the lack of theoretical studies that could provide deeper insights into the role of these modulators in CVD nucleation and growth. Understanding their effects on microstructure, composition, and functional properties remains a crucial challenge. In particular, the emerging field of magnetic-field-assisted CVD would benefit from further research, enabling reliable control over the process and material characteristics.

According to current estimates, the global CVD market has reached approximately 24 billion USD and is projected to grow to nearly 48 billion USD by 2032.[547] Field-assisted manipulations are expected to play a key role in capitalizing on this trend; however, the existing challenges, as schematically highlighted in Fig. 11, need to be effectively addressed to unfold the potential of field-enhanced CVD techniques. Key advancements will likely involve optimizing field modulations in terms of intensity and configuration and innovations in reactor design to accommodate such modulations in high-throughput systems. Additionally, advancing our understanding of field-matter interactions, coupled with extensive computational analysis using 3D reactor-scale models, will be crucial for overcoming current limitations. Finally, the integration of *operando* and *in situ* techniques into conventional CVD systems and processes to

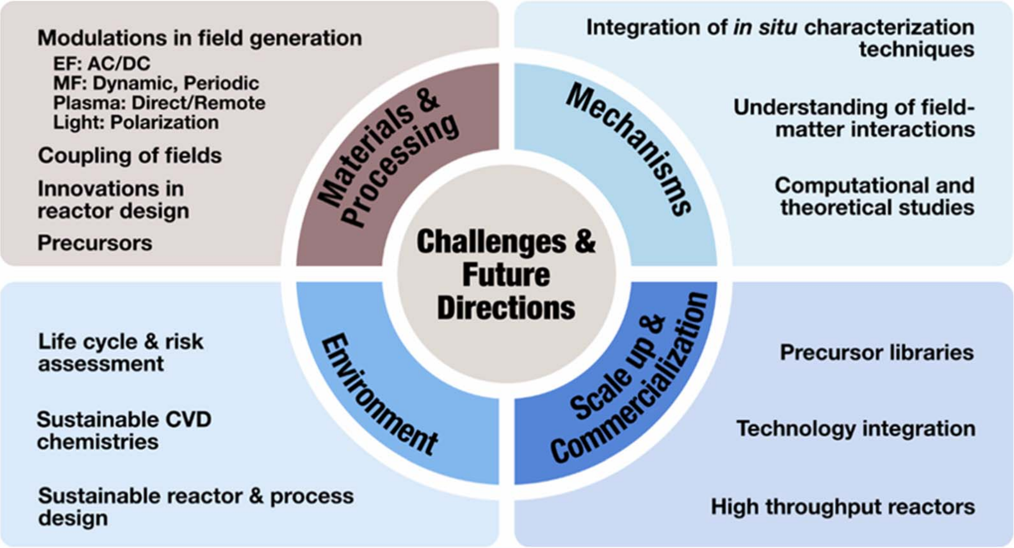

Fig. 11 Schematic of existing challenges in field-assisted CVD and the future directions to overcome them.

develop a robust framework for depositing materials with enhanced functional properties can bring a paradigm shift in thin film engineering.

Data availability

No primary research results, software or code have been included and no new data were generated or analysed as part of this review.

Author contributions

All authors contributed equally.

Conflicts of interest

There are no conflicts of interest to declare.

Acknowledgements

Authors gratefully thank the University of Cologne for the infrastructural and financial support. SM acknowledges the financial support by the German Science Foundation (DFG) in the frame of the priority program SPP 1959 “Manipulation of matter controlled by electric and magnetic field: towards novel synthesis and processing routes of inorganic materials”.

Notes and references

1 B. Sun, J. Pang, Q. Cheng, S. Zhang, Y. Li, C. Zhang, D. Sun, B. Ibarlucea, Y. Li, D. Chen, H. Fan, Q. Han, M. Chao, H. Liu, J. Wang, G. Cuniberti, L. Han and W. Zhou, *Adv. Mater. Technol.*, 2021, **6**, 2000744.

2 L. Sun, G. Yuan, L. Gao, J. Yang, M. Chhowalla, M. H. Gharahcheshmeh, K. K. Gleason, Y. S. Choi, B. H. Hong and Z. Liu, *Nat. Rev. Methods Primers*, 2021, **1**, 1–20.

3 M. Nakaya, A. Uedono and A. Hotta, *Coatings*, 2015, **5**, 987–1001.

4 M. Bahri, S. H. Gebre, M. A. Elaguech, F. T. Dajan, M. G. Sendeku, C. Tlili and D. Wang, *Coord. Chem. Rev.*, 2023, **475**, 214910.

5 L. Wang, G. Sun and S. Yuan, *Adv. Mater. Technol.*, 2024, **9**, 2301973.

6 J. Zhang, J. Wang, G. Zhang, Z. Huo, Z. Huang and L. Wu, *Mater. Des.*, 2024, **237**, 112577.

7 M. Yaseen, M. A. K. Khattak, A. Khan, S. Bibi, M. Bououdina, M. Usman, N. A. Khan, A. A. A. Pirzado, R. A. Abumousa and M. Humayun, *Nanocomposites*, 2024, **10**, 1–40.

8 L. Tang, J. Tan, H. Nong, B. Liu and H.-M. Cheng, *Acc. Mater. Res.*, 2021, **2**, 36–47.

9 M. D. Straub, J. Leduc, M. Frank, A. Raauf, T. D. Lohrey, S. G. Minasian, S. Mathur and J. Arnold, *Angew. Chem., Int. Ed.*, 2019, **58**, 5749–5753.

10 U. Atamtürk, E. Jung, T. Fischer and S. Mathur, *Chem. Mater.*, 2022, **34**, 7344–7356.

11 C. K. Amadi, T. Karimpour, M. Jafari, Z. Peng, D. V. Gerven, V. Brune, F. Hartl, M. Siaj and S. Mathur, *Dalton Trans.*, 2024, **53**, 9874–9886.

12 A. Sutorius, R. Weißing, C. R. Pèrez, T. Fischer, F. Hartl, N. Basu, H. Suk Shin and S. Mathur, *Nanoscale*, 2024, **16**, 15782–15792.

13 V. Brune, C. Hegemann and S. Mathur, *Inorg. Chem.*, 2019, **58**, 9922–9934.

14 B. Qin, H. Ma, M. Hossain, M. Zhong, Q. Xia, B. Li and X. Duan, *Chem. Mater.*, 2020, **32**, 10321–10347.

15 Y. Hamedani, P. Macha, T. J. Bunning, R. R. Naik, M. C. Vasudev, Y. Hamedani, P. Macha, T. J. Bunning, R. R. Naik and M. C. Vasudev, in Chemical Vapor

Deposition – Recent Advances and Applications in Optical, *Solar Cells and Solid State Devices*, IntechOpen, 2016.
16 F. Loyer, S. Bulou, P. Choquet and N. D. Boscher, *Plasma Processes Polym.*, 2018, **15**, 1800121.
17 G. Franz, *Processes*, 2021, **9**, 980.
18 H. Kun, J. Li, K. Li, N. Yan, C. bian, Y. Guan, Y. Yang and H. Li, *Polym. Degrad. Stab.*, 2022, **196**, 109816.
19 R. Panickar, C. B. Sobhan and S. Chakravorti, *Vacuum*, 2020, **172**, 109108.
20 M. Bi, J. Zhu, Y. Luo, H. Cai, X. Li, X. Wang, Y. Wei, X. Wang, C. Hu, J. Hu, G. Zhang, X. Wang and X. Zhang, *Coatings*, 2022, **12**, 1731.
21 K. Alberi and M. A. Scarpulla, *J. Phys. D: Appl. Phys.*, 2017, **51**, 023001.
22 X. Zhao, C. Wei, Z. Gai, S. Yu and X. Ren, *Chem. Pap.*, 2020, **74**, 767–778.
23 M. E. A. Warwick, A. J. Roberts, R. C. T. Slade and R. Binions, *J. Mater. Chem. A*, 2014, **2**, 6115–6120.
24 A. Sawabe and T. Inuzuka, *Appl. Phys. Lett.*, 1985, **46**, 146–147.
25 S. Yugo, T. Kimura and T. Muto, *Vacuum*, 1990, **41**, 1364–1367.
26 J. Li, Y. Wang, Q. Wei, Y. Xie, H. Long, Z. Deng, L. Ma, Z. Yu, Y. Jiang, N. Hu and K. Zhou, *Surf. Coat. Technol.*, 2017, **324**, 413–418.
27 Y. Wang, Q. Wei, Z. Yu, H. Long, Z. Deng, Y. Xie, J. Li, C.-T. Lin, L. Ma and K. Zhou, *Appl. Surf. Sci.*, 2017, **423**, 788–792.
28 W. In-Hwang, X. Chen, T. Kuzuya, K. Kawabe and S. Motojima, *Carbon*, 2000, **38**, 565–571.
29 A. S. Grenadyorov, A. A. Solovyev, K. V. Oskomov and V. O. Oskirko, *J. Vac. Sci. Technol., A*, 2019, **37**, 061512.
30 T. Tabuchi, M. Takashiri and K. Ishida, *Surf. Coat. Technol.*, 2007, **202**, 114–120.
31 Y. Wang, J. Li, N. Hu, Y. Jiang, Q. Wei, Z. Yu, H. Long, H. Zhu, Y. Xie, L. Ma, C.-T. Lin and W. Su, *Mater. Res. Express*, 2018, **5**, 035009.
32 X. Lu, P. J. Bruggeman, S. Reuter, G. Naidis, A. Bogaerts, M. Laroussi, M. Keidar, E. Robert, J.-M. Pouvesle, D. Liu and K. Ostrikov, *Front. Phys.*, 2022, **10**, 1–12.
33 *Plasma Chemistry*, ed. A. Fridman, Cambridge University Press, Cambridge, 2008, pp. 12–91.
34 I. B. Denysenko, S. V. Ivko and N. A. Azarenkov, in *2018 IEEE 8th International Conference Nanomaterials: Application & Properties (NAP)*, 2018, pp. 1–5.
35 L. Martinu, O. Zabeida and J. E. Klemberg-Sapieha, in *Handbook of Deposition Technologies for Films and Coatings*, ed. P. M. Martin, William Andrew Publishing, 3rd edn, Boston, 2010, pp. 392–465.
36 S. Sovizi, S. Angizi, S. A. Ahmad Alem, R. Goodarzi, M. R. R. Taji Boyuk, H. Ghanbari, R. Szoszkiewicz, A. Simchi and P. Kruse, *Chem. Rev.*, 2023, **123**, 13869–13951.
37 C. Vallée, M. Bonvalot, S. Belahcen, T. Yeghoyan, M. Jaffal, R. Vallat, A. Chaker, G. Lefèvre, S. David, A. Bsiesy, N. Possémé, R. Gassilloud and A. Granier, *J. Vac. Sci. Technol., A*, 2020, **38**, 033007.
38 J. Chen, Z. Bo and G. Lu, in *Vertically-Oriented Graphene: PECVD Synthesis and Applications*, ed. J. Chen, Z. Bo and G. Lu, Springer International Publishing, Cham, 2015, pp. 19–34.
39 J. Zhou, J. Liao, J. Huang, T. Chen, B. Lv and Y. Peng, *Vacuum*, 2022, **195**, 110678.
40 M. Yamamoto, H. Murata, N. Miyata, H. Takashima, M. Nagao, H. Mimura, Y. Neo and K. Murakami, *ACS Omega*, 2023, **8**, 5497–5505.
41 J. Chen, P. Ji, Y. Yang, C. Jin, L. Zhuge and X. Wu, *Diamond Relat. Mater.*, 2021, **112**, 108243.
42 J. Chen, P. Ji, Y. Yang, C. Jin, L. Zhuge and X. Wu, *Thin Solid Films*, 2020, **709**, 138167.
43 J. Wang, P. Bulkin, I. Florea, J.-L. Maurice and E. Johnson, *J. Phys. D: Appl. Phys.*, 2016, **49**, 285203.
44 S. Lin, D. Xie, Y. Tang, Y. Wang, F. Jing, N. Huang and Y. Leng, *Vacuum*, 2021, **189**, 110223.
45 P. Mandracci and P. Rivolo, *Coatings*, 2023, **13**, 1075.
46 N. M. Santhosh, G. Filipič, E. Tatarova, O. Baranov, H. Kondo, M. Sekine, M. Hori, K. Ken Ostrikov and U. Cvelbar, *Micromachines*, 2018, **9**, 565.
47 K. Ollegott, P. Wirth, C. Oberste-Beulmann, P. Awakowicz and M. Muhler, *Chem. Ing. Tech.*, 2020, **92**, 1542–1558.
48 R. Snyders, D. Hegemann, D. Thiry, O. Zabeida, J. Klemberg-Sapieha and L. Martinu, *Plasma Sources Sci. Technol.*, 2023, **32**, 074001.
49 Y. Hua, J. Song, Z. Hao, G. Zhang and C. Ren, *Plasma Res. Express*, 2018, **1**, 015008.
50 K. Yi, D. Liu, X. Chen, J. Yang, D. Wei, Y. Liu and D. Wei, *Acc. Chem. Res.*, 2021, **54**, 1011–1022.
51 V. Cech and M. Branecky, *Plasma Processes Polym.*, 2023, **20**, 2300019.
52 G. S. Oehrlein and S. Hamaguchi, *Plasma Sources Sci. Technol.*, 2018, **27**, 023001.
53 D. W. Hess, *Annu. Rev. Mater. Sci.*, 1986, **16**, 163–183.
54 S. Mathur and T. Ruegamer, *Int. J. Appl. Ceram. Technol.*, 2011, **8**, 1050–1058.
55 L. Czympiel, M. Frank, A. Mettenbörger, S.-M. Hühne and S. Mathur, *C. R. Chim.*, 2018, **21**, 943–951.
56 A. S. M. de Freitas, C. C. Maciel, J. S. Rodrigues, R. P. Ribeiro, A. O. Delgado-Silva and E. C. Rangel, *Vacuum*, 2021, **194**, 110556.
57 M. Li, D. Liu, D. Wei, X. Song, D. Wei and A. T. S. Wee, *Adv. Sci.*, 2016, **3**, 1600003.
58 N.-C. Yeh, C.-C. Hsu, J. Bagley and W.-S. Tseng, *Nanotechnology*, 2019, **30**, 162001.
59 E. Bertran-Serra, S. Rodriguez-Miguel, Z. Li, Y. Ma, G. Farid, S. Chaitoglou, R. Amade, R. Ospina and J.-L. Andújar, *Nanomaterials*, 2023, **13**, 2533.
60 G. L. Kabongo, B. M. Mothudi and M. S. Dhlamini, *Front. Mater.*, 2021, **8**, 1–11.
61 H. Nagasawa and T. Tsuru, in *Advanced Materials for Membrane Fabrication and Modification*, CRC Press, 2018.
62 D. Patrun, S. Zhao, Z. Aytuna, T. Fischer, M. Miess, Z. Hong and S. Mathur, *Nano Energy*, 2024, **128**, 109836.

63 M. Pyeon, T.-P. Ruoko, J. Leduc, Y. Gönüllü, M. Deo, N. V. Tkachenko and S. Mathur, *J. Mater. Res.*, 2018, **33**, 455–466.

64 L. Jürgensen, M. Frank, M. Pyeon, L. Czympiel and S. Mathur, *Organometallics*, 2017, **36**, 2331–2337.

65 R. Garg, N. Rajagopalan, M. Pyeon, Y. Gönüllü, T. Fischer, A. S. Khanna and S. Mathur, *Surf. Coat. Technol.*, 2018, **356**, 49–55.

66 L. Jürgensen, D. Höll, M. Frank, T. Ludwig, D. Graf, A. Katrin Schmidt-Verma, A. Raauf, I. Gessner and S. Mathur, *Dalton Trans.*, 2020, **49**, 13317–13325.

67 F. Zhou, J. Shan, L. Cui, Y. Qi, J. Hu, Y. Zhang and Z. Liu, *Adv. Funct. Mater.*, 2022, **32**, 2202026.

68 F. Sanchette, M. El Garah, S. Achache, F. Schuster, C. Chouquet, C. Ducros and A. Billard, *Coatings*, 2021, **11**, 1225.

69 J. Li and H. Chae, *Korean J. Chem. Eng.*, 2023, **40**, 1268–1276.

70 Y. Liu, J. He, N. Zhang, W. Zhang, Y. Zhou and K. Huang, *J. Mater. Sci.*, 2021, **56**, 12559–12583.

71 S. V. Baryshev and M. Muehle, *IEEE Trans. Plasma Sci.*, 2024, **52**, 1082–1103.

72 N. Chen, D. H. Kim, P. Kovacik, H. Sojoudi, M. Wang and K. K. Gleason, *Annu. Rev. Chem. Biomol. Eng.*, 2016, **7**, 373–393.

73 Z. Yang, Y. Liu, Z. Guo, J. Wei, J. Liu, L. Chen and C. Li, *Diamond Relat. Mater.*, 2024, **142**, 110767.

74 C.-W. Chuang and F. C.-N. Hong, *Cryst. Growth Des.*, 2023, **23**, 37–48.

75 F. Movassagh-Alanagh, A. Abdollah-Zadeh, M. A. Zolbin, N. Nemati and R. Aghababaei, *Tribol. Int.*, 2023, **179**, 108137.

76 O.-G. Simionescu, O. Brîncoveanu, C. Romaniţan, S. Vulpe and A. Avram, *Coatings*, 2022, **12**, 943.

77 G. Moradkhani, J. Profili, M. Robert, G. Laroche, S. Elkoun and F. Mighri, *Polymers*, 2024, **16**, 360.

78 A. D. Nguyen, T. K. Nguyen, C. T. Le, S. Kim, F. Ullah, Y. Lee, S. Lee, K. Kim, D. Lee, S. Park, J.-S. Bae, J. I. Jang and Y. S. Kim, *ACS Omega*, 2019, **4**, 21509–21515.

79 J. Zheng, A. Xu, A. Wu and X. Li, *ACS Appl. Mater. Interfaces*, 2021, **13**, 21231–21240.

80 S. P. Flynn, M. McKenna, R. Monaghan, S. M. Kelleher, S. Daniels and A. MacCormac, *J. Chem. Educ.*, 2017, **94**, 221–225.

81 Y. Huang, L. Cao and P. Zeng, *Russ. J. Phys. Chem.*, 2023, **97**, 3399–3404.

82 M. Zhao, D. Chen, Y. Guo, Q. Wang, T. Zhao, J. Lu and Y. Zhou, *Thin Solid Films*, 2023, **784**, 140064.

83 J.-H. Oh, T. K. Lee, R. Y. Kim, J.-H. An, S.-I. Mo, J.-E. Hong, S.-W. Kim, M. J. Keum, H. Song and K.-H. Kim, *Small Struct.*, 2024, **5**, 2300218.

84 J. Cho, H. Seok, I. Lee, J. Lee, E. Kim, D. Sung, I.-K. Baek, C.-H. Lee and T. Kim, *Sci. Rep.*, 2022, **12**, 10335.

85 L. Himics, D. Gál, P. Csíkvári, R. Holomb, M. Koós, A. Sulyok, B. Pécz and M. Veres, *Vacuum*, 2023, **216**, 112493.

86 V. A. Terekhov, E. I. Terukov, Y. K. Undalov, K. A. Barkov, N. A. Kurilo, S. A. Ivkov, D. N. Nesterov, P. V. Seredin, D. L. Goloshchapov, D. A. Minakov, E. V. Popova, A. N. Lukin and I. N. Trapeznikova, *Symmetry*, 2023, **15**, 1800.

87 C. Wu, D. Y. Guo, L. Y. Zhang, P. G. Li, F. B. Zhang, C. K. Tan, S. L. Wang, A. P. Liu, F. M. Wu and W. H. Tang, *Appl. Phys. Lett.*, 2020, **116**, 072102.

88 V. K. Shukla, J. Lekshmi, B. S. Yadav, M. Kumari, S. Dalal, A. Goyal and P. Rai, *Int. J. Refract. Met. Hard Mater.*, 2024, **119**, 106559.

89 H.-U. Kim, H. Seok, W. S. Kang and T. Kim, *Nanoscale Adv.*, 2022, **4**, 2962–2972.

90 V. S. Jayaseelan and R. N. Singh, *J. Mater. Res.*, 2024, **39**, 825–835.

91 H. Tian, S. Jie, P. Zhang, J. Li and S. An, *Diamond Relat. Mater.*, 2024, **141**, 110671.

92 A. M. Mumlyakov, E. A. Pershina, Ju. V. Bondareva, P. A. Nekludova, A. A. Shibalova, M. V. Shibalov, Yu. V. Anufriev, A. M. Tagachenkov and M. A. Tarkhov, *Carbon*, 2023, **214**, 118332.

93 Y. Ma, J. Han, D. Yue, Z. Tong, M. Wang, L. Xiao, S. Jia and X. Chen, *Inorg. Chem.*, 2023, **62**, 13505–13511.

94 R. Muñoz, E. López-Elvira, C. Munuera, F. Carrascoso, Y. Xie, O. Çakıroğlu, T. Pucher, S. Puebla, A. Castellanos-Gomez and M. García-Hernández, *npj 2D Mater. Appl.*, 2023, **7**, 1–11.

95 T.-T. Zhang, B.-H. Lv, C.-C. Fan, B.-Y. Shi, Q.-J. Cao, W. Wang, F.-F. Tao and W.-D. Dou, *ACS Omega*, 2023, **8**, 36245–36252.

96 W. J. Lee, T.-Y. Cho, J.-H. Eom, J.-S. Park, J. Ryu and S.-K. Cho, *Plasma Processes Polym.*, 2022, **19**, 2200001.

97 A. M. Wrobel and P. Uznanski, *Plasma Processes Polym.*, 2023, **20**, 2200190.

98 G. Akiki, D. Suchet, D. Daineka, S. Filonovich, P. Bulkin and E. V. Johnson, *Appl. Surf. Sci.*, 2020, **531**, 147305.

99 B. Jugdersuren, X. Liu, J. C. Culbertson, N. Mahadik, O. Thomas and Y. Shu, *J. Appl. Phys.*, 2023, **134**, 214303.

100 C. Yu, K. Gao, C.-W. Peng, C. He, S. Wang, W. Shi, V. Allen, J. Zhang, D. Wang, G. Tian, Y. Zhang, W. Jia, Y. Song, Y. Hu, J. Colwell, C. Xing, Q. Ma, H. Wu, L. Guo, G. Dong, H. Jiang, H. Wu, X. Wang, D. Xu, K. Li, J. Peng, W. Liu, D. Chen, A. Lennon, X. Cao, S. De Wolf, J. Zhou, X. Yang and X. Zhang, *Nat. Energy*, 2023, **8**, 1375–1385.

101 D. Liu, X. Chen, Y. Yan, Z. Zhang, Z. Jin, K. Yi, C. Zhang, Y. Zheng, Y. Wang, J. Yang, X. Xu, J. Chen, Y. Lu, D. Wei, A. T. S. Wee and D. Wei, *Nat. Commun.*, 2019, **10**, 1188.

102 K. Chakrabarty, I. Arnold and S. A. Catledge, *J. Vac. Sci. Technol., A*, 2019, **37**, 061507.

103 K. Yi, Z. Jin, S. Bu, D. Wang, D. Liu, Y. Huang, Y. Dong, Q. Yuan, Y. Liu, A. T. S. Wee and D. Wei, *ACS Appl. Mater. Interfaces*, 2020, **12**, 33113–33120.

104 B. Schurink, W. T. E. van den Beld, R. M. Tiggelaar, R. W. E. van de Kruijs and F. Bijkerk, *Coatings*, 2022, **12**, 685.

105 H. Nadhom, D. Lundin, P. Rouf and H. Pedersen, *J. Vac. Sci. Technol., A*, 2020, **38**, 033402.

106 D. E. Gomersall and A. J. Flewitt, *J. Appl. Phys.*, 2022, **131**, 215301.

107 P. M. Campbell, C. J. Perini, J. Chiu, A. Gupta, H. S. Ray, H. Chen, K. Wenzel, E. Snyder, B. K. Wagner, J. Ready and E. M. Vogel, *2D Mater.*, 2017, **5**, 015005.
108 H. He, C. Wu, H. Hu, S. Wang, F. Zhang, D. Guo and F. Wu, *J. Phys. Chem. Lett.*, 2023, **14**, 6444–6450.
109 C. A. Beaudette, J. T. Held, K. A. Mkhoyan and U. R. Kortshagen, *ACS Omega*, 2020, **5**, 21853–21861.
110 K. M. M. D. K. Kimbulapitiya, B. Rehman, S. S. Wani, C.-T. Chen, R.-H. Cyu, A. Manikandan, M. K. Date, Y.-R. Peng, R. J. G. L. R. Kumara, F.-C. Chuang and Y.-L. Chueh, *Nano Energy*, 2024, **122**, 109235.
111 E. Z. Frątczak, J. Balcerzak and M. Rogala, *Materials*, 2024, **17**, 314.
112 Y. Xia, Z. Xu, J. Peng, Q. Shen and C. Wang, *Surf. Coat. Technol.*, 2022, **441**, 128522.
113 M. A. Kudryashov, L. A. Mochalov, I. O. Prokhorov, M. A. Vshivtsev, Y. P. Kudryashova, V. M. Malyshev and E. A. Slapovskaya, *High Energy Chem.*, 2023, **57**, 532–536.
114 T.-H. Yang, Z.-Z. Lin, S.-C. Tsai, J.-Z. Dai, S.-M. Chen, M.-W. Lin and S. Chen, *Mater. Sci. Semicond. Process.*, 2023, **162**, 107515.
115 C. Yadav, M. Kumar, K. Lodhi and S. Kumar, *Mater. Today Commun.*, 2023, **36**, 106736.
116 M. Gürsoy, *Coatings*, 2024, **14**, 347.
117 O. Richard, H. Mziouek, R. Arès, V. Aimez and A. Jaouad, *Surf. Interfaces*, 2023, **40**, 103104.
118 K. D. Lee, K.-S. Ji, S. Bae, S. Kim, H. Kim, J. E. Kim, Y. C. Nam, S. Choi, M. S. Jeong, M. G. Kang, H.-E. Song, Y. Kang, H.-S. Lee and D. Kim, *J. Nanosci. Nanotechnol.*, 2017, **17**, 4687–4693.
119 S. Ahn, S. J. Hong, H. S. Yang and S. M. Cho, *Mater. Sci. Semicond. Process.*, 2022, **143**, 106538.
120 H.-L. Chen, Y.-C. Tu, C.-C. Hsieh, D.-L. Lin and K.-C. Leou, *J. Appl. Phys.*, 2014, **116**, 103307.
121 B. B. Sahu and J. G. Han, *Phys. Plasmas*, 2016, **23**, 123504.
122 G. Das, S. Mandal, S. Dhar, S. Bose, J. R. Sharma, S. Mukhopadhyay, C. Banerjee and A. K. Barua, *J. Mater. Sci.: Mater. Electron.*, 2017, **28**, 10382–10390.
123 X. Li, R. Jin, L. Li, J. Lu, Y. Gu, F. Ren and J. Huang, *Optik*, 2019, **180**, 104–112.
124 M. A. Yusuf, A. Rosikhin, J. D. Malago, F. A. Noor and T. Winata, *Mater. Sci. Forum*, 2019, **966**, 100–106.
125 S. Juneja and S. Kumar, *Silicon*, 2021, **13**, 3927–3940.
126 X. Zhou, X. Tan, Y. Lv, Y. Wang, J. Li, S. Liang, Z.-H. Zhang, Z. Feng and S. Cai, *Opt. Express*, 2020, **28**, 29245–29252.
127 P. R. Y. Gangavarapu, A. M. R. Sharma and A. K. Naik, *Semicond. Sci. Technol.*, 2019, **34**, 065018.
128 B. B. Sahu, Y. Yin and J. G. Han, *Phys. Plasmas*, 2016, **23**, 033512.
129 C. Chen, W. Fu, C. Zhang, D. Lu, M. Han and Y. Yan, *Appl. Sci.*, 2021, **11**, 9873.
130 M. Cantoro, S. Hofmann, C. Mattevi, S. Pisana, A. Parvez, A. Fasoli, C. Ducati, V. Scardaci, A. C. Ferrari and J. Robertson, *J. Appl. Phys.*, 2009, **105**, 064304.
131 T. Labbaye, E. Kovacevic, T. Lecas, M.-R. Ammar, A. Canizarès, N. Raimboux, T. Strunskus, C. Jaeger, P. Simon and C. Boulmer-Leborgne, *Appl. Surf. Sci.*, 2018, **453**, 436–441.
132 U. Sharma and S. C. Sharma, *IEEE Trans. Plasma Sci.*, 2022, **50**, 888–898.
133 U. Khalilov, A. Bogaerts, S. Hussain, E. Kovacevic, P. Brault, C. Boulmer-Leborgne and E. C. Neyts, *J. Phys. D: Appl. Phys.*, 2017, **50**, 184001.
134 Z. Jiang, B. Zhang, Q. Shen and Z.-J. Jiang, *J. Alloys Compd.*, 2019, **806**, 864–873.
135 W. Wang, É. Ngo, P. Bulkin, Z. Zhang, M. Foldyna, P. Roca i Cabarrocas, E. V. Johnson and J.-L. Maurice, *Nanomaterials*, 2023, **13**, 2061.
136 S. Djoumi, F. Kail, P. R. i Cabarrocas and L. Chahed, *Thin Solid Films*, 2022, **758**, 139447.
137 J. Tang, J.-L. Maurice, W. Chen, S. Misra, M. Foldyna, E. V. Johnson and P. Roca i Cabarrocas, *Nanoscale Res. Lett.*, 2016, **11**, 455.
138 M. Hývl, M. Müller, T.-H. Stuchlíková, J. Stuchlík, M. Šilhavík, J. Kočka, A. Fejfar and J. Červenka, *Nanotechnology*, 2020, **31**, 225601.
139 A. O. Zamchiy, E. A. Baranov, S. Ya. Khmel, E. A. Maximovskiy, D. V. Gulyaev and K. S. Zhuravlev, *Thin Solid Films*, 2018, **654**, 61–68.
140 E. Azrak, W. Chen, S. Moldovan, S. Gao, S. Duguay, P. Pareige and P. Roca i Cabarrocas, *J. Phys. Chem. C*, 2018, **122**, 26236–26242.
141 L. Zheng, E. Azrak, R. Gong, C. Castro, S. Duguay, P. Pareige, P. Roca i Cabarrocas and W. Chen, *J. Alloys Compd.*, 2022, **899**, 163273.
142 L. Dai, I. Maurin, M. Foldyna, J. Alvarez, W. Wang, H. Mohsin, W. Chen, J.-P. Kleider, J.-L. Maurice, T. Gacoin and P. R. i Cabarrocas, *Nanotechnology*, 2018, **29**, 435301.
143 W. Yang, X. Zhang, F. Huang, Z. Zhang, J. Muhammad, X. Li, Z. Rong, X. Guo, Y. Jung and X. Dong, *Appl. Surf. Sci.*, 2021, **557**, 149848.
144 E. Azrak, Z. Xue, S. Liu, W. Chen, C. Castro, S. Duguay, P. Pareige, L. Yu and P. Roca i Cabarrocas, *Appl. Surf. Sci.*, 2023, **618**, 156637.
145 J. W. Miller, Z. Khatami, J. Wojcik, J. D. B. Bradley and P. Mascher, *Surf. Coat. Technol.*, 2018, **336**, 99–105.
146 F. Azmi, Y. Gao, Z. Khatami and P. Mascher, *J. Vac. Sci. Technol., A*, 2022, **40**, 043402.
147 Z. Khatami, L. Wolz, J. Wojcik and P. Mascher, *J. Mater. Res.*, 2024, **39**, 150–164.
148 F. Azmi, Y. Gao, Z. Khatami and P. Mascher, *Meet. Abstr.*, 2020, MA2020-01, p. 2934.
149 R. B. Namin, P. Mascher, F. Chibante and Z. Khatami, *ECS J. Solid State Sci. Technol.*, 2023, **12**, 106002.
150 J. Kulczyk-Malecka, D. Donaghy, B. Delfour-Peyrethon, M. Werner, P. R. Chalker, J. W. Bradley and P. J. Kelly, *J. Vac. Sci. Technol., A*, 2020, **38**, 033410.
151 N. R. Lee, Y. S. Jun, K. I. Moon and C. S. Lee, *Jpn. J. Appl. Phys.*, 2017, **56**, 035506.
152 K. H. Kim, K. S. Kim, Y. J. Ji, J. E. Kang and G. Y. Yeom, *Appl. Surf. Sci.*, 2021, **541**, 148313.

153 Z. Huang, Z. Chen, W. Lang and X. Wang, *Materials*, 2021, **14**, 2954.

154 R. Song, S. Chen, Z. Liu, C. Huo and Q. Chen, *Diamond Relat. Mater.*, 2023, **132**, 109687.

155 S.-C. Lin, C.-C. Wang, C.-L. Tien, F.-C. Tung, H.-F. Wang and S.-H. Lai, *Micromachines*, 2023, **14**, 279.

156 N. Q. Minh, N. Van Nong, M. S. D. C. Dela Vega, O. Oda and M. Hori, *Vacuum*, 2023, **213**, 112118.

157 A. Dias, N. Bundaleska, E. Felizardo, D. Tsyganov, A. Almeida, A. M. Ferraria, A. M. Botelho do Rego, M. Abrashev, T. Strunskus, N. M. Santhosh, U. Cvelbar, J. Zavašnik, M. F. Montemor, M. M. Almeida, P. A. Carvalho, J. Kissovski, L. L. Alves and E. Tatarova, *Chem. Eng. J.*, 2022, **430**, 133153.

158 M. Su, H. Yang, Z. Liu, E. Wu, X. Chen, Z. Bo, L. Dai and K. Ken Ostrikov, *Carbon*, 2022, **197**, 301–310.

159 B. Dey, S. Bulou, W. Ravisy, N. Gautier, M. Richard-Plouet, A. Granier and P. Choquet, *Surf. Coat. Technol.*, 2022, **436**, 128256.

160 C. T. Tran, M. Raco, L. M. Casey and D. R. McKenzie, *Plasma Processes Polym.*, 2022, **19**, 2200019.

161 A. Capote, G. Capote, E. J. Corat and V. J. Trava-Airoldi, *Surf. Coat. Technol.*, 2022, **445**, 128716.

162 K. Yamasaki, T. Matsutani, N. Imaeda and T. Kawasaki, *Vacuum*, 2015, **122**, 332–336.

163 M. Murano, T. Matsutani and T. Kawasaki, *Vacuum*, 2018, **158**, 60–64.

164 D. Batryshev, A. Utegenov, R. Zhumadilov, N. Akhanova, S. Orazbayev, S. Ussenkhan, J. Lin, K. Takahashi, N. Bastykova, S. Kodanova, M. Gabdullin and T. Ramazanov, *Contrib. Plasma Phys.*, 2022, **62**, e202100238.

165 Z. Guo, L. Sang, Z. Wang, Q. Chen, L. Yang and Z. Liu, *Surf. Coat. Technol.*, 2016, **307**, 1059–1064.

166 Y. Hu, X. Tian, Q. Fan, Z. Wang, B. Liu, L. Yang and Z. Liu, *Plasma Sci. Technol.*, 2019, **21**, 105502.

167 S. Bulou, E. Lecoq, F. Loyer, G. Frache, T. Fouquet, M. Gueye, T. Belmonte and P. Choquet, *Plasma Processes Polym.*, 2019, **16**, 1800177.

168 C. Ruhmlieb, Y. J. Lee, C. Strelow, T. Kipp and A. Mews, *J. Mater. Chem. C*, 2019, **7**, 10098–10110.

169 M. Taplick, C. Ruhmlieb, T. Kipp and A. Mews, *Nano Lett.*, 2023, **23**, 1313–1319.

170 M. A. A. Mamun, H. Furuta and A. Hatta, *Jpn. J. Appl. Phys.*, 2018, **57**, 06JF02.

171 R. Hatada, S. Flege, M. N. Ashraf, A. Timmermann, C. Schmid and W. Ensinger, *Coatings*, 2020, **10**, 360.

172 R. Hatada, K. Baba, S. Flege and W. Ensinger, *Surf. Coat. Technol.*, 2016, **305**, 93–98.

173 S. de F. M. Mariano, M. Ueda, R. M. Oliveira, E. J. de D. M. Pillaca and N. M. dos Santos, *Surf. Coat. Technol.*, 2017, **312**, 47–54.

174 S. F. M. Mariano and M. Ueda, *Appl. Surf. Sci.*, 2019, **465**, 824–832.

175 Z. Wu, E. Wang, G. Zhang, Y. Shen and G. Shao, *Small*, 2024, **11**, 2307923.

176 H. Wang, Y. Han, P. Luo, Y. Zhou, Q. Chen, H. Zhu, Y. Yang, B. Zhang and K. Huang, *ChemistrySelect*, 2022, **7**, e202200103.

177 S. Sahoo, G. Sahoo, S. M. Jeong and C. S. Rout, *J. Energy Storage*, 2022, **53**, 105212.

178 M. A. Zafar and M. V. Jacob, *Rev. Mod. Plasma Phys.*, 2022, **6**, 37.

179 S. Zheng, Q. Wang, K. Guo, J. Bai, Z. Yang, H. Yu, H. Liu, H. Wei, J. Zhu and Q. Hu, *J. Cryst. Growth*, 2024, **627**, 127538.

180 O. Baranov, I. Levchenko, S. Xu, J. W. M. Lim, U. Cvelbar and K. Bazaka, *2D Mater.*, 2018, **5**, 044002.

181 W. Zheng, X. Zhao and W. Fu, *ACS Appl. Mater. Interfaces*, 2021, **13**, 9561–9579.

182 A. Khan, J. Cong, R. R. Kumar, S. Ahmed, D. Yang and X. Yu, *ACS Appl. Nano Mater.*, 2022, **5**, 17544–17555.

183 S. Ghosh, S. R. Polaki, M. Kamruddin, S. M. Jeong and K. Ken Ostrikov, *J. Phys. D: Appl. Phys.*, 2018, **51**, 145303.

184 M. R. Maschmann, P. B. Amama, A. Goyal, Z. Iqbal and T. S. Fisher, *Carbon*, 2006, **44**, 2758–2763.

185 A. Thapa, S. Neupane, R. Guo, K. L. Jungjohann, D. Pete and W. Li, *Diamond Relat. Mater.*, 2018, **90**, 144–153.

186 J. Sun, T. Rattanasawatesun, P. Tang, Z. Bi, S. Pandit, L. Lam, C. Wasén, M. Erlandsson, M. Bokarewa, J. Dong, F. Ding, F. Xiong and I. Mijakovic, *ACS Appl. Mater. Interfaces*, 2022, **14**, 7152–7160.

187 A. Tewari, S. Ghosh and P. Srivastava, *Plasma Res. Express*, 2021, **3**, 035003.

188 S. Xu, S. Wang, Z. Chen, Y. Sun, Z. Gao, H. Zhang and J. Zhang, *Adv. Funct. Mater.*, 2020, **30**, 2003302.

189 C. Shen, S. Xu, Z. Chen, N. Ji, J. Yang and J. Zhang, *Small*, 2023, **19**, 2207745.

190 S. Xu, T. Cheng, Q. Yan, C. Shen, Y. Yu, C.-T. Lin, F. Ding and J. Zhang, *Adv. Sci.*, 2022, **9**, 2200737.

191 S. Xu, Y. Wen, Z. Chen, N. Ji, Z. Zou, M. Wu, L. Qu and J. Zhang, *Angew. Chem., Int. Ed.*, 2021, **60**, 24505–24509.

192 S.-F. Wang, D. Xue, J. Liang, L.-Y. Chen, Y. Xie and J.-M. Zhang, *Diamond Relat. Mater.*, 2023, **140**, 110426.

193 D. H. Seo, S. Yick, Z. J. Han, J. H. Fang and K. Ken Ostrikov, *ChemSusChem*, 2014, **7**, 2317–2324.

194 L.-A. Gautier, V. Le Borgne and M. A. El Khakani, *Carbon*, 2016, **98**, 259–266.

195 W.-H. Chiang, T.-C. Lin, Y.-S. Li, Y.-J. Yang and Z. Pei, *RSC Adv.*, 2016, **6**, 2270–2278.

196 X. Peng, Z. Wang, Z. Wang, J. Gong and H. Hao, *Catal. Today*, 2019, **337**, 63–68.

197 E. P. Neustroev, A. R. Prokopyev, S. O. Semenov, V. I. Popov, F. F. Protopopov, A. S. Andreev, N. A. Savvinova and E. S. Lukin, *IOP Conf. Ser.:Mater. Sci. Eng.*, 2021, **1079**, 042086.

198 A. Dias, E. Felizardo, N. Bundaleska, M. Abrashev, J. Kissovski, A. M. Ferraria, A. M. Rego, T. Strunskus, P. A. Carvalho, A. Almeida, J. Zavašnik, E. Kovacevic, J. Berndt, N. Bundaleski, M.-R. Ammar, O. M. N. D. Teodoro, U. Cvelbar, L. L. Alves, B. Gonçalves and E. Tatarova, *Appl. Mater. Today*, 2024, **36**, 102056.

199 J. Zheng, R. Yang, Y. Lou, W. Li and X. Li, *Thin Solid Films*, 2012, **521**, 137–140.

200 H. Seok, Y. T. Megra, C. K. Kanade, J. Cho, V. K. Kanade, M. Kim, I. Lee, P. J. Yoo, H.-U. Kim, J. W. Suk and T. Kim, *ACS Nano*, 2021, **15**, 707–718.

201 Y. Kim, S. Kwon, E.-J. Seo, J. H. Nam, H. Y. Jang, S.-H. Kwon, J.-D. Kwon, D.-W. Kim and B. Cho, *ACS Appl. Mater. Interfaces*, 2018, **10**, 36136–36143.

202 R. K. Joshi, M. Yoshimura, K. Tanaka, K. Ueda, A. Kumar and N. Ramgir, *J. Phys. Chem. C*, 2008, **112**, 13901–13904.

203 S. A. Ahmad Kamal, R. Ritikos and S. Abdul Rahman, *Appl. Surf. Sci.*, 2015, **328**, 146–153.

204 H. Hamidinezhad, A. Akbar Ashkarran and Z. Abdul-Malek, *Mater. Sci. Semicond. Process.*, 2014, **27**, 26–32.

205 M. Macias-Montero, A. Borras, Z. Saghi, J. P. Espinos, A. Barranco, J. Cotrino and A. R. Gonzalez-Elipe, *Nanotechnology*, 2012, **23**, 255303.

206 N. Filippin, J. Castillo-Seoane, M. C. López-Santos, C. T. Rojas, K. Ostrikov, A. Barranco, J. R. Sánchez-Valencia and A. Borrás, *ACS Appl. Mater. Interfaces*, 2020, **12**, 50721–50733.

207 M. C. Vasudev, H. Koerner, K. M. Singh, B. P. Partlow, D. L. Kaplan, E. Gazit, T. J. Bunning and R. R. Naik, *Biomacromolecules*, 2014, **15**, 533–540.

208 Z. He, C. S. Lee, J.-L. Maurice, D. Pribat, P. Haghi-Ashtiani and C. S. Cojocaru, *Carbon*, 2011, **49**, 4710–4718.

209 J. Jiang, N. M. Chetuya, E. I. Meletis, J. H. Ngai, G. J. Grzybowski and B. Claflin, *J. Vac. Sci. Technol. B*, 2024, **42**, 034001.

210 H.-U. Kim, M. Kim, H. Seok, K.-Y. Park, J.-Y. Moon, J. Park, B.-S. An, H. J. Jung, V. P. Dravid, D. Whang, J.-H. Lee and T. Kim, *ChemSusChem*, 2021, **14**, 1344–1350.

211 Y. Xing, S. Dong, X. Zhang, Y. Zhang, J. Han, X. Zhang, L. Zhang, B. Zhang and Z. Zeng, *Cryst. Growth Des.*, 2023, **23**, 2257–2263.

212 V. Brune, M. Grosch, R. Weißing, F. Hartl, M. Frank, S. Mishra and S. Mathur, *Dalton Trans.*, 2021, **50**, 12365–12385.

213 P. A. L. Sino, T.-C. Lin, S. Wani, L. Lee, C.-T. Chen, M.-J. Liu, Y.-Z. Kuo, B. Rehman, K. Tuyen Le, J.-M. Wu, F.-C. Chuang and Y.-L. Chueh, *Mater. Today*, 2023, **69**, 97–106.

214 M. Chaudhary, T.-Y. Yang, C.-T. Chen, P.-C. Lai, Y.-C. Hsu, Y.-R. Peng, A. Kumar, C.-H. Lee and Y.-L. Chueh, *Adv. Funct. Mater.*, 2023, **33**, 2303697.

215 J. Park, I. Cho, H. Jeon, Y. Lee, J. Zhang, D. Lee, M. K. Cho, D. J. Preston, B. Shong, I. S. Kim and W.-K. Lee, *Adv. Mater.*, 2024, **36**, 2314031.

216 H.-U. Kim, V. Kanade, M. Kim, K. S. Kim, B.-S. An, H. Seok, H. Yoo, L. E. Chaney, S.-I. Kim, C.-W. Yang, G. Y. Yeom, D. Whang, J.-H. Lee and T. Kim, *Small*, 2020, **16**, 1905000.

217 R. Zhang, Q. Zhang, X. Jia, S. Wen, H. Wu, Y. Gong, Y. Yin, C. Lan and C. Li, *Nanotechnology*, 2023, **34**, 345704.

218 K. Aydin, C. Kanade, V. Kaluram Kanade, G. Bahit, C. Ahn and T. Kim, *Nanoscale*, 2023, **15**, 17326–17334.

219 C. Ahn, J. Lee, H.-U. Kim, H. Bark, M. Jeon, G. H. Ryu, Z. Lee, G. Y. Yeom, K. Kim, J. Jung, Y. Kim, C. Lee and T. Kim, *Adv. Mater.*, 2015, **27**, 5223–5229.

220 H. Seok, M. Kim, J. Cho, E. Kim, S. Son, K.-W. Kim, J. K. Kim, P. J. Yoo, M. Kim, H.-U. Kim and T. Kim, *ACS Sustainable Chem. Eng.*, 2023, **11**, 568–577.

221 J. H. Kim, S. J. Yun, H. S. Lee, J. Zhao, H. Bouzid and Y. H. Lee, *Sci. Rep.*, 2018, **8**, 10284.

222 Y. Li, J. Duan, Y. Berencén, R. Hübner, H.-S. Tsai, C.-N. Kuo, C. Shan Lue, M. Helm, S. Zhou and S. Prucnal, *Nanoscale Adv.*, 2023, **5**, 443–449.

223 J. Cho, H. Seok and T. Kim, *Meet. Abstr.*, 2023, MA2023-02, p. 1157.

224 M. Chaudhary, Y.-C. Shih, S.-Y. Tang, T.-Y. Yang, T.-W. Kuo, C.-C. Chung, Y.-C. Shen, A. kumar Anbalagan, C.-H. Lee, T.-H. Hou, J.-H. He and Y.-L. Chueh, *ACS Appl. Mater. Interfaces*, 2023, **15**, 33858–33867.

225 W. Fan, H. Shen, B. Liu, L. Zhao, X. Zhang and H. Pan, *Energies*, 2023, **16**, 6963.

226 B. Grübel, H. Nagel, B. Steinhauser, F. Feldmann, S. Kluska and M. Hermle, *Phys. Status Solidi A*, 2021, **218**, 2100156.

227 J.-S. Song, Y. S. Park and N.-H. Kim, *Appl. Sci.*, 2021, **11**, 358.

228 Z. Zhong, X. Luo, L. Zhou, S. Hu, L. Dai, S. Wang and S. Yang, *Opt. Quantum Electron.*, 2023, **55**, 264.

229 Y.-R. Zhang, Y.-T. Hu and Y.-N. Wang, *Plasma Sources Sci. Technol.*, 2020, **29**, 084003.

230 H. J. Kim, K. Lee and H. Park, *Plasma Sources Sci. Technol.*, 2024, **33**, 015008.

231 H. J. Kim, K. Lee and H. Park, *Plasma Sources Sci. Technol.*, 2023, **32**, 115008.

232 D. Li, X. Feng, Z. Wen, Z. Shang and Y. She, *Optoelectron. Lett.*, 2016, **12**, 285–289.

233 H. Lim, Y. Park, N. Baek, S.-Y. Jun, S. Lee, J. Yang, D. Jung and S. Yu, *J. Nanosci. Nanotechnol.*, 2021, **21**, 4477–4483.

234 E. Bertran-Serra, A. Musheghyan-Avetisyan, S. Chaitoglou, R. Amade-Rovira, I. Alshaikh, F. Pantoja-Suárez, J.-L. Andújar-Bella, T. Jawhari, A. Perez-del-Pino and E. Gyorgy, *Appl. Surf. Sci.*, 2023, **610**, 155530.

235 G. Sato, T. Kato, W. Oohara and R. Hatakeyama, *Thin Solid Films*, 2006, **506–507**, 550–554.

236 C. R. Yang, C. H. Yeh, L. C. Hu, T. C. Wei, C. C. Lee, J. Y. Chang and T. T. Li, *Plasma Chem. Plasma Process.*, 2018, **38**, 247–259.

237 J. Miller, A. Ceballos, L. B. Bayu Aji, A. Moore, C. Wasz, S. O. Kucheyev, S. Elhadj and S. Falabella, *Thin Solid Films*, 2020, **714**, 138394.

238 L. C. Hu, G. M. Ruan, T. C. Wei, C. J. Wang, Y. W. Lin, C. C. Lee, Y. Kawai and T. T. Li, *Thin Solid Films*, 2014, **570**, 574–579.

239 P. Ji, J. Chen, T. Huang, L. Zhuge and X. Wu, *Diamond Relat. Mater.*, 2020, **109**, 108067.

240 Y. Xia, X. Yang, L. Chang, H. Zhou, J.-H. Zhang, D. Jing, Q. Xu, G.-J. Niu, H.-S. Zhou and G.-N. Luo, *Rev. Sci. Instrum.*, 2023, **94**, 125110.

241 Y. Yang, T. Huang, M. Li, Y. Yu, J. Huang, B. Yu, X. Wu and P. Ji, *Plasma Sci. Technol.*, 2022, **24**, 105502.

242 J. Chen, P. Ji, M. Li, T. Huang, L. Zhuge and X. Wu, *Plasma Sci. Technol.*, 2022, **24**, 054001.

243 P. Ji, J. Chen, T. Huang, C. Jin, L. Zhuge and X. Wu, *Diamond Relat. Mater.*, 2020, **108**, 107958.

244 P. Ji, J. Chen, T. Huang, C. Jin, L. Zhuge and X. Wu, *Appl. Phys. A*, 2020, **126**, 247.
245 X. Ma, D. Xu, P. Ji, C. Jin, J. Lin, Y. Ding and C. Xu, *Vacuum*, 2019, **164**, 355–360.
246 D. Li, S. Dai, A. Goullet and A. Granier, *Nano*, 2018, **13**, 1850124.
247 P. Ji, J. Yu, T. Huang, C. Jin, Y. Yang, L. Zhuge and X. Wu, *Plasma Sci. Technol.*, 2018, **20**, 025505.
248 J. Chen, P. Ji, C. JIN, L. Zhuge and X. Wu, *Plasma Sci. Technol.*, 2018, **21**, 025502.
249 J. Qian, P. Ji, C. Jin, L. Zhuge and X. Wu, *IEEE Trans. Plasma Sci.*, 2020, **48**, 2431–2436.
250 T. Goto, K.-I. Sato, Y. Yabuta, S. Sugawa and S. Hara, *IEEE J. Electron Devices Soc.*, 2018, **6**, 512–517.
251 H. Bae, I. Hamaguchi, K. Sasai, H. Suzuki and H. Toyoda, *Jpn. J. Appl. Phys.*, 2021, **60**, 126002.
252 S. Patil, S. Sharma, S. Sengupta, A. Sen and I. Kaganovich, *Phys. Rev. Res.*, 2022, **4**, 013059.
253 M. Magarotto, D. Melazzi and D. Pavarin, *J. Plasma Phys.*, 2019, **85**, 905850404.
254 Q.-Z. Zhang, J.-Y. Sun, W.-Q. Lu, J. Schulze, Y.-Q. Guo and Y.-N. Wang, *Phys. Rev. E*, 2021, **104**, 045209.
255 S. Sharma, I. D. Kaganovich, A. V. Khrabrov, P. Kaw and A. Sen, *Phys. Plasmas*, 2018, **25**, 080704.
256 T. Zhang, R. Cui, R. Han, F. He, W. Zhu, Z. Xia, Y. Cui and J. Ouyang, *Plasma Sources Sci. Technol.*, 2022, **31**, 105008.
257 A. O. Zamchiy, E. A. Baranov and S. Y. Khmel, *Vacuum*, 2018, **147**, 99–106.
258 A. O. Zamchiy, E. A. Baranov, I. E. Merkulova, V. A. Volodin, M. R. Sharafutdinov and S. Y. Khmel, *Vacuum*, 2018, **152**, 319–326.
259 E. A. Baranov, A. O. Zamchiy, N. A. Lunev, I. E. Merkulova, V. A. Volodin, M. R. Sharafutdinov and A. A. Shapovalova, *J. Appl. Mech. Tech. Phys.*, 2022, **63**, 757–764.
260 I. E. Merkulova, *J. Phys.: Conf. Ser.*, 2019, **1382**, 012160.
261 T. Tabuchi, Y. Toyoshima, S. Fujimoto and M. Takashiri, *Thin Solid Films*, 2020, **694**, 137714.
262 T. Tabuchi, Y. Toyoshima, S. Fujimoto and M. Takashiri, *AIP Adv.*, 2019, **9**, 055125.
263 H. Sugiura, H. Kondo, T. Tsutsumi, K. Ishikawa and M. Hori, *C*, 2019, **5**, 8.
264 L. Jia, H. Sugiura, H. Kondo, K. Takeda, K. Ishikawa, O. Oda, M. Sekine, M. Hiramatsu and M. Hori, *Plasma Processes Polym.*, 2016, **13**, 730–736.
265 H. Sugiura, L. Jia, Y. Ohashi, H. Kondo, K. Ishikawa, T. Tsutsumi, T. Hayashi, K. Takeda, M. Sekine and M. Hori, *Jpn. J. Appl. Phys.*, 2019, **58**, 030912.
266 T. Ichikawa, N. Shimizu, K. Ishikawa, M. Hiramatsu and M. Hori, *Carbon*, 2020, **161**, 403–412.
267 X.-F. Wang, W.-Z. Jia, Y.-H. Song, Y.-Y. Zhang, Z.-L. Dai and Y.-N. Wang, *Phys. Plasmas*, 2017, **24**, 113503.
268 D. Lundin, J. Jensen and H. Pedersen, *J. Vac. Sci. Technol., A*, 2014, **32**, 030602.
269 M. A. A. Mamun, H. Furuta and A. Hatta, *IEEE Trans. Plasma Sci.*, 2019, **47**, 22–31.
270 H. Kakiuchi, H. Ohmi and K. Yasutake, *J. Phys. D: Appl. Phys.*, 2020, **53**, 415201.
271 Z. Gong, J. Shi, W. Ma, B. Zhang and J. Zhang, *RSC Adv.*, 2016, **6**, 115092–115100.
272 Ö. Çelikel and H. Kavak, *Diamond Relat. Mater.*, 2021, **120**, 108610.
273 M. Y. Yoon, J.-R. Jeong, H.-C. Lee and J.-H. Kim, *Appl. Surf. Sci.*, 2023, **636**, 157814.
274 G. Kalita and M. Umeno, *AppliedChem*, 2022, **2**, 160–184.
275 A. M. Coclite and K. K. Gleason, *Plasma Processes Polym.*, 2012, **9**, 425–434.
276 M. Gürsoy, *Plasma Chem. Plasma Process.*, 2020, **40**, 1063–1079.
277 M. Gürsoy, *J. Appl. Polym. Sci.*, 2021, **138**, 49722.
278 F. Loyer, G. Bengasi, G. Frache, P. Choquet and N. D. Boscher, *Plasma Processes Polym.*, 2018, **15**, 1800027.
279 D. D. Burkey, in *CVD Polymers*, John Wiley & Sons, Ltd, 2015, pp. 65–85.
280 M. Wang, N. D. Boscher, K. Heinze and K. K. Gleason, *Adv. Funct. Mater.*, 2017, **27**, 1606652.
281 A. Kumar, D. S. Grant, K. Bazaka and M. V. Jacob, *J. Appl. Polym. Sci.*, 2018, **135**, 45771.
282 H. Akther, M. M. Rahman, A. H. Bhuiyan, H. Kabir, S. A.-A. Zumahi, J. A. Syed and R. Nasrin, *Mater. Today Commun.*, 2022, **31**, 103377.
283 A. Loesch-Zhang, A. Geissler and M. Biesalski, *Plasma Processes Polym.*, 2023, **20**, e2300016.
284 T. Dufour, *Polymers*, 2023, **15**, 3607.
285 S. Matsui, in *Encyclopedia of Nanotechnology*, ed. B. Bhushan, Springer Netherlands, Dordrecht, 2012, pp. 866–876.
286 W. J. MoberlyChan, D. P. Adams, M. J. Aziz, G. Hobler and T. Schenkel, *MRS Bull.*, 2007, **32**, 424–432.
287 M. Manoccio, M. Esposito, A. Passaseo, M. Cuscunà and V. Tasco, *Micromachines*, 2021, **12**, 6.
288 R. Winkler, J. D. Fowlkes, P. D. Rack and H. Plank, *J. Appl. Phys.*, 2019, **125**, 210901.
289 K. Höflich, G. Hobler, F. I. Allen, T. Wirtz, G. Rius, L. McElwee-White, A. V. Krasheninnikov, M. Schmidt, I. Utke, N. Klingner, M. Osenberg, R. Córdoba, F. Djurabekova, I. Manke, P. Moll, M. Manoccio, J. M. De Teresa, L. Bischoff, J. Michler, O. De Castro, A. Delobbe, P. Dunne, O. V. Dobrovolskiy, N. Frese, A. Gölzhäuser, P. Mazarov, D. Koelle, W. Möller, F. Pérez-Murano, P. Philipp, F. Vollnhals and G. Hlawacek, *Appl. Phys. Rev.*, 2023, **10**, 041311.
290 R. Winkler, B. B. Lewis, J. D. Fowlkes, P. D. Rack and H. Plank, *ACS Appl. Nano Mater.*, 2018, **1**, 1014–1027.
291 P. Niiranen, H. Nadhom, M. Zanáška, R. Boyd, M. Sortica, D. Primetzhofer, D. Lundin and H. Pedersen, *Rev. Sci. Instrum.*, 2023, **94**, 023902.
292 P. Niiranen, A. Kapran, H. Nadhom, M. Čada, Z. Hubička, H. Pedersen and D. Lundin, *J. Vac. Sci. Technol., A*, 2024, **42**, 023006.
293 H. Nadhom, Y. Yuan, P. Rouf, N. Solin and H. Pedersen, *J. Vac. Sci. Technol., A*, 2021, **39**, 043411.
294 G. Pozina, C.-W. Hsu, N. Abrikossova and C. Hemmingsson, *Crystals*, 2023, **13**, 373.
295 M. Xu, T. Bearda, M. Hasan, H. S. Radhakrishnan, I. Gordon, J. Szlufcik and J. Poortmans, in *2018 IEEE 7th*

World Conference on Photovoltaic Energy Conversion (WCPEC) (A Joint Conference of 45th IEEE PVSC, 28th PVSEC & 34th EU PVSEC), 2018, pp. 3148–3151.

296 H. Nadhom, R. Boyd, P. Rouf, D. Lundin and H. Pedersen, *J. Phys. Chem. Lett.*, 2021, **12**, 4130–4133.

297 G. Akiki, M. Frégnaux, I. Florea, P. Bulkin, D. Daineka, S. Filonovich, M. Bouttemy and E. V. Johnson, *J. Vac. Sci. Technol., A*, 2020, **39**, 013201.

298 I. V. Otto IV, C. Vallée, S. Kal and P. Biolsi, *J. Vac. Sci. Technol. B*, 2023, **41**, 032202.

299 D. N. Polyakov, V. V. Shumova and L. M. Vasilyak, *Plasma Sources Sci. Technol.*, 2021, **30**, 07LT01.

300 T. Faraz, K. Arts, S. Karwal, H. C. M. Knoops and W. M. M. Kessels, *Plasma Sources Sci. Technol.*, 2019, **28**, 024002.

301 S. J. C. Irvine and D. Lamb, in *Chemical Vapour Deposition: Precursors, Processes and Applications*, 2008, pp. 477–493.

302 C. P. Grigoropoulos, *Int. J. Extreme Manuf.*, 2019, **1**, 012002.

303 J. Niu, S. Meng, J. Li, H. Jin, F. Yi and Y. Qin, *Ceram. Int.*, 2020, **46**, 2086–2092.

304 S. Miyata, K. Matsuse, A. Ibi, T. Izumi, Y. Shiohara and T. Goto, *Supercond. Sci. Technol.*, 2013, **26**, 045020.

305 W. Arpavate, K. Roongraung and S. Chuangchote, in *Green Sustainable Process for Chemical and Environmental Engineering and Science*, ed. Inamuddin, R. Boddula, A. M. Asiri and M. M. Rahman, Elsevier, 2021, pp. 189–203.

306 D. J. Hwang, S.-G. Ryu and C. P. Grigoropoulos, *Nanotechnology*, 2011, **22**, 385303.

307 Y. van de Burgt, *J. Laser Appl.*, 2014, **26**, 032001.

308 R. Tu, Z. Liu, Q. Xu, S. Zhang, Q. Li, X. Zhang, M. L. Kosinova and T. Goto, *J. Eur. Ceram. Soc.*, 2023, **43**, 5214–5222.

309 K.-H. Dahmen, in *Encyclopedia of Physical Science and Technology* ed. R. A. Meyers, Academic Press, New York, 3rd edn, 2003, pp. 787–808.

310 M. R. Baklanov, V. Jousseaume, T. V. Rakhimova, D. V. Lopaev, Yu. A. Mankelevich, V. V. Afanas'ev, J. L. Shohet, S. W. King and E. T. Ryan, *Appl. Phys. Rev.*, 2019, **6**, 011301.

311 Y. Zhang, Z. Chen, K. Zhang, Z. Feng and H. Zhao, *Phys. Status Solidi RRL*, 2021, **15**, 2100202.

312 S. J. C. Irvine, in *Chemical Physics of Thin Film Deposition Processes for Micro- and Nano-Technologies*, ed. Y. Pauleau, Springer Netherlands, Dordrecht, 2002, pp. 199–222.

313 H. Cheng, R. Tu, S. Zhang, M. Han, T. Goto and L. Zhang, *J. Eur. Ceram. Soc.*, 2017, **37**, 509–515.

314 Y. Fujita, *J. Cryst. Growth*, 2000, **221**, 382–387.

315 D. Farhanian, G. De Crescenzo and J. R. Tavares, *Langmuir*, 2017, **33**, 1780–1791.

316 C. P. Christensen and K. M. Lakin, *Appl. Phys. Lett.*, 2008, **32**, 254–256.

317 G. Leyendecker, D. Bäuerle, P. Geittner and H. Lydtin, *Appl. Phys. Lett.*, 1981, **39**, 921–923.

318 B. Liu, R. F. Hicks and J. J. Zinck, *J. Cryst. Growth*, 1993, **129**, 111–118.

319 B. Liu, R. F. Hicks and J. J. Zinck, *J. Cryst. Growth*, 1992, **123**, 500–518.

320 A. Ruzin and Y. Nemirovsky, *J. Electron. Mater.*, 1993, **22**, 281–288.

321 S. J. C. Irvine, A. Stafford, M. U. Ahmed, A. Brown and H. Kheyrandish, *J. Electron. Mater.*, 1997, **26**, 723–727.

322 M. J. Santos, A. J. Silvestre and O. Conde, *Surf. Coat. Technol.*, 2002, **151–152**, 160–164.

323 J. Mazumder and A. Kar, *Theory and Application of Laser Chemical Vapor Deposition*, Springer US, Boston, MA, 1995.

324 C. Duty, D. Jean and W. J. Lackey, *Int. Mater. Rev.*, 2001, **46**, 271–287.

325 H. Sankur, *Thin Solid Films*, 1992, **218**, 161–169.

326 E. Hwang, J. Choi and S. Hong, *Nanoscale*, 2022, **14**, 16065–16076.

327 M. Yang, S. Bai, Q. Xu, J. Li, T. Shimada, Q. Li, T. Goto, R. Tu and S. Zhang, *Diamond Relat. Mater.*, 2020, **109**, 108094.

328 L. Constantin, L. Fan, C. Azina, K. Keramatnejad, J.-F. Silvain and Y. F. Lu, *Cryst. Growth Des.*, 2018, **18**, 2458–2466.

329 Z. Wu, W. Sun, A. Mao, Q. Zhu, X. Chen, X. Zhang, L. Trinh, N. Li, X. Huang, N. Kraiem, J.-F. Silvain, B. Cui and Y. Lu, *Diamond Relat. Mater.*, 2024, **142**, 110744.

330 L. S. Fan, Y. S. Zhou, M. X. Wang, Y. Gao, L. Liu, J. F. Silvain and Y. F. Lu, *Laser Phys. Lett.*, 2014, **11**, 076002.

331 A. Odusanya, I. Rahaman, P. K. Sarkar, A. Zkria, K. Ghosh and A. Haque, *C*, 2022, **8**, 24.

332 S. Yu, R. Tu and T. Goto, *J. Eur. Ceram. Soc.*, 2016, **36**, 403–409.

333 Z. Liu, Q. Xu, Q. Sun, J. Li, R. Tu, S. Zhang, M. Yang, Q. Li, Z. Deng, L. Zhang, T. Goto, H. Ohmori and M. Kosinova, *Thin Solid Films*, 2019, **678**, 8–15.

334 H. Katsui, K. Shimoda and M. Hotta, *Ceram. Int.*, 2023, **49**, 38813–38823.

335 K. An, H.-N. Lee, K.-H. Cho, Y. J. Han and K.-T. Kang, *Org. Electron.*, 2021, **91**, 106078.

336 H. Katsui, K. Harada, Z. Liu, N. Kondo and M. Hotta, *Ceram. Int.*, 2022, **48**, 31016–31022.

337 B. G. Salazar, C. R. Brewer, L. McElwee-White and A. V. Walker, *J. Vac. Sci. Technol., A*, 2022, **40**, 023404.

338 B. Sharma and A. Sharma, *Appl. Surf. Sci.*, 2021, **567**, 150724.

339 Y. D. Zhao, X. Dong, Z. Z. Ma, Y. T. Zhang, B. Wu, S. W. Zhuang, B. L. Zhang, W. C. Li and G. T. Du, *J. Cryst. Growth*, 2016, **454**, 30–34.

340 T. Wang, R. Tu, C. Zhang, S. Zhang, K. Wang, T. Goto and L. Zhang, *J. Asian Ceram. Soc.*, 2021, **9**, 197–207.

341 Y. Hashimoto and A. Ito, *Mater. Lett.*, 2024, **366**, 136558.

342 R. Tu, Z. Liu, C. Wang, P. Lu, B. Guo, Q. Xu, B.-W. Li and S. Zhang, *RSC Adv.*, 2022, **12**, 15555–15563.

343 T.-H. Feng and X.-C. Xia, *Opt. Mater. Express*, 2017, **7**, 1281–1288.

344 Y. Mitsuhashi, S. Matsumoto and A. Ito, *Mater. Trans.*, 2023, **64**, 1107–1111.

345 Y. Mitsuhashi, S. Matsumoto and A. Ito, *J. Am. Ceram. Soc.*, 2023, **106**, 5140–5146.

346 N. Yamaguchi and A. Ito, *Mater. Lett.*, 2024, **369**, 136721.

347 W. Li, Y. Zhang, Z. Chen, H. Zhao, S. A. Ringel and A. R. Arehart, *Appl. Phys. Lett.*, 2023, **123**, 112101.

348 E. Güney, J. Karimzadeh Khoei, B. S. Sengul, F. Can and G. Ozaydin Ince, *J. Appl. Polym. Sci.*, 2024, **141**, e55210.

349 A. Aufoujal, U. Legrand, J.-L. Meunier and J. R. Tavares, *Catalysts*, 2020, **10**, 534.

350 D. Kim, A. Park, Y. Choi, H. Seong, S. J. Shin, Y. H. Cho and Y. Yoo, *ACS Appl. Polym. Mater.*, 2023, **5**, 8474–8482.

351 K. R. Johnson, P. Arevalo Rodriguez, C. R. Brewer, J. A. Brannaka, Z. Shi, J. Yang, B. Salazar, L. McElwee-White and A. V. Walker, *J. Chem. Phys.*, 2016, **146**, 052816.

352 T. Tsuchiya, *J. Ceram. Soc. Jpn.*, 2018, **126**, 889–899.

353 K. K. Gleason, *Adv. Mater.*, 2024, **36**, 2306665.

354 H. Akazawa, *J. Vac. Sci. Technol., A*, 2018, **36**, 041505.

355 H. Akazawa, *J. Vac. Sci. Technol. B*, 2022, **40**, 062204.

356 H. Nasri Lari, J. Chaouki and J. R. Tavares, *Chem. Eng. J.*, 2020, **390**, 124526.

357 E. Kasparek, J. R. Tavares, M. R. Wertheimer and P.-L. Girard-Lauriault, *Langmuir*, 2018, **34**, 12234–12243.

358 H. Wang, Y. Zhao, J. Li, Y. Zhou, Z. Shi, C. Yin, S. Zhuang and F. Yang, *Mater. Res. Express*, 2019, **6**, 095914.

359 C.-S. Xu and P.-W. Lv, *Chin. J. Struct. Chem.*, 2021, **40**, 1223–1230.

360 H. Liu, C. R. Brewer, A. V. Walker and L. McElwee-White, *Organometallics*, 2020, **39**, 4565–4574.

361 C. R. Brewer, N. C. Sheehan, J. Herrera, A. V. Walker and L. McElwee-White, *Organometallics*, 2022, **41**, 761–775.

362 C. R. Brewer, O. M. Hawkins, N. C. Sheehan, J. D. Bullock, V. D. Kleiman, A. V. Walker and L. McElwee-White, *Organometallics*, 2019, **38**, 4363–4370.

363 S. P. Murzin, *Appl. Sci.*, 2022, **12**, 12133.

364 K. Jeong, J. Lee, I. Byun, M. Seong, J. Park, H. Nam and J. Lee, *Thin Solid Films*, 2017, **626**, 145–153.

365 L.-S. Fan, L. Constantin, D. Li, L. Liu, K. Keramatnejad, C. Azina, X. Huang, H. R. Golgir, Y. Lu, Z. Ahmadi, F. Wang, J. Shield, B. Cui, J.-F. Silvain and Y.-F. Lu, *Light:Sci. Appl.*, 2018, **7**, 17177.

366 S. Kuk, H. K. Nam, Z. Wang and D. J. Hwang, *J. Nanosci. Nanotechnol.*, 2018, **18**, 7085–7089.

367 Q. Xu, P. Zhu, Q. Sun, R. Tu, S. Zhang, M. Yang, Q. Li, J. Shi, H. Li, L. Zhang, T. Goto, M. Han, J. Yan, S. Li and H. Ohmori, *J. Am. Ceram. Soc.*, 2018, **101**, 1471–1478.

368 H. R. Golgir, Y. S. Zhou, D. Li, K. Keramatnejad, W. Xiong, M. Wang, L. J. Jiang, X. Huang, L. Jiang, J. F. Silvain and Y. F. Lu, *J. Appl. Phys.*, 2016, **120**, 105303.

369 L. Fan, L. Constantin, Z. P. Wu, K. A. McElveen, X. G. Chen, T. He, F. Wang, C. Debiemme-Chouvy, B. Cui, R. Y. Lai, X. Li, J. F. Silvain and Y. F. Lu, *Sci. Adv.*, 2021, **7**, eabc7547.

370 Y. S. Zhou, L. S. Fan, Z. Q. Xie, L. Jiang, J.-F. Silvain and Y. F. Lu, *Curr. Opin. Solid State Mater. Sci.*, 2015, **19**, 107–114.

371 J. Lasseter, P. D. Rack and S. J. Randolph, *Nanomaterials*, 2023, **13**, 757.

372 W. Zhang, X.-y. Chen, Y.-s. Ma, W.-x. Fu, L. Wang, H. Zhou, Z.-j. Xu, B. Wang and Y.-s. Ruan, *Chin. J. Liq. Cryst. Disp.*, 2019, **34**, 755–763.

373 K. Jeong, J. Lee, I. Byun, M. Seong, J. Park, H. W. Kim, M. J. Kim, J.-H. Kim and J. Lee, *Mater. Sci. Semicond. Process.*, 2017, **68**, 245–251.

374 K. An, H.-N. Lee, K. H. Cho, S.-W. Lee, D. J. Hwang and K.-T. Kang, *Micromachines*, 2020, **11**, 88.

375 N. Khosla, J. Narayan and R. Narayan, *J. Mater. Res.*, 2024, **39**, 716–725.

376 S. J. Panchu, S. Dhani, A. Chuturgoon and M. K. Moodley, *J. Photochem. Photobiol., B*, 2018, **187**, 10–17.

377 S. J. Panchu, M. A. Adebisi, E. Manikandan and M. K. Moodley, *J. Electron. Mater.*, 2020, **49**, 1957–1968.

378 S. J. Panchu, K. Raju, H. C. Swart, B. Chokkalingam, M. Maaza, M. Henini and M. K. Moodley, *ACS Omega*, 2021, **6**, 4542–4550.

379 J. W. Um, S.-Y. Kim, B. H. Lee, J. B. Park and S. Jeong, *Carbon*, 2020, **169**, 163–171.

380 Z. Liu, Y. Cai, R. Tu, Q. Xu, M. Hu, C. Wang, Q. Sun, B.-W. Li, S. Zhang, C. Wang, T. Goto and L. Zhang, *Carbon*, 2021, **175**, 377–386.

381 J. Lasseter, P. D. Rack and S. J. Randolph, *ACS Appl. Nano Mater.*, 2022, **5**, 10890–10899.

382 F. Lisha, L. Fan, W. Guolong, V. S. Kovalenko and Y. Jianhua, *Opto-Electron. Eng.*, 2022, **49**, 210333.

383 C. Zhang, J. Zhang, K. Lin and Y. Huang, *Rev. Sci. Instrum.*, 2017, **88**, 053907.

384 B. Fotovvati, A. Dehghanghadikolaei and N. Namdari, *Part. Sci. Technol.*, 2021, **39**, 738–747.

385 T. Goto, *J. Wuhan Univ. Technol., Mater. Sci. Ed.*, 2016, **31**, 1–5.

386 Y. Zhang, Y. Jiao, C. Li, C. Chen, J. Li, Y. Hu, D. Wu and J. Chu, *Int. J. Extrem. Manuf.*, 2020, **2**, 032002.

387 A. Ito, *J. Ceram. Soc. Jpn.*, 2021, **129**, 646–653.

388 S. Bai, L. Ruan, H. Chen, Y. Du, H. Deng, N. Dai and Y. Tang, *Chem. Eng. J.*, 2024, **493**, 152805.

389 Z. Wu, A. Mao, L. Wadle, X. Huang, N. Kraiem, J.-F. Silvain, B. Cui and Y. Lu, *Diamond Relat. Mater.*, 2024, **149**, 111549.

390 Z. Q. Xie, J. Bai, Y. S. Zhou, Y. Gao, J. Park, T. Guillemet, L. Jiang, X. C. Zeng and Y. F. Lu, *Sci. Rep.*, 2014, **4**, 4581.

391 Q. Xu, Z. Deng, Q. Sun, R. Tu, S. Zhang, M. Yang, Q. Li, L. Zhang, T. Goto and H. Ohmori, *Carbon*, 2018, **139**, 76–84.

392 Q. Sun, R. Tu, Q. Xu, C. Zhang, J. Li, H. Ohmori, M. Kosinova, B. Basu, J. Yan, S. Li, T. Goto, L. Zhang and S. Zhang, *J. Power Sources*, 2019, **444**, 227308.

393 R. Tu, Z. Hu, Q. Xu, L. Li, M. Yang, Q. Li, J. Shi, H. Li, S. Zhang, L. Zhang, T. Goto, H. Ohmori, M. Kosinova and B. Basu, *J. Asian Ceram. Soc.*, 2019, **7**, 312–320.

394 J. S. Ten, M. Sparkes and W. O'Neill, in *Laser Applications in Microelectronic and Optoelectronic Manufacturing (LAMOM) XXII, SPIE*, 2017, vol. 10091, pp. 52–58.

395 M. Trippel, J. Bläsing, M. Wieneke, A. Dadgar, G. Schmidt, F. Bertram, J. Christen and A. Strittmatter, *Rev. Sci. Instrum.*, 2022, **93**, 113904.

396 H. Rabiee Golgir, D. W. Li, K. Keramatnejad, Q. M. Zou, J. Xiao, F. Wang, L. Jiang, J.-F. Silvain and Y. F. Lu, *ACS Appl. Mater. Interfaces*, 2017, **9**, 21539–21547.

397 Y. Zhang, V. G. Thirupakuzi Vangipuram, K. Zhang and H. Zhao, *Appl. Phys. Lett.*, 2023, **122**, 162101.

398 C. S. Torres-Castillo and J. R. Tavares, *Can. J. Chem. Eng.*, 2023, **101**, 1410–1420.

399 A. Khlyustova, Y. Cheng and R. Yang, *J. Mater. Chem. B*, 2020, **8**, 6588–6609.

400 R. Fan and T. L. Andrew, *J. Electrochem. Soc.*, 2021, **168**, 077518.

401 C. A. Dorval Dion and J. R. Tavares, *Powder Technol.*, 2013, **239**, 484–491.

402 S. Hosseininasab, N. Faucheux, G. Soucy and J. R. Tavares, *J. Nanopart. Res.*, 2019, **21**, 114.

403 S. Yousefi, M. A. Makarem, E. Rahimpour and M. R. Rahimpour, in *Advances in Synthesis Gas : Methods, Technologies and Applications*, ed. M. R. Rahimpour, M. A. Makarem and M. Meshksar, Elsevier, 2023, vol. 3, pp. 395–410.

404 H. Nasri Lari, D. Farhanian, D. C. Boffito, G. S. Patience, G. De Crescenzo, J. Chaouki and J. R. Tavares, *Catal. Commun.*, 2017, **100**, 19–23.

405 V. Labonté, A. Marion, N. Virgilio and J. R. Tavares, *Ind. Eng. Chem. Res.*, 2016, **55**, 7362–7372.

406 D. Farhanian, G. De Crescenzo and J. R. Tavares, *Sci. Rep.*, 2018, **8**, 12223.

407 S. Hosseininasab, N. Faucheux, G. Soucy and J. R. Tavares, *Chem. Eng. J.*, 2017, **325**, 101–113.

408 A. Bérard, G. S. Patience, G. Chouinard and J. R. Tavares, *Sci. Rep.*, 2016, **6**, 31574.

409 P. R. Riley, P. Joshi, N. Khosla, R. J. Narayan and J. Narayan, *Carbon*, 2022, **196**, 972–978.

410 M. J. Jeon, S.-K. Hyeong, H. Y. Jang, J. Mun, T.-W. Kim, S. Bae and S.-K. Lee, *Nanomaterials*, 2023, **13**, 2937.

411 D. A. Boyd, L. Greengard, M. Brongersma, M. Y. El-Naggar and D. G. Goodwin, *Nano Lett.*, 2006, **6**, 2592–2597.

412 J. Svensson, N. M. Bulgakova, O. A. Nerushev and E. E. B. Campbell, *Phys. Rev. B:Condens. Matter Mater. Phys.*, 2006, **73**, 205413.

413 D. Dey and A. K. Tiwari, *ACS Omega*, 2020, **5**, 17857–17867.

414 I. Angelov, L. Zaharieva and L. Antonov, *Molecules*, 2023, **28**, 695.

415 N. Wang and L. Weatherley, *Curr. Opin. Chem. Eng.*, 2023, **39**, 100895.

416 S. Xu, R. Eisenberg, Z. Song and H. Huang, *Phys. Rev. E*, 2023, **108**, 064413.

417 F. Che, J. T. Gray, S. Ha, N. Kruse, S. L. Scott and J.-S. McEwen, *ACS Catal.*, 2018, **8**, 5153–5174.

418 I. Lyubinetsky, S. Mezhenny, W. J. Choyke and J. T. Yates Jr, *J. Vac. Sci. Technol., A*, 1999, **17**, 1445–1450.

419 S. Yugo, T. Kanai, T. Kimura and T. Muto, *Appl. Phys. Lett.*, 1991, **58**, 1036–1038.

420 V. S. Jayaseelan and R. N. Singh, *J. Appl. Phys.*, 2023, **133**, 155302.

421 A. Saravanan, B.-R. Huang, K. J. Sankaran, S. Kunuku, C.-L. Dong, K.-C. Leou, N.-H. Tai and I.-N. Lin, *ACS Appl. Mater. Interfaces*, 2014, **6**, 10566–10575.

422 Y. Zhang, A. Chang, J. Cao, Q. Wang, W. Kim, Y. Li, N. Morris, E. Yenilmez, J. Kong and H. Dai, *Appl. Phys. Lett.*, 2001, **79**, 3155–3157.

423 *Appendix B - Bias Enhanced Nucleation*, **https://www.chm.bris.ac.uk/pt/diamond/stuthesis/appendb.htm#_ednref15**, accessed February 12, 2024.

424 N. M. Hwang, *Non-Classical Crystallization of Thin Films and Nanostructures in CVD and PVD Processes*, Springer Netherlands, Dordrecht, 2016, vol. 60.

425 J. J. Alcantar-Peña, E. de Obaldia, J. Montes-Gutierrez, K. Kang, M. J. Arellano-Jimenez, J. E. Ortega Aguilar, G. P. Suchy, D. Berman-Mendoza, R. Garcia, M. J. Yacaman and O. Auciello, *Diamond Relat. Mater.*, 2017, **78**, 1–11.

426 L. Osman, A. Zkria, A. M. Ali, S. Nagano, H. Naragino and T. Yoshitake, *Appl. Phys. Express*, 2023, **16**, 075501.

427 W. Wang, S. Yang, B. Liu, X. Hao, J. Han, B. Dai and J. Zhu, *Carbon Lett.*, 2023, **33**, 517–530.

428 A. Saravanan, B. R. Huang, K. J. Sankaran, G. Keiser, J. Kurian, N. H. Tai and I. N. Lin, *J. Appl. Phys.*, 2015, **117**, 215307.

429 W.-K. Youn, C.-S. Kim, J.-Y. Lee, S.-S. Lee and N.-M. Hwang, *J. Phys. Chem. C*, 2012, **116**, 25157–25163.

430 D.-S. Kim and N.-M. Hwang, *J. Phys. D: Appl. Phys.*, 2018, **51**, 463002.

431 J. Wang, J.-H. Park, A.-Y. Lu and J. Kong, *J. Am. Chem. Soc.*, 2022, **144**, 22925–22932.

432 M.-S. Chae, T. H. Lee, K. R. Son, Y. W. Kim, K. S. Hwang and T. G. Kim, *Nanoscale Horiz.*, 2019, **4**, 610–618.

433 Q.-J. Feng, H.-W. Liang, Y.-Y. Mei, J.-Y. Liu, C. C. Ling, P.-C. Tao, D.-Z. Pan and Y.-Q. Yang, *J. Mater. Chem. C*, 2015, **3**, 4678–4682.

434 H. Bae, K. Sasai, H. Suzuki and H. Toyoda, *Vacuum*, 2021, **192**, 110429.

435 J. Langer, V. Cimalla, V. Lebedev, L. Kirste, M. Prescher, T. Luo, J. Jeske and O. Ambacher, *Phys. Status Solidi A*, 2022, **219**, 2100756.

436 K. An, S. Zhang, S. Shao, J. Liu, J. Wei, L. Chen, Y. Zheng, Q. Liu and C. Li, *Plasma Sci. Technol.*, 2022, **24**, 045502.

437 V. Beladiya, M. Becker, T. Faraz, W. M. M. Erwin Kessels, P. Schenk, F. Otto, T. Fritz, M. Gruenewald, C. Helbing, K. D. Jandt, A. Tünnermann, M. Sierka and A. Szeghalmi, *Nanoscale*, 2020, **12**, 2089–2102.

438 B. Wang, D. Yang, X. Zhu, Y. Zhao, S. Wang, J. Zhu and M. Zhai, *Processes*, 2022, **10**, 2665.

439 T. Yoshimura, S. Tatsuura and W. Sotoyama, *Thin Solid Films*, 1992, **207**, 9–11.

440 S. Tatsuura, W. Sotoyama and T. Yoshimura, *Appl. Phys. Lett.*, 1992, **60**, 1661–1663.

441 S. Tatsuura, W. Sotoyama, K. Motoyoshi, A. Matsuura, T. Hayano and T. Yoshimura, *Appl. Phys. Lett.*, 1993, **62**, 2182–2184.

442 N. Hu, Y. Wang, J. Li, Q. Wei, Y. Jiang, L. Ma, Z. Yu, K. Zhou and H. Long, *Surf. Coat. Technol.*, 2019, **359**, 459–467.

443 B. Peng, S. Jiang, Y. Zhang and J. Zhang, *Carbon*, 2011, **49**, 2555–2560.

444 N. Panjawi, A. Naik, M. E. A. Warwick, G. Hyett and R. Binions, *Chem. Vap. Deposition*, 2012, **18**, 102–106.

445 A. J. T. Naik, M. E. A. Warwick, S. J. A. Moniz, C. S. Blackman, I. P. Parkin and R. Binions, *J. Mater. Chem. A*, 2013, **1**, 1827–1833.

446 M. E. A. Warwick, I. Ridley and R. Binions, *Surf. Coat. Technol.*, 2013, **230**, 163–167.

447 L. Romero and R. Binions, *Surf. Coat. Technol.*, 2013, **230**, 196–201.

448 A. J. T. Naik, C. Bowman, N. Panjwani, M. E. A. Warwick and R. Binions, *Thin Solid Films*, 2013, **544**, 452–456.
449 L. Romero, A. B. Jorge, P. F. McMillan and R. Binions, *ECS J. Solid State Sci. Technol.*, 2014, **3**, N107.
450 F. Qiu-Ju, L. Fang, L. Tong-Tong, L. Yun-Zheng, S. Bo, L. Meng-Ke and L. Hong-Wei, *Acta Phys. Sin.*, 2018, **67**, 218101.
451 I. Top, R. Binions, M. E. A. Warwick, C. W. Dunnill, M. Holdynski and I. Abrahams, *J. Mater. Chem. C*, 2018, **6**, 4485–4493.
452 M. E. A. Warwick, I. Ridley and R. Binions, *Sol. Energy Mater. Sol. Cells*, 2016, **157**, 686–694.
453 L. Romero, A.-B. Jorge-Sobrido, P. F. McMillan and R. Binions, *Thin Solid Films*, 2015, **584**, 320–325.
454 L. Romero, C. Piccirillo, P. M. L. Castro, C. Bowman, M. E. A. Warwick and R. Binions, *Chem. Vap. Deposition*, 2015, **21**, 63–70.
455 W.-J. Lee, S.-K. Rha, S.-Y. Lee and C.-O. Park, *J. Electrochem. Soc.*, 1997, **144**, 683.
456 E. Pawlas-Foryst, W. Przybyło, M. Kopyto and K. Fitzner, *Mater. Res. Bull.*, 2001, **36**, 915–923.
457 Y.-T. Jang, J.-H. Ahn, B.-K. Ju and Y.-H. Lee, *Solid State Commun.*, 2003, **126**, 305–308.
458 G. Shaw, I. P. Parkin, K. F. E. Pratt and D. E. Williams, *J. Mater. Chem.*, 2005, **15**, 149–154.
459 M. E. A. Warwick, I. Ridley and R. Binions, *J. Nanosci. Nanotechnol.*, 2011, **11**, 8158–8162.
460 J. Crane, M. Warwick, R. Smith, N. Furlan and R. Binions, *J. Electrochem. Soc.*, 2010, **158**, D62.
461 R. Naeem, S. Ahmed, K. M. Lo, W. J. Basirun, R. Yahya, M. Misran, T. A. N. Peiris, J. S. Sagu, K. G. U. Wijayantha, A. K. Thapa, G. U. Sumanasekera and M. Mazhar, *Chem. Vap. Deposition*, 2015, **21**, 360–368.
462 J.-Y. Lee and J.-H. Yoon, *Solid State Commun.*, 2004, **132**, 627–630.
463 R. Naeem, R. Yahya, A. Pandikumar, H. N. Ming and M. Mazhar, *J. Mater. Sci.: Mater. Electron.*, 2017, **28**, 868–877.
464 L. Issman, P. A. Kloza, J. Terrones Portas, B. Collins, A. Pendashteh, M. Pick, J. J. Vilatela, J. A. Elliott and A. Boies, *ACS Nano*, 2022, **16**, 9583–9597.
465 S. Zhao, Q. Feng, C. Gao, D. Wang, Y. Xing, J. Xie, Z. Dong, M. Li and H. Liang, *Mater. Sci. Semicond. Process.*, 2020, **116**, 105142.
466 S.-H. Park, J.-W. Park, S.-M. Yang, K.-H. Kim and N.-M. Hwang, *J. Phys. Chem. C*, 2015, **119**, 25047–25052.
467 S. Park, J. Jung, K. Kim, K. Kim and N. Hwang, *Cryst. Growth Des.*, 2018, **18**, 5816–5823.
468 D. Kim, D.-Y. Kim, J.-H. Kwon and N.-M. Hwang, *Coatings*, 2020, **10**, 726.
469 A. Gamboa, L. M. Marques and E. C. Fernandes, *Diamond Relat. Mater.*, 2021, **113**, 108274.
470 C. Luo, G. Liu and M. Zhang, *Front. Mater. Sci.*, 2019, **13**, 270–276.
471 C. Liao, Y. Zhang and C. Pan, *J. Appl. Phys.*, 2012, **112**, 114310.
472 H. Tani, R. Lu, S. Koganezawa and N. Tagawa, *IEEE Trans. Magn.*, 2017, **53**, 1–6.
473 N. M. Hwang, in *Non-Classical Crystallization of Thin Films and Nanostructures in CVD and PVD Processes*, ed. N. M. Hwang, Springer Netherlands, Dordrecht, 2016, pp. 261–289.
474 J.-W. Park, K.-H. Kim and N.-M. Hwang, *Adv. Mater. Lett.*, 2018, **9**, 638–642.
475 S.-W. Yoo, N.-M. Hwang, S.-J. You, J.-H. Kim and D.-J. Seong, *J. Nanopart. Res.*, 2017, **19**, 374.
476 T. Sharda, M. Umeno, T. Soga and T. Jimbo, *Appl. Phys. Lett.*, 2000, **77**, 4304–4306.
477 W. Chen, C. Xiao, Q. Yang, A. Moewes and A. Hirose, *Can. J. Phys.*, 2005, **83**, 753–759.
478 J.-I. Lee and N.-M. Hwang, *Carbon*, 2008, **46**, 1588–1592.
479 E. Plaza, H. Briceño-Fuenmayor, J. Arévalo, R. Atencio and L. Corredor, *J. Nanopart. Res.*, 2015, **17**, 246.
480 H. Kanayama, K. Ikesugi, K. Shimanaka and H. Sato, *Diamond Relat. Mater.*, 2012, **24**, 83–87.
481 J. Zhang and C. Pan, *J. Alloys Compd.*, 2010, **495**, 93–96.
482 S. A. Linnik, A. V. Gaydaychuk, A. S. Mitulinsky and S. P. Zenkin, *Mater. Lett.*, 2022, **324**, 132670.
483 K. Ishikawa, *Adv. Eng. Mater.*, 2024, **26**, 2400679.
484 A. Roy and D. Das, *Diamond Relat. Mater.*, 2018, **88**, 204–214.
485 D. Das and A. Roy, *Appl. Surf. Sci.*, 2020, **515**, 146043.
486 M. G. Cuxart, I. Šics, A. R. Goñi, E. Pach, G. Sauthier, M. Paradinas, M. Foerster, L. Aballe, H. M. Fernandez, V. Carlino and E. Pellegrin, *Carbon*, 2017, **117**, 331–342.
487 Y. Qi, B. Deng, X. Guo, S. Chen, J. Gao, T. Li, Z. Dou, H. Ci, J. Sun, Z. Chen, R. Wang, L. Cui, X. Chen, K. Chen, H. Wang, S. Wang, P. Gao, M. H. Rummeli, H. Peng, Y. Zhang and Z. Liu, *Adv. Mater.*, 2018, **30**, 1704839.
488 K. S. A. Butcher, V. Georgiev, D. Georgieva, R. Gergova, P. Terziyska and P. W. Binsted, *Coatings*, 2022, **12**, 1581.
489 T. Yoshikawa, D. Herrling, F. Meyer, F. Burmeister, C. E. Nebel, O. Ambacher and V. Lebedev, *J. Vac. Sci. Technol. B*, 2019, **37**, 021207.
490 J. Reiprich, N. A. Isaac, L. Schlag, T. Kups, M. Hopfeld, G. Ecke, T. Stauden, J. Pezoldt and H. O. Jacobs, *ACS Nano*, 2020, **14**, 12885–12894.
491 L. Shi, F. Xu, J. Gao, M. Yuen, S. Sun, J. Xu, K. Jia and D. Zuo, *Diamond Relat. Mater.*, 2020, **109**, 108098.
492 J. Geiser and M. Arab, *Spec. Top. Rev. Porous Media*, 2010, **1**, 215–229.
493 L. Rudniak, *Comput. Chem. Eng.*, 1998, **22**, S755–S758.
494 D. Li-Fang, C. Jun-Ying, D. Guo-Yi and S. Yong, *Chinese Phys.*, 2002, **11**, 419.
495 D. Lifang, M. Boqin, S. Yong and W. Zhijun, *Plasma Sci. Technol.*, 2005, **7**, 2845.
496 M. Saeidi, M. Vaezzadeh and F. Badakhshan, *Phys. B*, 2011, **406**, 1038–1040.
497 M. Saeidi, *Phys. E*, 2015, **70**, 225–230.
498 M. Yan, T. Zhang, B. Wang, J. Liu, X. Liang, Y. Xu and F. Yi, *J. Appl. Phys.*, 2023, **134**, 155303.
499 V. Beladiya, T. Faraz, P. Schmitt, A.-S. Munser, S. Schröder, S. Riese, C. Mühlig, D. Schachtler, F. Steger, R. Botha,

F. Otto, T. Fritz, C. van Helvoirt, W. M. M. Kessels, H. Gargouri and A. Szeghalmi, *ACS Appl. Mater. Interfaces*, 2022, **14**, 14677–14692.

500 B. Reeja-Jayan and J. Luo, *MRS Bull.*, 2021, **46**, 26–35.

501 J. W. Strand, J. Cottom, L. Larcher and A. L. Shluger, *Phys. Rev. B*, 2020, **102**, 014106.

502 A. Ansh, U. Patbhaje, J. Kumar, A. Meersha and M. Shrivastava, *Commun. Mater.*, 2023, **4**, 1–11.

503 W.-K. Youn, S.-S. Lee, J.-Y. Lee, C.-S. Kim, N.-M. Hwang and S. Iijima, *J. Phys. Chem. C*, 2014, **118**, 11946–11953.

504 M. G. Byun, J. W. Yang, J. H. Park, N. M. Hwang, J. Park and B. D. Yu, *Cryst. Growth Des.*, 2022, **22**, 2490–2498.

505 M. G. Byun, J. H. Park, J. W. Yang, N. M. Hwang, J. Park and B. D. Yu, *Electron. Mater. Lett.*, 2023, **19**, 218–228.

506 *Magneto-Science: Magnetic Field Effects on Materials: Fundamentals and Applications*, ed. M. Yamaguchi and Y. Tanimoto, Springer, Berlin, Heidelberg, 2006, pp. 1–40.

507 U. E. Steiner and T. Ulrich, *Chem. Rev.*, 1989, **89**, 51–147.

508 A. A. J. Kipriyanov and P. A. Purtov, *Bull. Korean Chem. Soc.*, 2012, **33**, 1009–1014.

509 Y. Ma, K. Watanabe, S. Awaji and M. Motokawa, *J. Cryst. Growth*, 2001, **233**, 483–489.

510 Y. Lu, C. Yang, H. Wang, L. Ma, M. Xu and L. Xi, *Vacuum*, 2023, **211**, 111912.

511 Z. Wu, Y. Zhang, Y. Shen, W. Zhang and G. Shao, *Adv. Mater. Interfaces*, 2020, **7**, 2000854.

512 M. Baghgar, Y. Abdi and E. Arzi, *Commun. Mater.*, 2009, **48**, 20603.

513 H. Yasuda, *Magneto Luminous Chemical Vapor Deposition*, CRC Press, Boca Raton, 2012.

514 M. Taniguchi, M. Hirose, T. Hamasaki and Y. Osaka, *Appl. Phys. Lett.*, 2008, **37**, 787–788.

515 T. Hamasaki, H. Kurata, M. Hirose and Y. Osaka, *Appl. Phys. Lett.*, 2008, **37**, 1084–1086.

516 T. H. Yuzuriha, W. E. Mlynko and D. W. Hess, *J. Vac. Sci. Technol., A*, 1985, **3**, 2135–2140.

517 Z. Sun, X. Shi and E. Liu, *Thin Solid Films*, 1999, **355–356**, 146–150.

518 S. R. P. Silva, K. J. Clay, S. P. Speakman and G. A. J. Amaratunga, *Diamond Relat. Mater.*, 1995, **4**, 977–983.

519 J. Schwan, S. Ulrich, K. Jung, H. Ehrhardt, R. Samlenski and R. Brenn, *Diamond Relat. Mater.*, 1995, **4**, 304–308.

520 C. Luo, D. Wan, J. Jia, D. Li, C. Pan and L. Liao, *Nanoscale*, 2016, **8**, 13017–13024.

521 G.-L. Tian, J.-Q. Huang, J. Li, Q. Zhang and F. Wei, *Carbon*, 2016, **108**, 404–411.

522 C. B. Lugod and J. Auresenia, *MATEC Web Conf.*, 2019, **268**, 05004.

523 X. Liu, K. Wen, X. Duan, C. Wang and H. Long, *Vacuum*, 2023, **218**, 112661.

524 F. Kwok, X. Du, Z. Sun, M. Ng, Q. Liu, L. L. Fan, W. Yip, D. Kwok and S. To, *Surf. Coat. Technol.*, 2024, **483**, 130802.

525 Y. Wang, J. Li, H. Long, H. Luo, B. Zhou, Y. Xie, S. Li, Q. Wei and Z. Yu, *Surf. Coat. Technol.*, 2016, **292**, 49–53.

526 F. M. Kwok, X. Du, Z. Sun, M. C. Ng, W. S. Yip, K. Y. D. Kwok and S. To, *Surf. Coat. Technol.*, 2025, **495**, 131588.

527 D. Wei, Y. Liu, L. Cao, L. Fu, X. Li, Y. Wang and G. Yu, *J. Am. Chem. Soc.*, 2007, **129**, 7364–7368.

528 C. Luo, Q. Fu and C. Pan, *Sci. Rep.*, 2015, **5**, 9062.

529 A. Hamasaki, A. Furuse, J. Uchimura, Y. Takashima and S. Ozeki, *Int. J. Appl. Electromagn. Mech.*, 2023, **71**, S393–S401.

530 D. Stadler, D. N. Mueller, T. Brede, T. Duchoň, T. Fischer, A. Sarkar, M. Giesen, C. M. Schneider, C. A. Volkert and S. Mathur, *J. Phys. Chem. Lett.*, 2019, **10**, 6253–6259.

531 A. Raauf, J. Leduc, M. Frank, D. Stadler, D. Graf, M. Wilhelm, M. Grosch and S. Mathur, *Inorg. Chem.*, 2021, **60**, 1915–1921.

532 M. Pyeon, V. Rauch, D. Stadler, M. Gürsoy, M. Deo, Y. Gönüllü, T. Fischer, T. Hwang and S. Mathur, *Adv. Eng. Mater.*, 2019, **21**, 1900195.

533 D. Stadler, T. Brede, D. Schwarzbach, F. Maccari, T. Fischer, O. Gutfleisch, C. A. Volkert and S. Mathur, *Nanoscale Adv.*, 2019, **1**, 4290–4295.

534 P. Tutacz, D. Stadler, T. Karimpour, T. Duchoň, S. Cramm, C. M. Schneider, T. Fischer, D. N. Mueller and S. Mathur, *Chem. Mater.*, 2023, **35**, 8050–8056.

535 H. Lee, Z. T. Aytuna, A. Bhardwaj, M. Wilhelm, K. Lê, B. May, D. N. Mueller and S. Mathur, *Adv. Eng. Mater.*, 2023, **25**, 2300021.

536 M. Frank, L. Jürgensen, J. Leduc, D. Stadler, D. Graf, I. Gessner, F. Zajusch, T. Fischer, M.-A. Rose, D. N. Mueller and S. Mathur, *Inorg. Chem.*, 2019, **58**, 10408–10416.

537 R. B. Little and R. Goddard, *J. Appl. Phys.*, 2004, **95**, 2702–2712.

538 X. You, Z. Yu, L. Shi and L. Wang, *J. Cryst. Growth*, 2009, **311**, 4675–4678.

539 H. Long, S. Li, H. Luo, Y. Wang, Q. P. Wei and Z. M. Yu, *Appl. Surf. Sci.*, 2015, **353**, 548–552.

540 X. Liu, K. Wen, X. Duan, C. Wang and H. Long, *Coatings*, 2023, **13**, 441.

541 Y. J. Kim, Y. S. Choi, K. S. Shin, S. H. Cho, I. S. Choi and J. G. Han, *Curr. Appl. Phys.*, 2010, **10**, S354–S356.

542 D.-H. Kim, H.-S. Jang, H.-R. Lee, C.-D. Kim and H.-D. Kang, *Appl. Phys. Lett.*, 2004, **85**, 109–111.

543 A. Mettenbörger, T. Singh, A. P. Singh, T. T. Järvi, M. Moseler, M. Valldor and S. Mathur, *Int. J. Hydrogen Energy*, 2014, **39**, 4828–4835.

544 S. Awaji, K. Watanabe, Y. Ma and M. Motokawa, *Phys. B*, 2001, **294–295**, 482–485.

545 M. Tahashi, K. Sassa and S. Asai, *Mater. Trans.*, 2002, **43**, 2813–2817.

546 Y. Wu, H. Tao, S. Su, H. Yue, H. Li, Z. Zhang, Z. Ni and X. Chen, *Sci. Rep.*, 2017, **7**, 46583.

547 PMR, *Chemical Vapor Deposition Market Size, Growth Report*, 2032, **https://www.polarismarketresearch.com**; **https://www.polarismarketresearch.com/industry-analysis/chemical-vapor-deposition-cvd-market**, accessed December 3, 2024.